Analysis of EMI issues in DC-Microgrids due to Power Electronic Converters

Angaline Reshmi Krishna

A thesis submitted to the Auckland University of Technology, New Zealand in fulfilment of the requirements for the degree of ***Master of Engineering****.*

15th May 2022

Abstract

This research provides an overview of a MATLAB/Simulink model of the DC Microgrid system and presents key results from simulation studies undertaken to estimate the conducted electromagnetic interference arising from the interactions between power converters. This research has investigated how multi-converters in a DC Microgrid system, contribute to the generation of aggregated conducted electromagnetic interference. An islanded DC Microgrid model was built and simulated with and without the presence of the EMI suppressing filters. Spectrum analysis was performed on the DC-DC converters using several DC Microgrid topologies to analyse the EMI emissions in the DC Microgrids due to the interactions between its multiple power converters of different switching frequencies. The simulation results obtained, supported by the mathematical analysis, confirmed that in multi-converter systems, aggregated conducted electromagnetic interference is more prevalent in DC Microgrid topologies where the power converters have different switching frequencies relative to the DC Microgrid models where converters have similar switching frequencies. It was also found that custom-tuned PID-controlled DC-DC converters helped reduce the aggregated conducted electromagnetic interference in contrast to the un-tuned PI/PID controlled converters. It was also noted that the PID-controlled converters were more effective in minimizing the electromagnetic interference than the PI-controlled converters, due to their enhanced stability.

Overall, the research findings indicated that the DC Microgrid models having tuned PID controlled power converters of similar switching frequencies, generated reduced aggregated conducted electromagnetic interference relative to models having converters of different switching frequencies. It was also ascertained that having a pair of the common-mode and differential-mode EMI suppressing filters in the DC MG models, was more effective in reducing the EMI generation compared to models having four pairs of the EMI suppressing filters, i.e., having one pair of filters per each PID controlled power converter.

Declaration

I hereby declare that this submission is my own work and that, to the best of my knowledge and belief, it contains no material previously published or written by another person (except where explicitly defined in the acknowledgements) nor material which to a substantial extent has been submitted for the award of any other degree or diploma of a university or other institution of higher learning.

Signed ....

Date: 15/05/2022

Dedication

To my loving parents in heaven,

Mrs. Sushila Devi (17/07/1956 - 05/04/2010)

&

Mr. Krishna (29/08/1958 - 20/07/2021)

Acknowledgements

First, I would like to thank my research supervisor, Dr. Kosala Gunawardane, of Department of the Electrical & Electronic Engineering, Auckland University of Technology, for her invaluable support, guidance,and motivation throughout my research. Her extensive expertise in the power electronics & power systems have been a major advantage for my research. Undertaking this research full-time whilst working full-time sometimes became very challenging. However, she always ensured that I had sufficient time to complete all milestones, we had set. Her cheerful and positive nature helped me strive well in my research despite having a hectic work schedule.

This achievement would not have been possible without the love, care and support from my family, my sister-in-law Ranjana Wati, brother Avinesh Krishna, my loving nephew Avneel Krishna & my adorable baby niece Aavya Krishna.

Finally, I would like to extend my gratitude, respect, and appreciation towards my parents in heaven, Mrs. Sushila Devi and Mr. Krishna. Special thanks to my mother who always taught me to never give up and always strive to achieve my dreams.

Angaline Reshmi Krishna

15th May 2022

Table of Contents

List of Figures

List of Tables

Acronyms

Acronyms	Definitions
AC	Alternating Current
AC MG	AC Microgrid
CM	Common mode
CISPR	Comité International Spécial des Perturbations Radioélectriques, an IEC technical committee
DM	Differential-mode
DC MG	Direct Current Microgrid
EMI	Electromagnetic Interference
EUT	Equipment Under Test
FFT	Fast Fourier Transformation
SPV	Solar Photovoltaic
SMPS	Switched Mode Power Supply
PI	Proportional(P) and Integral(I)
PID	Proportional(P) and Integral(I) and Differential(D)
LISN	Line impedance stabilization network
dBμV, dBμA	0dBμV = 1 μV, 20 dBμA = 10 μA
PWM	Pulse Width Modulation
MOSFET	Metal Oxide Semiconductor Field Effect Transistor

Chapter 1 Introduction

1.1 Motivation

Globally, power systems are experiencing the trend of moving towards decarbonisation measures to mitigate environmental issues such as global warming, rising seas levels and climate change. This move has been accelerated due to the rise in fossil fuel depletion and drastic weather changes witnessed across the world. This has led to the engineers and scientists exploring alternative environmentally friendly energy supplies such as the Solar Photovoltaics (SPVs), wind turbines and various other renewable energy sources which are clean, green, and abundant in supply. However, integrating the Photovoltaics into the legacy power grids can pose new risks such as seasonal effects, supply security being compromised and the energy capacity of the base load, amongst others. Recent studies of the microgrids powered by photovoltaics have proven that the DC Microgrid (MG) is a promising power grid system due to its seamless interfacing with the DC dominant renewable energy sources, DC loads, and reliable and efficient energy storage systems. There are two types of DC MGs, namely the grid-tied ones connected to the main grid and the standalone ones which operate in an islanded mode.

Recently, an increased interest has been observed in the islanded mode DC MGs which has promoted the practical implementation and commercialisation of this technology. In comparison to the AC MG, the DC MG does not impose the same frequency throughout its system. The DC MG has simpler power electronic interfaces, is more resilient and also has fewer points of potential failure. The power conversion losses are less in the DC MG system in contrast to the AC MG systems as DC MGs employ simple DC-DC converters for their operations whereas the AC MGs must use several rectifiers (AC/DC convertors) and inverters (DC/AC convertors) according to their load demands. In Figures 1 and 2 below, the general configurations of the AC MG and DC MG are illustrated. EMI is relatively lower in the DC grids in contrast to the AC MG grids due to the switching voltage spikes caused by the rectifier diodes commonly found in the AC grids.

However, DC MG has its own limitations. The lack of awareness about the DC MGs is one of the biggest limitations, as is the case with any new emerging technology. Electrical contractors tasked with the installation and maintenance of this fairly new technology may not be sufficiently trained or competent which could substantially compromise with the system's integrity and safety.

Another limiting factor is the availability of solar PV generated energy is restricted to daytime only. Poor weather could also hinder the energy harvesting capability of the SPV.

The lack of government incentives to promote such a technology could also discourage any new users to try out the LV-DC MGs, particularly in remote rural locations where grid electricity is not available.

Finally, as with all new emerging technology, it would need time and open-mindedness to adopt and accept the true potential of the system.

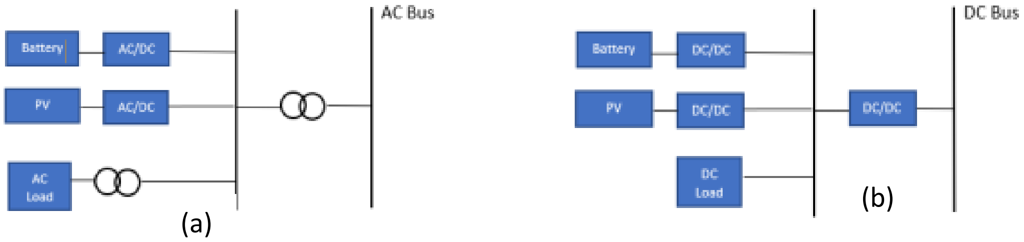

Figure 1: (a) General structure of AC MG (b) General structure of DC MG

In essence, the DC Microgrids are more resilient and tolerant of AC grid disturbances, thus giving improved power quality. However, the power quality in the DC microgrid is still sensitive to some issues due to the high frequency switching in power electronic converters. The most common power electronics converter used in DC MGs are the switched-mode power supply converters. These generate conducted and radiated electromagnetic interference (EMI) at their switching frequencies. In general, these converters are operated at frequencies in the range of 150kHz – 500kHz. If left unfiltered, the conducted EMI could cause operational interference in other neighbouring equipment. The radiated EMI could also be picked up by neighbouring equipment causing them to suffer operational malfunctions.

1.1.1 EMI

Electromagnetic interference (EMI) degrades the reliability of power converters and shortens the lifespan of circuit components [1][2].

Due to the rapid increase in the applications of high switching power converters, EMI generation has become a more concerning problem. Whilst fast switching ensures that the power supplies efficiency is improved, it inevitably causes noise problems. Higher frequency switching in the power electronic devices leads to rapid rise and fall times for the voltage and current waveforms. These fast edges generate high energy at very high frequencies which are the root cause of the EMI noise generation [3], as can be seen in Figure 2.

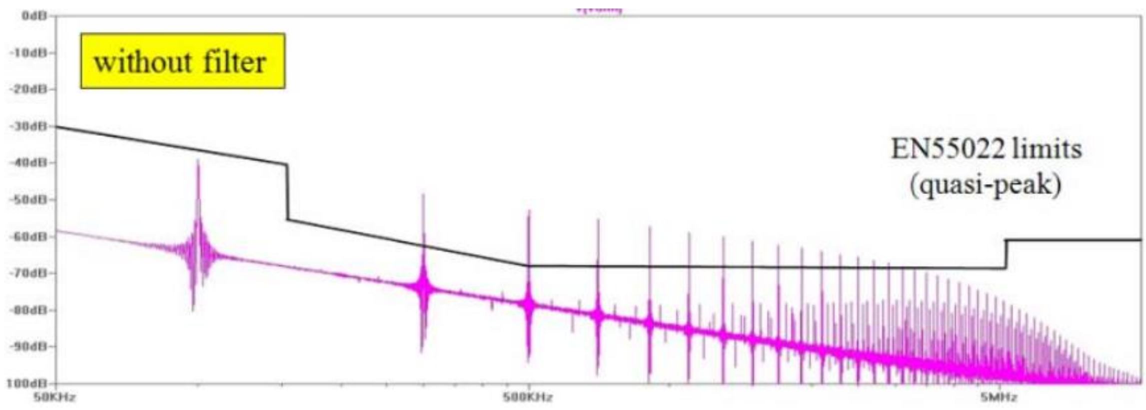

Figure 2: EMI frequency spectrum at high switching frequencies [3]

In summary, the overall EMI generation is lower in the DC MGs relative to the AC MGs, coupled with other advantages stated above. This implies that the DC MG as an emerging, new, and promising technology is worth investigating. This research aims to study the EMI issues arising in the Low Voltage Standalone DC Microgrid, due to its multiple DC-DC Buck converters and to present a simple, cost-effective yet efficient filter design to mitigate the EMI generation.

1.2 Research Objectives

The objective of this research is to develop and simulate a DC MG model to investigate the conducted EMI issues in DC-Microgrids due to its Power Electronic Converters, operating at various switching frequencies.

This research would be investigating different topologies of the DC MG to study the aggregation of the EMI generation arising as a result of various architectures of the DC-DC converters operating at various frequencies. The research will study the EMI effects by designing PI/PID controlled converters of similar and different switching frequencies to understand how these factors would affect the EMI generation.

To mitigate the effects of the aggregated conducted EMI, EMI filters would be incorporated into all the DC MG topologies. These filters would ensure that the EMI generation is suppressed as much as possible. Various design topologies to be studied, would include models with PI and PID controlled converters with single and four filters. The objective is to investigate the effect of increasing the number of EMI filters on the EMI generation.

1.3 Design Methodology

This study involved the analysis of the EMI emissions in DC Microgrid, due to the operations of its multiple power converters, of various switching frequencies. Figure 3 below, presents the research process undertaken to investigate the above problem:

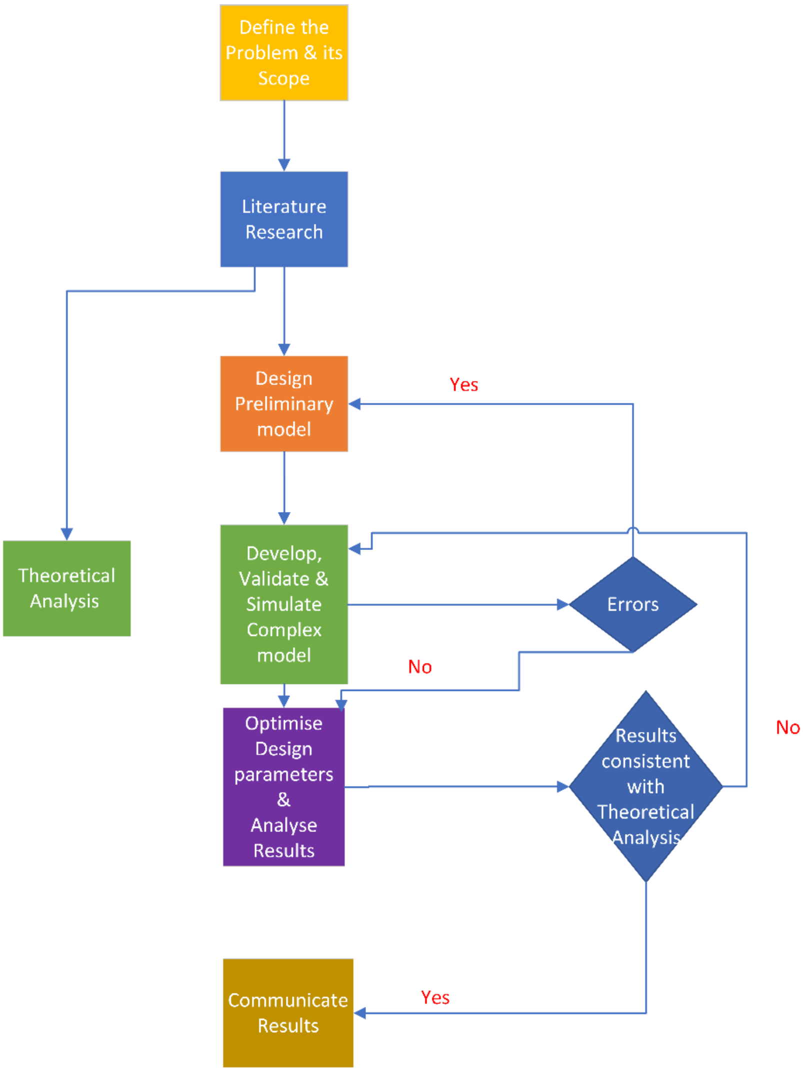

Figure 3: Research Methodology block diagram

1.4 Thesis Organisation

The remaining chapters are structured as follows:

Chapter 2 reviews existing literature concerning the power electronic converters used in the DC Microgrids, the generation of EMI, the existing methods to mitigate it and identify the research gaps.

Chapter 3 discusses the electromagnetic interference theory in detail.

Chapter 4 outlines the development of the DC Microgrid models and their various topologies to investigate the EMI emissions. It also presents techniques to mitigate EMI generation by the power converters.

Chapter 5 details a comprehensive account of the result outcomes of the simulating various topologies of the DC Microgrids. MATLAB/Simulink simulation outputs of the spectrum analysis were used for these purposes.

Chapter 6 presents a detailed analysis of the research findings and aims to provide mathematical analysis of the simulation results. The overall performance of the DC Microgrids, in terms of the aggregated conducted EMI generation, is discussed.

Chapter 7 draws conclusions and makes recommendations for the future work to further improve the aggregated conducted EMI emissions generated due to the multi-power converters operating at different switching frequencies.

1.5 Original Work & Publication

This research investigated the aggregated conducted EMI effects due to multiple Power Converters incorporated into a DC MG model, extensively, employing several DC MG model topologies. An extensive & detailed study of this nature has not been conducted to date.

As a result of this research, a conference paper has been published in the IEEE Xplore website:

1. (2021) Krishna A. R. and Gunawardane K., "EMI issues in LVDC-Microgrids due to Power Electronic Converters", *Proceedings of IEEE Tencon 2021, Auckland, New Zealand, 7th December – 10th December* 2021.

Another conference paper has been accepted for publication in the Electricity Engineers' Association (EEA) conference 2022:

2. “Investigation of the aggregated EMI generation in the LVDC Microgrids due to multiple DC-DC Converters”, in Electricity Engineers’ Association (EEA) conference 2022.

Chapter 2 DC Microgrids

2.1 Evolution of the DC Microgrids

Due to the high interception of the renewable energy sources and a surge in the usage of the modern DC loads, several pioneering research works have been dedicated to the development and utilisation of the DC Microgrid architecture. There are two modes of the DC MGs, namely the grid tied and the off-grid (islanded) DC MGs. Islanded or off-grid DC MGs are widely adopted in electric ships, smart buildings, and in some remote residential communities [4] where grid accessibility is not available. Figure 4 below illustrates a simplified DC MG model, incorporated with wind turbines and SPV as the renewable energy sources:

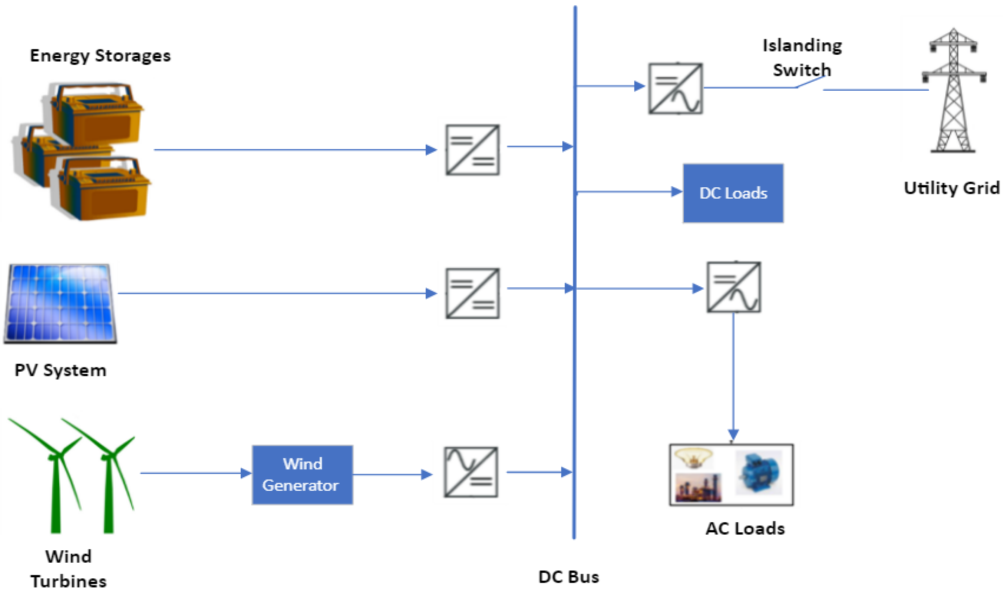

Figure 4: Simplified DC MG model

In Figure 5 below, it can be seen that the DC MG models have fewer converter stages than the AC MGs(fig. 6), thus being a more favourable architecture due to reduced converter losses. The power conversion losses are smaller in the DC MG system in contrast to the AC MG systems as DC MGs employ simple DC-DC converters for their operations whereas the AC MGs must use a variety of rectifiers (AC/DC convertors), inverters according to their load demands.

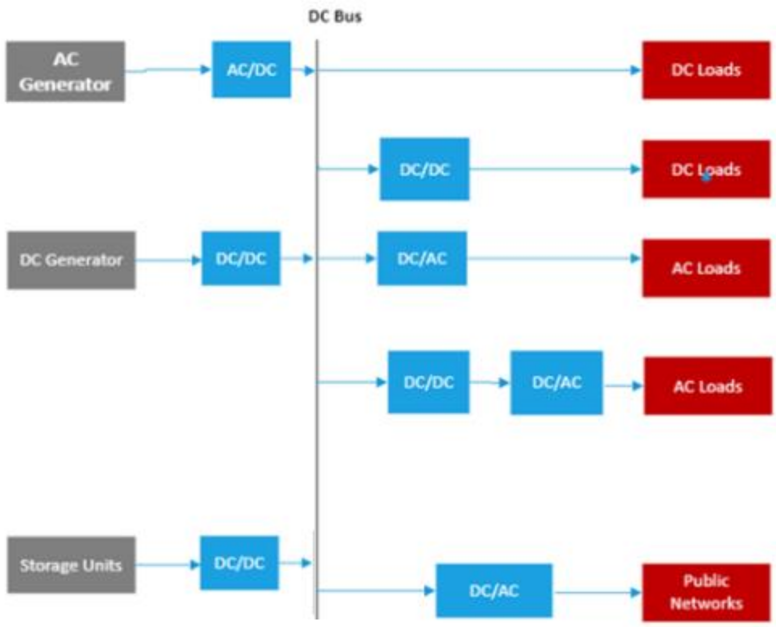

(a)

Figure 5: General structure of DC MG

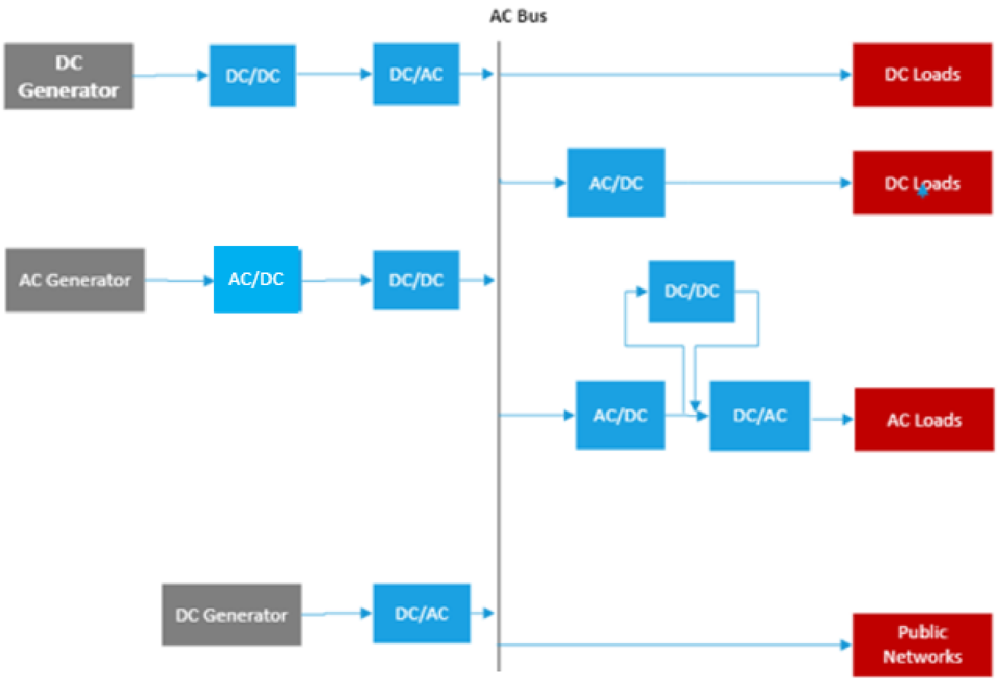

(b)

Figure 6: General structure of AC MG

2.2 DC Standards

For the development of the Future Architecture (FAN) of the Power Systems Network, having proper DC standards is extremely important. The existing DC standards facilitate the developing of various stages of the LV and MV DC MGs for both residential and industrial consumers [5].

Currently, trade organisations around the world are working on standardising the DC specifications. These are Emerge Alliance, an American industry association, tasked to promote the DC MGs in energy efficient establishments, the IEEE Standards Association which is working on developing global DC standards and the IEC (International Electrotechnical Commission), responsible for preparing and publishing the standards [5].

2.2.1 Standards for developing DC MG models

IEC recommends $380V_{DC}$ as suitable optimum voltage level of the DC power distribution and suggests $24V_{DC}$ and $48V_{DC}$ as appropriate for auxiliary DC voltage levels. IEEE Std 1547 provides information on interfaces of the DC power distribution and equipment. ETSI ES 203 474 V1.1.1 is the most suitable standard for interfacing of the renewable energy systems and general power architecture. ITU-T L.1205, on the other hand, specifies how to integrate the renewable energy source into a DC power system such as the DC MGs. As for battery storage systems in a DC MG model, IEEE Standard 946 provides the recommended practices for the design.

Overall, globally, the preferred nominal DC bus voltages for the LVDC distribution system so far appear to be 12V, 24V, 48V, 380V and 400V [5].

2.3 Impact of the EMI on the DC Microgrids

Solar Photovoltaic powered microgrids generate DC power which is supplied to the DC loads by power converters converting the voltage to appropriate levels, according to load demands. During this process, EMI is produced as radiated(propagated through space) and conducted EMI(propagated through groundings, etc) [6], [7]. PV modules which are formed by connecting multiple solar cells, start to act like transmitting antennas and emit radio frequency noises into the environment as well as pollute the grid. These modules are also susceptible to radio frequency signals from ambient and nearby equipment, resulting in converter failures in the microgrid.

On the other hand, fast switching on and off power converters in the DC microgrids, which are normally pulse width modulated(PWM), are major cause of the generation of the undesirable conducted EMI. This happens due to the high rates of voltage and current changes. Conducted EMI can negatively affect HV/LV DC – DC converters in a system, thus affecting its system's performance and safety. It also has the capability to cause the radiated EMI of the converters to exceed the standard EMI limits [8]. More detailed discussions about the electromagnetic interference would be presented in chapter 3.

2.4 Research Gaps

Several techniques have been presented in the literature to mitigate the EMI issues. However, the literature research has proved that, to date, extensive research on the EMI issues faced by the DC Microgrids due to its power converters, has not been performed. The focus of such studies has mostly been around the power converters in various electrical architectures, such as electric vehicles(EVs), aircrafts, etc . Literature research has shown that very limited work has been conducted in investigating the EMI emissions due to multiple converters being present in the low voltage DC Microgrid models. There is much potential for investigating and improving the power quality issues faced by the DC Microgrids due to these EMI issues. This research has explored this area in detail and presents its key findings in the upcoming chapters.

To improve the power quality issues in the DC Microgrids, this research has proposed, developed, and analysed several topologies to study different scenarios and present its comprehensive findings. It is also hoped that the research findings would add to the current rich knowledge base of the Future Architecture of the Network; a project whose major research hypothesis is the high insertion of DC transmission and distribution into the existing AC grids, which would enable the transition to low carbon power systems [9].The next chapter will discuss the electromagnetic interference arising in the DC MG due to its DC-DC converters.

Chapter 3 Electromagnetic Interference

3.1 Characteristics of the Electromagnetic Interference

Electromagnetic Interference (EMI) is a type of an electrical-noise pollutant which has the ability to degrade an electronic device's reliability and shorten its lifespan [10]. It also has the potential to threaten and compromise the safety and performance of the DC Microgrid equipment and its overall system [11].

For this reason, all electronic systems require compatibility with their EMI environment, where several other EMI emitting sources may be present.

Switched mode power supplies (SMPS) such as the DC-DC Buck converters are common sources of EMI noise emission from DC MGs. The SMPS in question often have high switching frequencies which lead to high emission of the EMI due to higher di/dt and dv/dt. This causes switching noise in the control loop and in the rest of the system [11].

Generally, control of EMI is one of the most challenging aspects of a SMPS design so as to prevent other electronic devices from causing operational interferences. Some techniques for reducing the EMI emissions in the SMPS are filtering, minimising current loops, shielding, etc. For this reason, the buck converters are extremely useful devices on which to study the mitigation of EMI issues. [2][13].

3.2 EMI Sources

In figure 6 below, the common culprits causing the EMI issues in the buck converters can be seen.

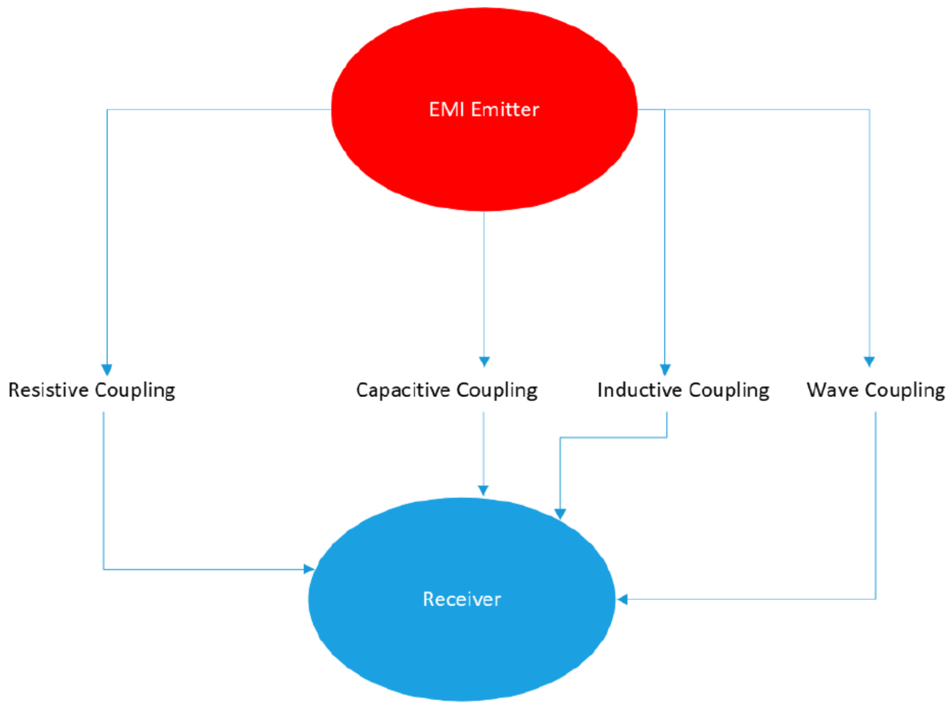

Figure 7: Sources of EMI

EMI can be classed into two modes which are the conducted and the radiated EMI. These modes are determined by the method in which their EM field propagates. Noise coupled via the conductors or through parasitic capacitance, power or grounding connections is how conducted EMI propagates. On the other hand, radiated EMI is any unwanted noise coupling via radio transmission. This radiated noise propagates through the free space/air as magnetic fields and is commonly controlled by employing metal shields to contain these fields within the device enclosure.

3.3 Conducted EMI

Conducted EMI is one of the most challenging noise sources to eliminate in a SMPS device such as a Buck converter [15]. The shape of the conducted EMI is determined by the source of the interference as well as the parasitic couplings in the circuit [15]. Recent studies have shown that it is usually more prevalent in the frequency range between 150kHz and 30MHz [16]. According to current industrial practices, only conducted EMI below 30MHz is considered when the EMI issues are investigated [19].

The conducted EMI can be further classified into the Common-mode (CM) and the Differential-mode (DM) EMI. These two modes are considered to be major EMI pollutants due to their ability to interfere with safety critical systems in their vicinity. To prevent such occurrences, the regulatory bodies such as the International Electromechanical Commission (IEC) have set several emission standards for monitoring such emissions.

3.3.1 Common-mode (CM) EMI

CM noise signals are asymmetric or longitudinal in nature, are voltage driven, and are associated with electric fields, high impedance, and high slew rate (dV/dt).CM noise voltage is calculated using equation 3.1 [17]

$$|V_{CM}| = \left|\frac{v_{Line\,1}+v_{Line\,2}}{2}\right|,$$

where $V_{Line\ 1}$ and $V_{Line\ 2}$ are the noise voltages. (3.1)

3.3.2 Differential-mode (DM) EMI

DM noise signals are symmetrical or transverse in nature, current driven, and associated with the magnetic field, low impedance, and fast current switching (di/dt). DM conducted noise is due to the intrinsic converter switching action and propagates in the opposite directions in the positive and return power lines. DM propagates in a closed return path in a small loop area. DM noise voltage is calculated using equation 3.2[17]:

$$|V_{DM}| = \left|\frac{v_{Line\,1}-v_{Line\,2}}{2}\right| \quad (3.2)$$

3.4 Radiated EMI

The radiated EMI emission is air-borne, and its far field electric field intensity E is used for its measurement [19], as can be seen in equation 3.3 below [13]:

$$|E_C| = 6.28x10^{-7} \times \frac{IfL}{d} \quad (3.3)$$

Where,

E_C = Electric field strength(V/m)

I = Net current on the PCB section

f = Frequency (Hz)

L = Length of the PCB trace(m)

d = Radial distance from the origin(m)

The radiated emission may degrade the performance of nearby sensitive electronic devices. According to the international standards, radiated EMI frequency range is between 30MHz to 3GHz [13]. The fundamental mechanism of the radiated EMI is:

- Power cables acting like an antenna for the radiation
- Radiated EMI mainly driven by CM noise

Simulation techniques can be applied to obtain the radiated EMI from any circuitry using software such as LTSpice, etc [13].

3.5 Acceptable levels of EMI

Several regulatory bodies monitor the permissible levels of the conducted and radiated EMI generated by the electrical systems so as to maintain the electromagnetic compatibility. For this purpose, a thorough understanding of the EMI standards pertaining to different applications is crucial [23]. The frequencies of interest for the EMI study lies within 150kHz – 30MHz. Frequencies between 2kHz to 150kHz are not generally considered as the EMC standard IEC 61000-6-3 does not apply to frequencies below 150kHz [23]. CISPR 11 is the international standard for EMI disturbances emitted by industrial, scientific, and medical RF equipment. The 6th edition of the CISPR 11 standard (2015) is subdivided into class A and class B. CISPR 11 class B uses limits used by CISPR 22/32, whilst class A depends on the power level of the equipment under EMI assessment [23]. Figure 7, below, shows the class A conducted EMI levels permissible for various frequencies, using quasi-peak and average signal detectors, for different groups of equipment.

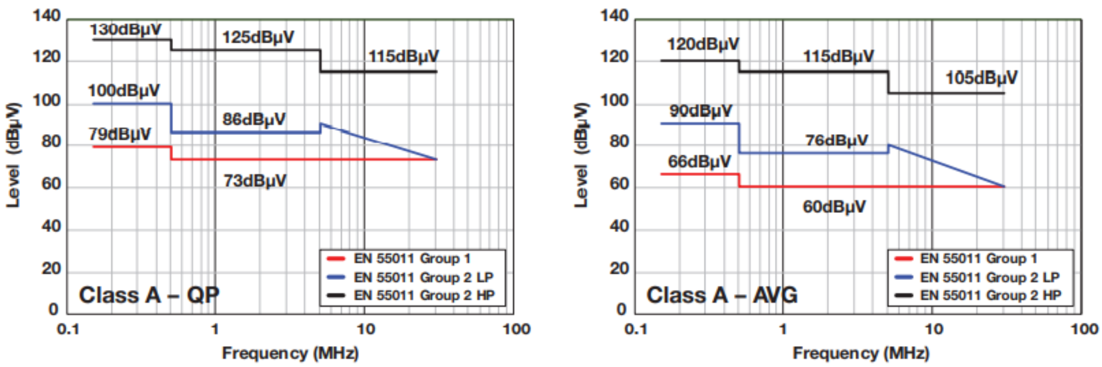

Figure 8: CISPR 11/EN 55011 Class A conducted EMI [19]

The IEC standard IEC 61000-6- 3 targets residential and commercial applications. The table below illustrates the standards for various products which may be used as DC loads in the residential LV DC MG models:

Table 1: International standards for determining the permissible limit values for the conducted [20][21][22]

Product Sector	CISPR Standard	EN Standard	FCC Standard
Household appliances	CISPR 14-1:2020	EN 55014-1	–
Lighting equipment	CISPR 15	EN 55015	Part 15/18

3.6 EMI modelling

3.6.1 Line Impedance Stabilisation Network (LISN)

The LISN is a passive low pass filter with a π configuration, which is used to measure the common-mode (CM) and the differential-mode (DM) conducted EMI emitted by the DC-DC converters. For repeatable measurements, a LISN is utilised to decouple the power line and the EUT (Buck converter). It is connected between the power source and the Buck converters (SMPS under test), in series, to ensure the reliability and comparability of the measurement. The conducted EMI/noise is measured by the spectrum analyser, through an RF connection to one of the LISN's ports [25]. An EMI separator in the LISN ensures that both the CM and DM EMI can be measured simultaneously. Figure 8 illustrates a basic LISN circuit topology.

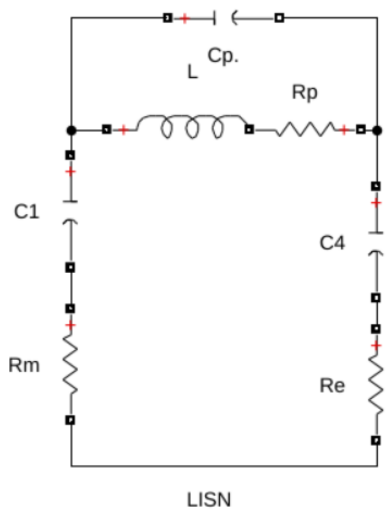

Figure 9: Schematics of a LISN circuit incorporated with parasitic elements

A LISN circuit, in practice, may change the impedance of the input power lines. Therefore, an impedance calibration of the LISN circuit via a Network Analyser is recommended. Having a low pass filter for the input power line and a bandpass filter for the frequency range of 150kHz – 30MHz would also help in stabilising the input impedance of the LISN [16].

For practical purposes, the value of the solenoid inductor, usually used in the LISN is given by the Wheeler relationship as shown by equation 3.4 [16], below:

$$L = \mu_0 n^2 \text{a (In (1 +} \left(1 + \frac{\pi a}{b}\right) + {}^{1}\Big/\left(2.3 + \frac{1.6b}{a} + 0.44\left(\frac{a}{b}\right)^2\right) \qquad (3.4)$$

Where a, b, μ_0, n^2 are the radius, axial length, permeability of free space, number of turns in the coil, respectively. The capacitance value, C_p of the above inductor can be obtained using equation 3.5 [16]:

$$C_p = \frac{1}{N-1} \times \frac{2\epsilon_o \pi D \times tan^{-1}\left(\sqrt{1+\frac{2}{\frac{1}{\epsilon_r} ln\frac{d_o}{d_i}+\frac{s}{d_o}}}\right)}{\sqrt{\left(1+\frac{1}{\epsilon_r} ln\frac{d_o}{d_i}+\frac{s}{d_o}\right)^2 - 1}} \qquad (3.5)$$

Where d_o = outer diameter of conductor, d_I = inner diameter,

s = air gap between conductors, ϵ_r = relative permittivity of the insulator and ϵ_o= air permittivity.

3.7 Techniques to mitigate the EMI in Power Converters

The use of the DC MG model to study the EMI emission arising due to the interactions between its fast-switching power converters is an interesting research area. The main objective of this study is to improve the power quality of the DC MG models. Ciarpi, G. et al. 2020, discuss the inductor-less DC-DC Converter design in order to reduce the EMI generated by the classic Switching Mode power supply. This would enable the size and weight of the onboard electronics in future spacecraft to be reduced by foregoing the metal shields [26]. Figure 9 illustrates the proposed multistage DC - DC converter topology, which can operate with a wide input voltage range of 6V - 60V.

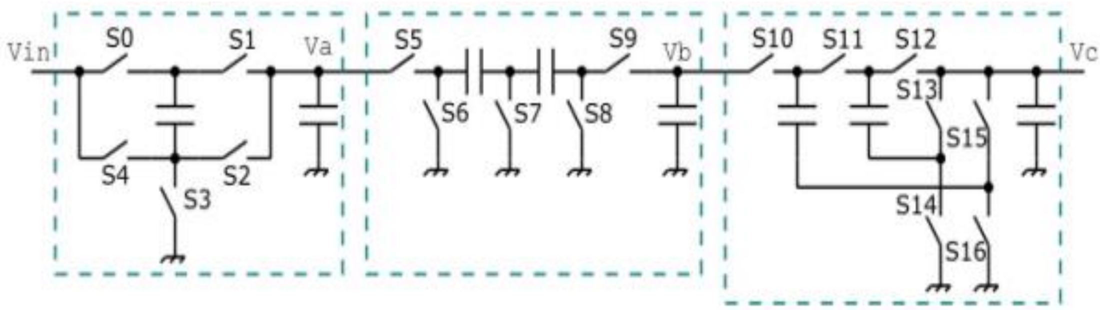

Figure 10: Switched Capacitors DC-DC converter [24]

Zhangi, Z. et al. 2017, propose a new Pulse Width Modulation (PWM) method to mitigate the EMI issues caused due to the bidirectional grid connected power converter. The electric vehicles (EV) connected to such grids through Vehicle to Grid (V2G) technology, often experience complex EV EMI environments due to frequent energy exchange. This could result in the impairment of performance in surrounding auxiliary electronic devices causing reduced stability for EVs. The proposed technique is based on employing the PWM technique to use random-like series to control the duty cycle and the switching period of the DC-DC converter. This would suppress the peaks in the conducted EMI by evenly distributing the harmonics over a wide range of frequency, both in the charging and discharging modes, thereby improving the power quality of the power grid [27]. Laour, M. et al. 2017, present a simple method to minimise the conducted and radiated EMI emissions in the switching noise zone of DC-DC converter system. This reduction was made using the ground inductors (BRC-220U). No input or output filters were used. This technique helps reduce the EMI levels to around 30dB. The model was simulated in MATLAB/Simulink environment in the time domain. Figure 10, below, shows the measurement setup of the radiated and conducted EMI emissions. Figure 11 displays the insertion points for the ground inductors in the model to minimise the EMI effects [28].

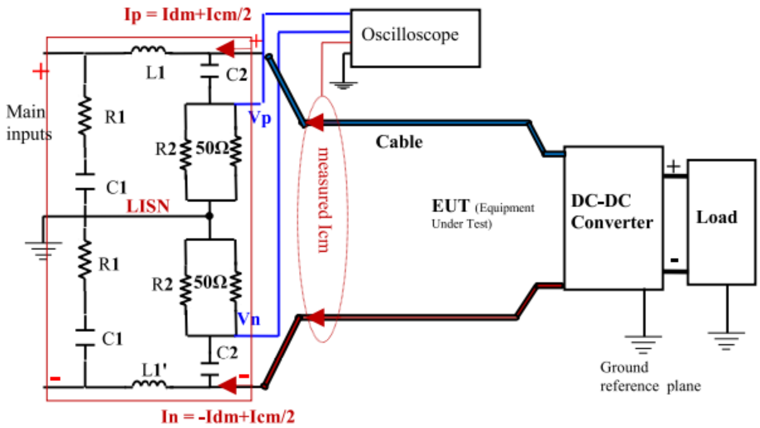

Figure 11: Schematics of the measurement setup of the conducted and Radiated EMI [28]

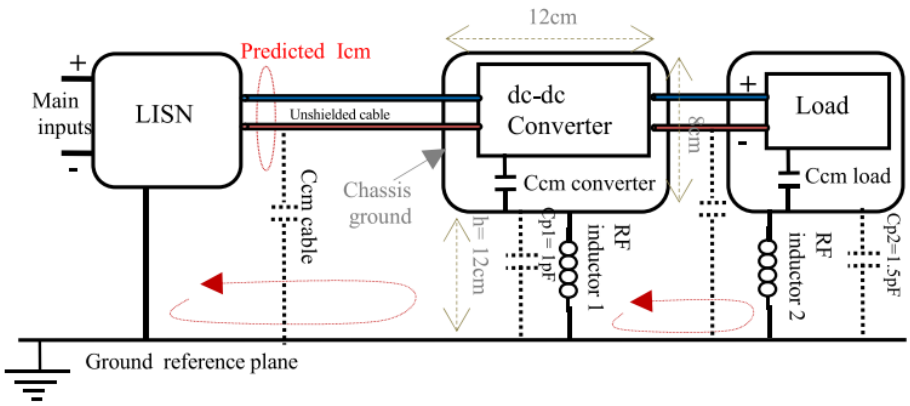

Figure 12: Insertion of the ground inductors in the Simulink model [28]

Karimi, S. et al. 2021 describe unscented Kalman filter (UKF) method to deal with the non-linear and stochastic nature of the EMI and to measure the noises. This proposed method was tested on the conventional DC-DC Buck converter using the dSPACE1104 development environment. The UKF method was used to estimate the parasitic capacitance in real time, which is essential for the adjustment of the EMI filter in the EV system where the parasitic capacitance keeps varying due to the environment (temperature, humidity, etc) it is in. Details of the UKF algorithm can be found in [29]. Shirai, R. et al. 2021 propose an EMI failure protection technique that facilitates the protection of the Controller Area Network (CAN) communication against the EMI generated by the Buck converters. When the CAN sampling point coincides with the switching time of the converter, a communication failure can occur. Thus, the Timing Control Shift (TSC) avoids the coincidence between the CAN sampling time and the induced noise. This method has the potential to be an effective solution for EMI mitigation. Details of the TSC method are presented in [30]. Muller, D. et al. 2021, have mentioned that due to rising voltages and wide bandgap, semiconductors in the power converters are the main cause of increasing EMI generation in EVs. Typically, active filters are complex to design, and the passive LC filters limit the power density improvements. Therefore, Muller et al. have proposed the use of simple half-bridge gate driver ICs to compensate the EMI emitted by the DC - DC converters. This method is extended by the Predictive Pulsed Compensation (PPC). To suppress the EMI, two level compensation pulse is utilised. The generation of this pulse is performed using the MOSFET half bridge. The PPC offers an efficient and simple design to suppress the EMI in DC- DC converters and provides potential to minimise the EMI filter size, significantly [31].

Chapter 4 Design of the DC Microgrid model

4.1 Architecture of the DC Microgrid model

The DC Microgrid model was designed using the DC Microgrid project found in the Microgrid Project [32]. An islanded model of the Low Voltage DC Microgrid comprising multiple DC buses at three different voltages levels were designed for residential consumers. The design incorporated DC Microgrid standards, the standards for the DC bus design for the 12, 24 and 48V DC buses [5] and the DC-DC converters design to produce a practical, low noise, high power quality and efficient DC MG model, as illustrated by Figure 12 below.

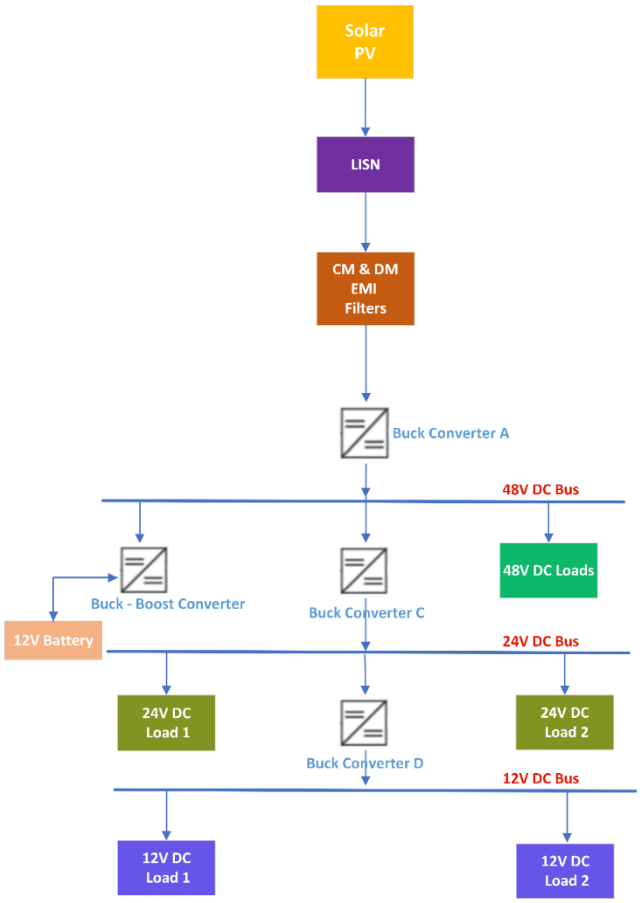

Figure 13: Architecture of the fully developed DC Microgrid model used in the research

4.2 Software used for simulation

MATLAB/Simulink version R2021b software was used to model and simulate the DC Microgrid in the frequency-domain to obtain the conducted EMI results. This software is one of the most commonly used Microgrid systems modelling tools for performing power systems design and analysis. It provides the flexibility and creativity to develop and analyse large scale models under various case conditions [33]. A physical modelling approach using the MATLAB/Simulink software can ease the tedious and complex mathematical modelling typically required for the EMI Spectrum analysis.

4.3 Design Phases

4.3.1 Basic DC MG model

This preliminary model (Figure 13) was created at the initial stage of the model development.

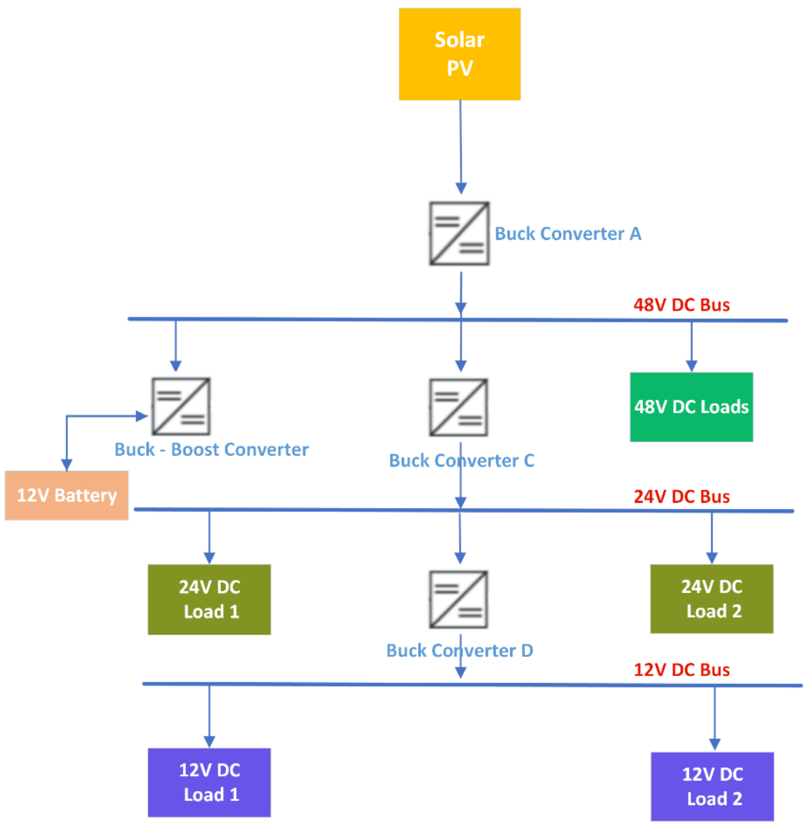

Figure 14: Basic DC Microgrid model

The purpose was to design a basic DC MG model, run several iterations of the simulations to check for errors(voltage outputs) and further develop the model with add-ons(LISNs, EMI filters, etc) once it had been simulated and tested. In this basic model (fig 13), the power converter switching frequencies were kept the same for all the converters. The aim was to create and simulate a very basic DC Microgrid model and verify that its simulation results, in terms of the solar PV rating, various DC loads, power converter's current and voltage outputs, were consistent with the calculations. Its simulation results were validated with the results from the mathematical analysis, which would be discussed in the next chapters. The following sections present the DC Microgrid model at the components level and provide a detailed design description of each component.

4.4 PV Array

Renewable energy sources such as standalone Solar Photovoltaics (SPVs) are experiencing increased popularity [32] and potential in comparison to the wind powered electrical system [12]. The solar PV (SPV) array (Figure 14) has been selected as the power source for this design since the SPVs have lower maintenance costs, have no moving parts and solar energy is abundant in nature, compared to other renewable energy sources. SPVs' easier installation at consumer load premises (commercial and residential buildings) makes them a more attractive choice for this reason [35].

Figure 15: A Rooftop SPV system

A Simulink model of the PV module is incorporated into the DC MG model to simulate the real time power harvesting process by the PV system. It consists of a number of photovoltaic cells connected in parallel and in series. Series connections offer higher voltage generation, whilst parallel connections generate higher currents. Therefore, the PV arrays can be designed (sized) according to their total power requirement [12]. The Simulink model of the SPV comprised of 40 parallel strings with each string having 10 series connected PV modules. Table 2 exhibits the PV system design parameters.

Table 2: PV Array Design Parameters used in the DC Microgrid model

MATLAB/Simulink PV Array	
Parallel connected string	40
Series connected module per string	10
Cells per module	60
V_{OC} | I_{SC}	36.3V | 7.84A
V_{MMPT} | I_{MMPT}	29V | 7A

Where V_{OC} = open circuit voltage (under no load condition) of the solar cell, I_{SC} = short circuit current, when the positive and negative terminals of figure 16 (below) are shorted,

V_{MMPT} & I_{MMPT} = voltage and current achieved when the SPV is producing the maximum power, respectively.

Irradiance and temperature affect current and voltage of the SPV, respectively. As the irradiance increases, so does the current, whilst the voltage remains unchanged. Similarly, as the temperature of the SPV increases, the output voltage decreases. To optimise the operation of the SPV system at Maximum Power Point, an efficient, fast, and accurate algorithm such as the Perturb and Observe method is used [36].

Figure 15 below displays the IV and the PV characteristics of the SPV, at 25˚C, used in the DC MG model. By setting the irradiance of the SPV array to 1000 W/m^2, a maximum output voltage of 290V was achieved.

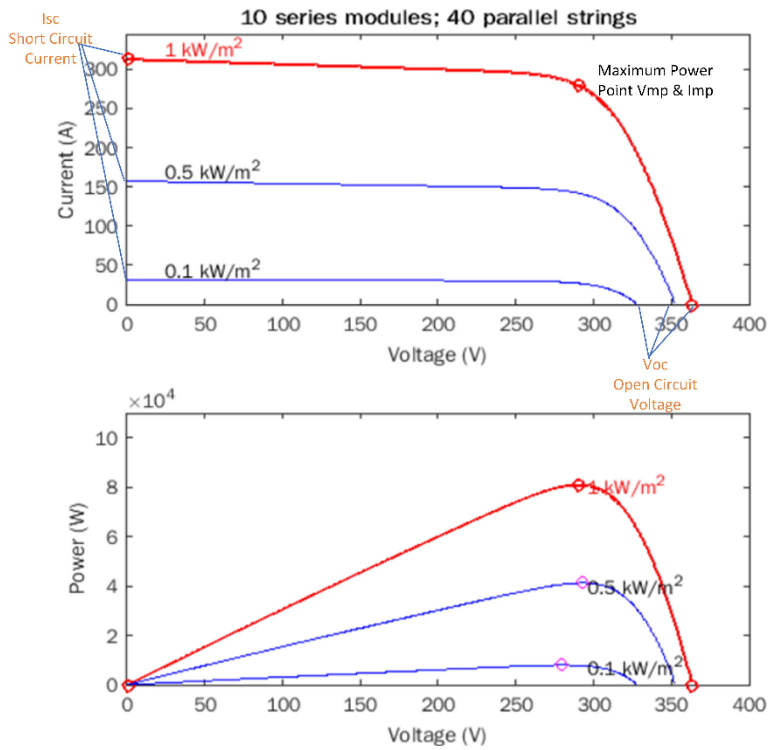

Figure 16: I-V and P-V output characteristics of the SPV module of the DC MG model, for different irradiances

4.4.1 PV Module modelling

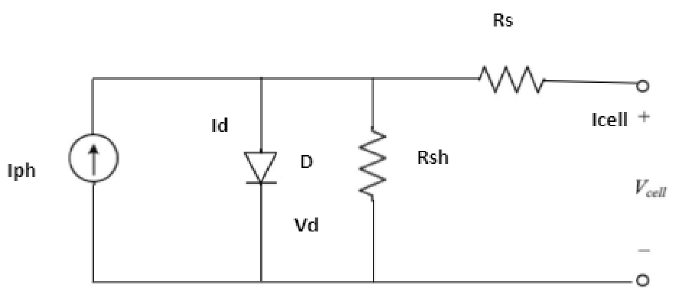

Figure 17: Equivalent circuit of a SPV cell

A single SPV cell consists of a current source I_{ph}, a diode D, a series R_s and a shunt resistor R_{sh}. The ideal solar cell model is represented by equations 4.1 – 4.5 (below):

$$I = I_{ph} - I_o\left[e^{\frac{V_d}{AV_t}} - 1\right] \qquad (4.1)$$

Where I_o = reverse saturation current (A); V_d = diode voltage, A = diode ideality factor and V_t = thermal voltage

$$V_t = \frac{kT}{q} \qquad (4.2)$$

Where k = Boltzmann constant = 1.38 x 10^{-23}J/K, T = solar cell temperature (°K) and q = electron charge = 1.6 x 10^{-19}C

Solar cell temperature, $$T = 3.12 + \frac{0.25G}{G_{ref}} + 0.899T_a - 1.3W_s + 273 \qquad (4.3)$$

Where G is the irradiance intensity (W/m^2), G_{ref} = reference irradiance of 1000 W/m^2, W_s = local wind speed in m/s

The photocurrent I_{ph} in fig. 16, is given by equation 4.4 below:

$$I_{ph} = \frac{G}{G_{ref}}\left[I_{sc,ref} + \mu_{I_{sc}}\left(T - T_{ref}\right)\right] \qquad (4.4)$$

Where $I_{sc,ref}$ = solar cell short circuit current at reference condition of G_{ref}, T_{ref} = 25°C & Air mass = 1.5, and $\mu_{I_{sc}}$ = solar cell's short circuit temperature coefficient.

Finally, equation 4.5 [31] describes the IV output characteristics of a SPV module:

$$I = I_{ph} - I_o\left(e^{\frac{V+IR_S}{AV_t}} - 1\right) - \frac{V+IR_S}{R_{sh}} \qquad (4.5)$$

4.4.2 Maximum Power Point Tracking

The Maximum Power Point Tracking (MPPT), a charge controlling technique, is imperative in the SPV systems for extracting maximum output power from the PV modules. Different DC-DC converter topologies help transfer the maximum power from the SPV to the loads; this will be discussed later.The maximum power delivery capability of the SPV varies with the randomly changing irradiation from the sun and the surrounding temperature. These parameters influence the peak power harvesting capability achievable by operating the PV system at different points of the PV curve (refer to Figure 15). Maintaining the terminal current and voltage of a PV array to match the maximum power delivery, is known as Maximum Power Point Tracking (MPPT). Employing the MPPT into the SPV system, increases its overall efficiency [38]. Figure 17 below shows the incorporation of the MPPT controller into a DC-DC converter.

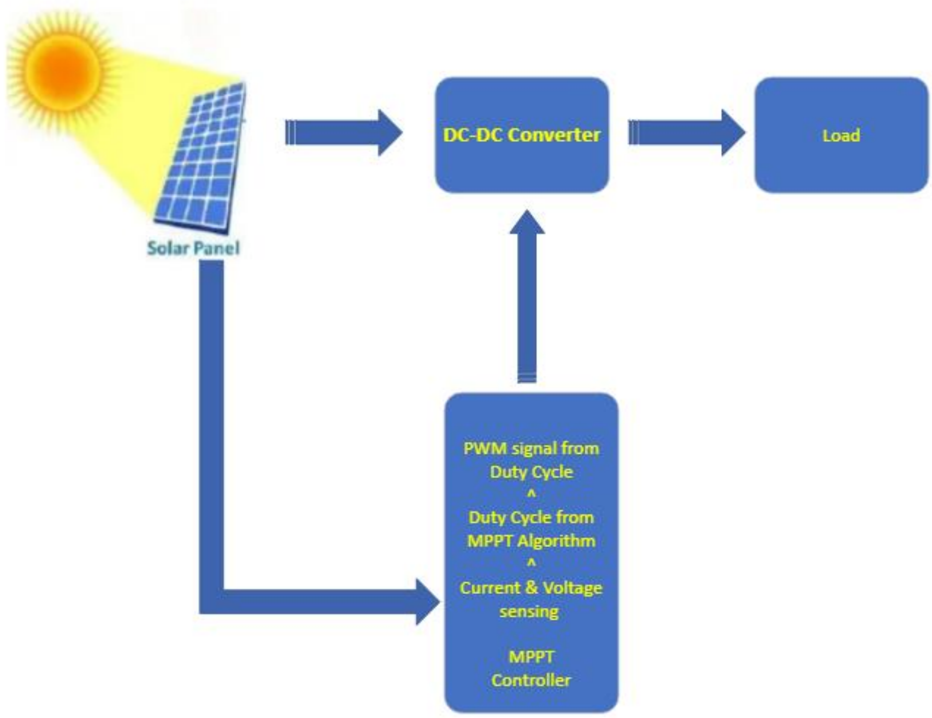

Figure 18: Block diagram illustrating how the SPV was incorporated with MPPT in the model

4.4.2.1 Perturb & Observe (Hill climbing-search algorithm)

Perturb and Observe (P & O) is one of the most commonly used MPPT technique, for SPV systems, in the industry [37]. This technique introduces a minor pertubation into the PV module to cause the power variation. The output power, *P(k)*, is periodically measured and compared with the previous power, *P(k-1)*. The same procedure is applied if the output power increases. If this isn't the case, then the perturbation is reversed. To check whether the output power has increased or decreased, the PV module voltage *V(k)* is increased or decreased. An increased voltage means an increase in power; therefore, this implies that the operating point of the PV module is towards the left of the Maximum Power(refer to the top graph of Figure 15). This means that further perturbation is required on the right to reach the Maximum Power. On the contrary, if an increased voltage leads to a decreased power, then the operating point of the PV is located at the right side of the Maximum Power and requires further perturbation on the left to achieve the required Maximum Power Point [38].

Figure 18 displays the Simulink model of the Perturb and Observe MPPT block used in the DC Microgrid model. Figure 19 shows the conventional P & O algorithm used in designing the P & O Simulink model:

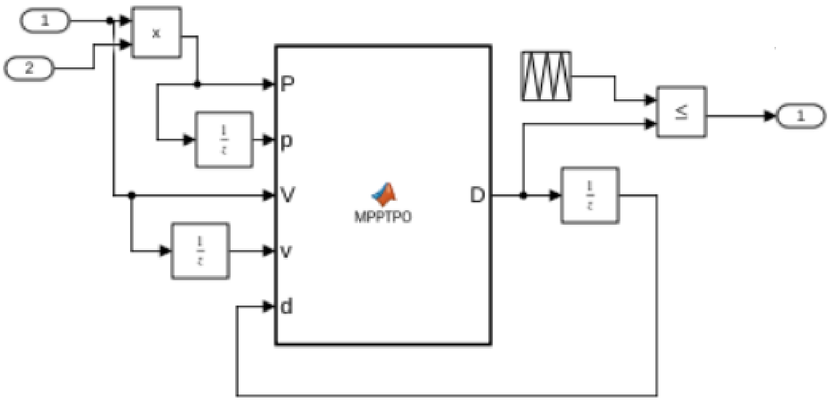

Figure 19: Simulink model of MPPT of the DC MG model

Four different MPPTs were designed for four DC-DC converters according to their load demands. The duty cycle of each MPPT is controlled by the P & O MPPT algorithm to achieve the required output voltage of the converter.

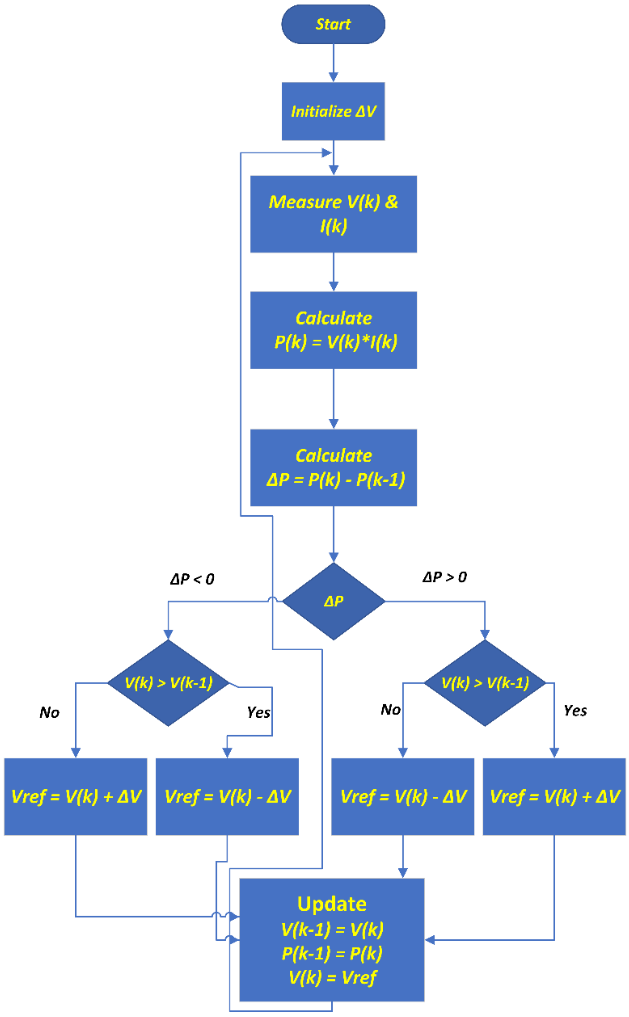

Figure 20: Flowchart of P & O method used in the MPPT in the model

4.5 Battery Energy Storage system (BESS)

A 12V BESS is connected to the DC Microgrid via a bidirectional buck-boost converter. Its function is to provide voltage regulation when the DC bus voltage (12V) experiences fluctuations. It can operate in Constant Current (CC) – Constant Voltage (CV) charging and discharging modes for voltage control [39]. When the 12V battery discharges to the 48V DC bus, the BESS operates in boost mode. Conversely, when the battery consumes power, the BESS operates in the buck mode [40]. The circuit diagram of the buck and boost mode is displayed in figure 20, below.

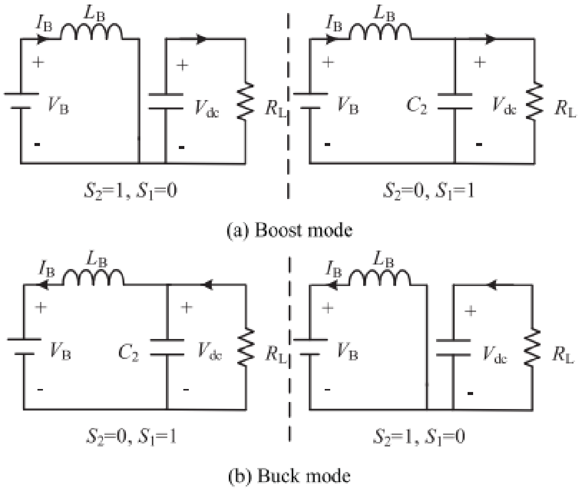

Figure 21 Topologies of boost and buck mode

The Lithium-Ion (Li-ion) battery has been selected for energy storage due to its superior characteristics and performance, relative to the other battery types available. Li-ion batteries are recycleable, have a highly accurate state of charge (SOC) estimation, low self discharge rate [41], cost less and are lightweight with high power density [42]. The built-in Simulink block model of a Lithium-ion battery[43][44] was used in the DC Microgrid model. Figure 21, below shows the equivalent circuit of the battery model, corresponding to the battery model used in the design.

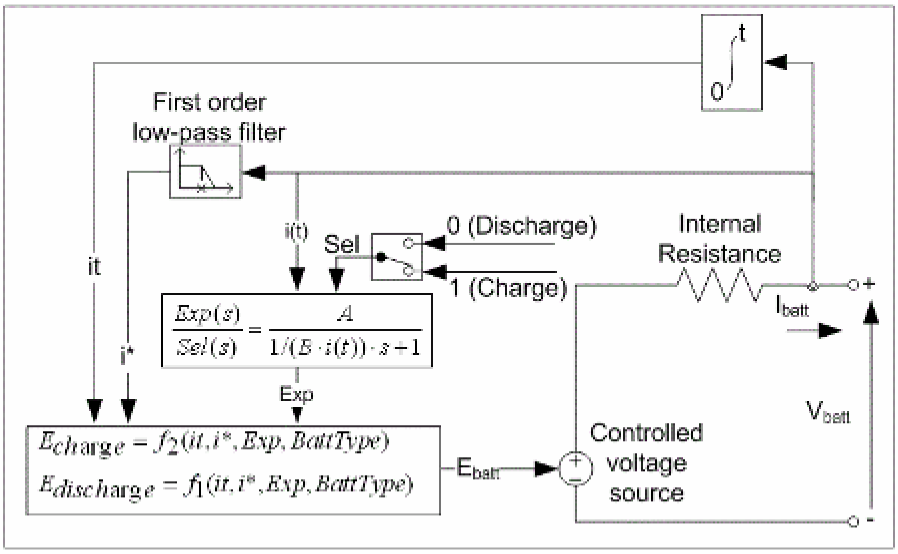

Figure 22: Equivalent circuit of the Simulink model of Li-ion battery used in the model

Table 3 displays the extracted battery data list from its Simulink model.

Table 3: Li-ion battery specifications

Parameter	Value
Initial State of Charge (SOC)	55%
Nominal Voltage	12V
Rated capacity	5.4Ah
Maximum capacity	5.4Ah
Fully charged voltage	12V
Nominal discharge current	2.3478A
Internal resistance	0.022222Ω
Capacity at nominal voltage	4.8835Ah
Exponential zone	12.9646V, 0.265304Ah
Nominal ambient temperature	20°C
Maximum capacity	4.8Ah
Initial discharge voltage at 0°C	7.1V
Voltage at 90% maximum capacity at 0°C	5.655V
Thermal resistance (estimated cell to ambient)	0.6°C/W
Thermal time constant (estimated cell to ambient)	2000s

4.5.1 Charging and Discharging characteristics

Figure 22 illustrates the discharging characteristics curves of the Li-ion battery used in the DC Microgrid model. The yellow region shows the exponential voltage drop when the battery is fully charged. The grey section represents the extractable charge until the voltage drops below the nominal value. Lastly, the blue curve shows the total discharge of the battery when the voltage discharges rapidly. A fully charged Simscape battery model would take 2.3 hours to fully discharge, according to equation 4.6 and the battery specification provided in Table 3.

$$(h) = \frac{Battery\ Capacity(Ah)}{Nominal\ Discharge\ Current(A)} \qquad (4.6)$$

where (h) is the time in hours taken to fully discharge the battery.

For real world applications, a higher capacity battery could be used to provide energy storage for longer period of time compared to the battery model shown above which completely discharges in 2.3 hours. The discharge characteristics curves shown in figure 22 have been calculated using equation 4.7 below. It shows that for different current values, as the load current increases, the discharging of the battery would be faster, as expected.

Discharge curve ($i^* > 0$) equation 4.7 [38] is given by:

$$f_1(it, i*, i) = E_o - K.\frac{Q}{Q-it}.i* - K\frac{Q}{Q-it}.it + A.exp(-B.it) \qquad (4.7)$$

where E_o = constant voltage (V), K = polarisation constant (V/Ah)

$i*$= low-frequency current dynamics (A), i = battery current (A), it = extracted capacity (Ah),

Q is the maximum battery capacity (Ah) and B = exponential capacity (Ah^{-1})

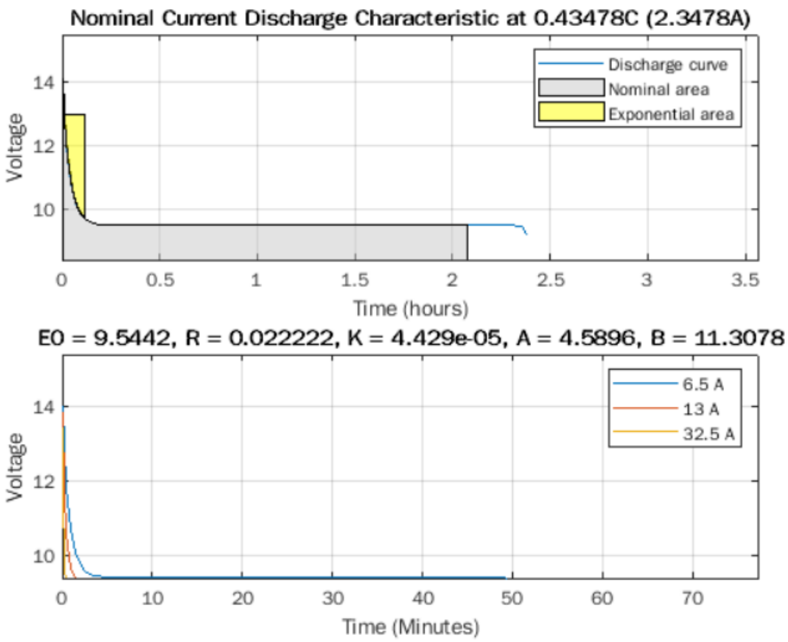

Figure 23: Discharge Characteristics curves for the Li-ion battery model used in the DCMG model

4.6 Buck converter

4.6.1 Common operating principles

DC Microgrids incorporate several DC-DC converters at the power supply and the load sides. They are predominantly used for their low weight, small size, and high efficiency [45].

DC-DC Buck converters are used to step down the input DC voltages according to the household DC load demands. A capacitor is connected in parallel to the load terminal to form a low pass output LC filter, to smooth the voltage to the load by removing the ripples [46]. At steady state, DC or the average input to the LC filter incorporated with an inductor L, has zero attenuation which means that the average output voltage, V_o is equal to the switching cycle average, V_{avg}. Hence, by controlling the duty cycle D, the output voltage can be controlled according to equation 4.8:

$$V_o = V_{avg} = D \times V_{in} \qquad (0 \leq V_o \leq V_{in}) \qquad (4.8)$$

where Vin = input voltage.

For the switching operation, the bidirectional nature is realised using a diode and a transistor. When the transistor gate is on, it carries the inductor current and the diode turns reverse biased, as can be seen in Figure 23.

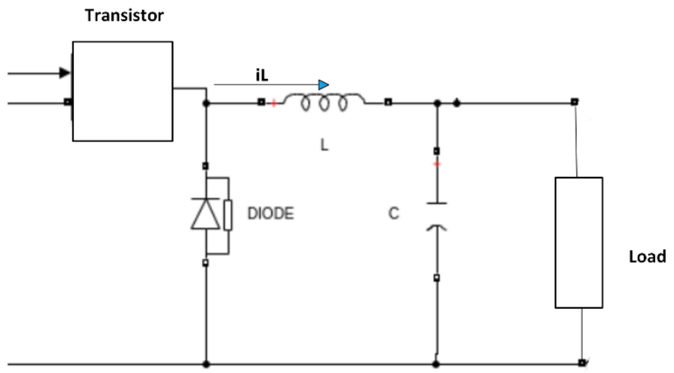

Figure 24: Buck converter switching operation: Transistor Switching ON

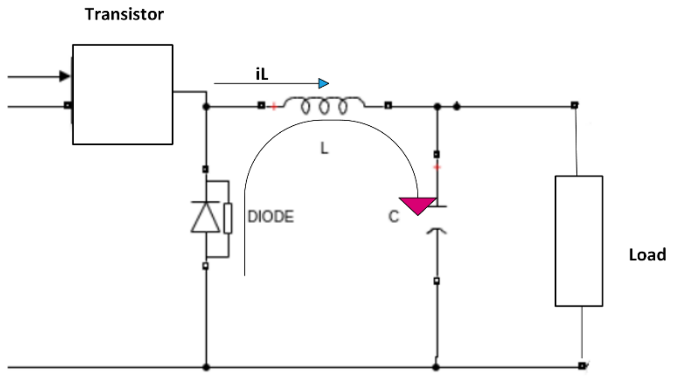

Figure 25: Buck converter switching operation: Transistor Switching OFF

When the transistor is turned off, the inductor current "freewheels" into the diode until the next switching cycle when the transistor is switched on, as can be seen in Figure 24 (above). In the switch mode circuit, the higher the switching frequency, the higher the switching losses in the bi-positional switch. Conversely, the high switching frequencies lead to smaller values components of the LC filter [12]. Therefore, keeping these trade-offs in mind, sensible switching frequencies were selected for the Buck converters, as well as considering the commercial availability of these converters [47]. The following sections discuss the working principles, component sections and design trade-offs of the buck converter.

4.6.2 Topology Selection

The design process for the power converters began with creating a basic buck converter. To model the noise coupling from the parasitic capacitance, C_p, in the Buck converter [47], a capacitor of 0.2nF was added to its circuit as shown in Figure 25 below.

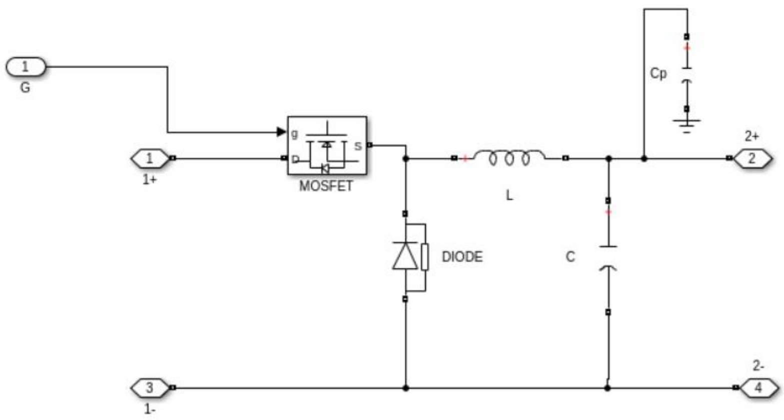

Figure 26: Simulink model of the DC-DC Buck Converter topology

Since high switching frequencies in the range of 100–105kHz were selected, MOSFETs were selected as the switching device, due to their high speed and their inherent ability to handle high switching frequency operations [48]. In practice, n-channel MOSFETs are preferred over the p-channel MOSFETs due to the poor characteristics of the p-channel MOSFETs [12].

The Simulink MOSFET parameters are given in Table 4 below. The RC snubber components are commonly used in the MOSFETs to reduce the high frequency EMI generation.

Table 4: Simulink MOSFET model specifications

Parameter	Value
FET Resistance (R_{ON})	0.1Ω
Internal Diode Inductance (L_{ON})	0H
Internal Diode Resistance (R_D)	0.01Ω
Internal diode forward Voltage (V_f)	0V
Initial Current	0A
Snubber Resistance (R_S)	10^5Ω
Snubber Capacitance (C_S)	infinity

The above frequency range was selected for the DC-DC converter designs, keeping in mind the commercial buck convertor specifications [49].

During the designing of the Buck converters, a problem was encountered. It was found that the Buck converter 1 (326V/48V), could not operate at switching frequencies greater than 10kHz. Designing its components above 10kHz started to affect the output voltages of the remaining converters. Several other switching frequency combinations were tried however, none worked other than within the one in the frequency range of 1kHZ – 10kHz. Hence it was decided to design the Buck converter 1 to switch at 10kHz.

4.6.2.1 Switching Frequency F_{SW}

In any SMPS device, the switching frequency is an important design parameter to consider. It is intuitively known that increasing the F_{SW}, would reduce the Buck converter component values, thereby reducing its overall size. However, this is valid only up to a certain value, i.e., up to a few hundred kHz [12]. Beyond this range, internal inductance within capacitors, and magnetic losses in inductors, would negate the reduced size trend.

Also, the disadvantage of increasing the F_{SW} means that the switching losses in the MOSFET and the diode of the Buck converter would also increase.

In addition to this, higher F_{SW} is a major contributor to EMI due to the higher di/dt and dv/dt which cause switching noise in the control loop and the remaining system. Therefore, these trade-offs were carefully considered during the designing and the component selection processes. Switching frequencies in the range of 100–105kHz were selected to mitigate the EMI issues which may have been caused due to selecting very high switching frequencies for the DC-DC converters in the DC MG model. The Sequence block was used to set the switching frequencies of the converters in the Simulink model.

4.6.2.2 Regulating the DC-DC Buck converter using PWM technique

The average output voltage of the Simulink model of the Buck converters were controlled by the Pulse Width Modulating (PWM) duty ratio d(t) through the MOSFETs. In Figures 26a and b, it can be seen that the output voltage is measured and compared by a PWM controller. The error found is amplified by an amplifier, whose output voltage equals the control voltage $v_c(t)$. As is evident in Figure 26b, inside the PWM controller, the control voltage gets compared with a ramp signal $v_r(t)$, where the comparator output is the switching function q(t), whose pulse width d(t) is modulated to control the buck converter's output voltage.

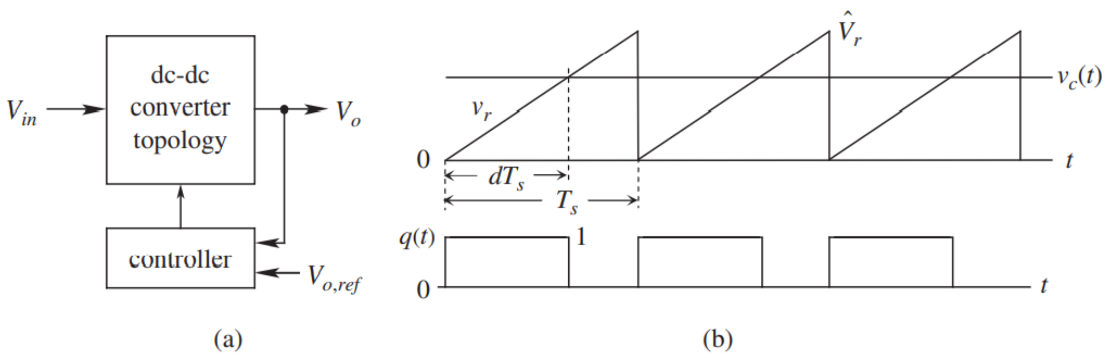

Figure 27: Regulation of output voltage by PWM in a DC-DC Converter [7]

The switching frequency F_{SW} is constant and amplitude of the ramp signal v_r is denoted by V_r. The MOSFET switching function q(t) is the output voltage of this comparator, which is equal to one, if $V_c(t) \geq v_r$, or else it is equal to zero.

The switching duty ratio in figure 26b is denoted by

$$d(t) = \frac{v_c(t)}{V_r} \tag{4.9}$$

Therefore, the control voltage lies between 0 and V_r range for each DC-DC converter, was linear, and controlled the pulse width d(t) dynamically.

4.6.2.3 Buck converter design equations & parameter tables

Figure 27 below shows the basic buck converter model used in the DC Microgrid model.

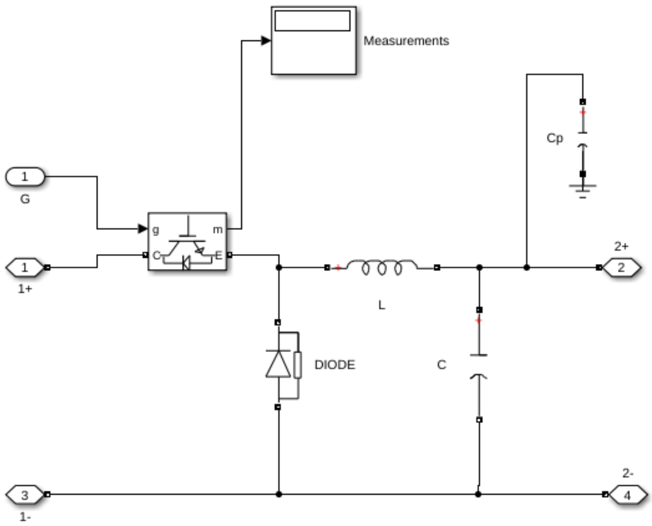

Figure 28: Simulink model of the DC-DC buck converter

1. The first design step was to determine the input and output voltages of the buck converter and its estimated efficiency, ή = 90%. A 90% efficiency factor was used in the equation 4.10 (below) to take the heat dissipated by the converter into consideration [50][51]

$$Maximum\ Duty\ Cycle\ D = \frac{V_{out}}{V_{IN(max)} \times ή} \qquad (4.10)$$

Where $V_{IN(max)}$ is the maximum input voltage and V_{OUT} is the output voltage.

2. To calculate the maximum switch current, the inductor ripple current was calculated by equation 4.11:

$$\Delta I_L = \frac{(V_{IN(max)} - V_{OUT}) \times D}{F_{SW} \times L} \qquad (4.11)$$

Maximum switch current I_{SW}, is also an important parameter to consider in the design and is given by equation 4.12:

$$I_{SW(max)} = \frac{\Delta I_L}{2} + I_{OUT(max)} \qquad (4.12)$$

3. The datasheets [49] were used to determine the recommended inductor value range for the buck converter design. The inductor value is directly proportional to the output current value and the inductor size.

4. The inductor should have a higher current rating than the maximum current provided in equation 4.12. This is due to current increasing with the decreasing inductance.

   Inductance can be calculated using equation 4.13 below:

$$L = \frac{V_{OUT} \times (V_{IN} - V_{OUT})}{\Delta I_L \times F_{sw} \times V_{IN}} \qquad (4.13)$$

5. Diode specification: the built-in Simulink model of the diode was used. It was simulated by a resistor, inductor, and a DC voltage source with a switch in series connection, as shown in Figure 28. The diode voltage, V and current, I controlled the operation of the switch.

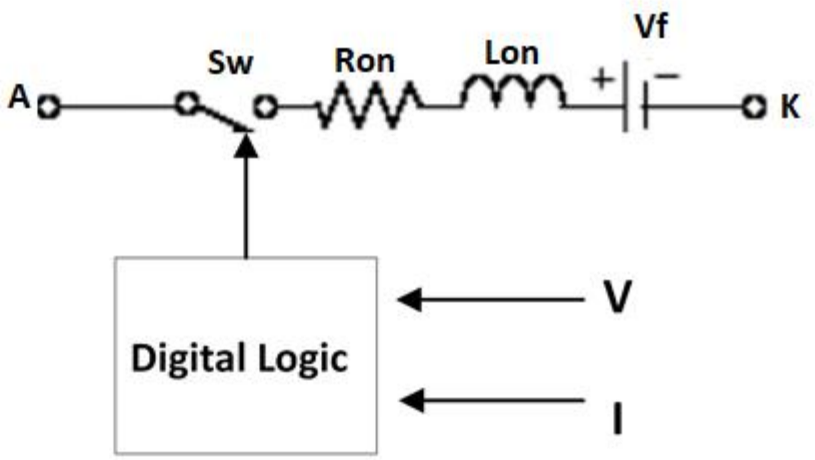

Figure 29: Diode block diagram

Table 5 shows the diode design parameters

Table 5: Specifications of the Simulink model of the Diode

Parameters	Values
Resistance R_{ON}	0.001Ω
Inductance L_{ON}	0H
Forward Voltage V_f	0.8V
Initial Current	0
Snubber Resistance R_S	500 Ω
Snubber Capacitance C_S	250 x 10^{-9}F

6. The buck converter capacitance was calculated using equation 4.14 below:

$$C = \frac{\Delta I_{OUT}{}^{2} \times L}{2 \times V_{OUT} \times V_{OS}} \quad (4.14)$$

Where V_{OS} is the desired output voltage change due to the voltage overshoot.

Thus, each Buck converter was designed, connected to its respective DC voltage buses and its output voltages were measured at each stage, to ensure all the scope readings matched the calculated values.

The following Tables 6 and 7 display the design parameters for all the converters used in the preliminary and final DC Microgrid models. The design process started with creating the Buck converter circuits with a very low switching frequency of 1kHz. Eventually, the switching frequencies were incremented sufficiently to produce realistic final Buck converter models with high switching frequencies as is demonstrated by Table 7 (below).

Table 6: Design Specification of the Buck Converters for Preliminary DC MG Model

Preliminary Design	**Buck Converter 1**	**Buck Converter 2**	**Buck Converter 3**	**Buck – Boost Converter**
Input Voltage(V)	326	48	24	48
Output Voltage(V)	48	24	12	12
Duty Cycle	0.155	0.526	0.526	#
Inductor(mH)	12.56	9.1139	13.333	#
Capacitor(μF)	289.37	137.153	93.7499	#
Switching Frequencies (Hz)	1000	1000	1000	1000

Table 7: Design Specification of the Buck Converters for Final DC MG Model

Final Design	**Buck Converter 1**	**Buck Converter 2**	**Buck Converter 3**	**Buck – Boost Converter**
Input Voltage(V)	326	48	24	48
Output Voltage(V)	48	24	12	12
Duty Cycle	0.155	0.526	0.526	#
Inductor(mH)	12.56	9.1139	13.333	#
Capacitor(μF)	289	137.153	93.7499	#
Switching Frequencies (Hz)	10000	103000	100000	103000

 # Values are specified in table 8.

It was noted during the design process that increasing the preliminary model (Figure 25) Buck converters' switching frequencies to match that of the commercial ones, started to affect the simulated output voltage values. Therefore, several iterations of various switching frequency combinations were used in the buck converters before an optimised combinations of switching frequencies were achieved for all the buck converters, as shown in Table 7 (above).

4.6.2.4 Buck – Boost Converter design

A bi-directional Buck-Boost converter model (48V/12V) was designed to charge and discharge the 12V battery model discussed in section 3.5. Its design parameters have been listed in Tables 6 and 7. This converter was incorporated with a PID controller which is discussed in detail in the next section. The converter works in the buck and boost mode, as the system requires. When the battery voltage is lower than the set point, the converter operates in buck mode (48V/12V). When the battery voltage is higher than the set point, the boost mode (12V/48V) activates, and the battery starts to discharge. This bidirectional power transfer enables an efficient power management of the DC Microgrid [53]. It would also help in regulating the DC bus voltage directly, in contrast to having to use some optimisation-based method for energy management [53].

A design issue was encountered when creating and interfacing the standalone model of the Buck-Boost converter with the battery. The output voltage measurement of the discharge mode of the battery was incorrect. However, this error was eliminated when the model was connected to the PID block which ensured that the correct voltage measurement of the discharge mode of the battery was displayed. Figure 29 shows the circuit diagram of the Buck-Boost converter used in the DC Microgrid model to charge and discharge the 12V battery. Table 8 specifies the design parameters of the Buck-Boost converter used in the design.

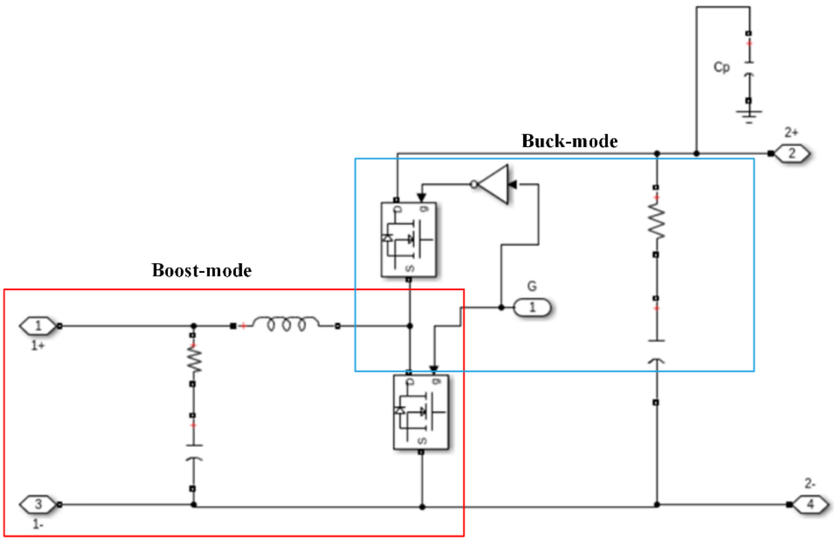

Figure 30: The Simulink model of the Buck-Boost Converter Circuit diagram in the DC MG model

The design equations of the buck-boost converter [54] are as follows:

1. The first design step was to determine the input and output voltages of the buck-boost converter and its estimated efficiency, ή = 95%. 95% efficiency factor was used in equation 4.15 below to take the heat dissipation by the converter into consideration [55]

$$Maximum\ Duty\ Cycle\ D = \frac{V_{out}}{V_{IN(max)} \times ή} \qquad (4.15)$$

Where $V_{IN(max)}$ is the maximum input voltage and V_{OUT} is the output voltage.

2. To calculate the maximum switch current, the inductor ripple current was calculated by equation 4.16:

$$\Delta I_L = \frac{(V_{IN(max)} - V_{OUT}) \times D}{F_{sw} \times L} \qquad (4.16)$$

Maximum switch current I_{SW}, is also an important parameter to consider in the design and is given by equation 4.17:

$$I_{SW(max)} = \frac{\Delta I_L}{2} + I_{OUT(max)} \qquad (4.17)$$

3. The datasheets [46] were used to determine the recommended inductor values range for the Buck-Boost converter design. The inductor value is directly proportional to the output current value and the inductor size.

4. The inductors should have a higher current rating than the maximum current provided in equation 4.17. This is due to current increasing with the decreasing inductance.

Inductance can be calculated using equation 4.18 below:

$$L = \frac{V_{OUT} \times (V_{IN} - V_{OUT})}{\Delta I_L \times F_{sw} \times V_{IN}} \qquad (4.18)$$

5. Diode specification: the built-in Simulink model of the diode was used. It was simulated by a resistor, inductor, and a DC voltage source with a switch in series connection, as shown in Figure 28 (above). The diode voltage, V and current, I controlled the operation of the switch. Table 5 gives the diode design parameters.

6. The buck-boost converter capacitances were calculated using equation 4.19 below:

$$C = \frac{\Delta I_{OUT}{}^{2} \times L}{2 \times V_{OUT} \times V_{OS}} \quad (4.19)$$

Where V_{OS} is the desired output voltage change due to the voltage overshoot

Table 8: Design Specification of the Buck-Boost Converters for Final DC MG Model

Design parameters	Buck mode	Boost mode
Input Voltage(V)	48	12
Output Voltage(V)	12	48
Duty Cycle	0.2631	0.7825
Inductor(mH)	16.667	4.1667
Capacitor(μF)	168.75	352.132

4.6.2.5 Feedback Controller design of the DC-DC Buck Converters – PI & PID Voltage-mode control

The purpose of a feedback controller is to regulate the output voltage of a power converter. The following factors are taken into consideration when designing such controllers:

- Rapid response to changes in input and output voltages
- Zero steady state errors
- Low voltage overshoot
- Low noise susceptibility.

In a regulated DC-DC converter, the feedback controller changes the duty cycle so as to regulate the output voltage [53].

Thus, there are two basic feedback controllers, namely Proportional Integrator (PI) and Proportional Integrator Derivative (PID) controllers, both widely used in the industry.

First, the PI controller used in the Buck converter design would be discussed. One of the most important objectives of this controller is to keep output voltage of the converter, constant, regardless of the disturbances or load variations that may occur in the system. The PI controller’s input is the error signal between the reference voltage and the actual output voltage of the Buck converter. This error should be zero so as to regulate the output voltage to a reference value. Therefore, the equation of the PI controller is given by equation 4.20:

$$C(s) = K_p + \frac{K_i}{s} = K_p \frac{s+a}{s}, a = \frac{K_i}{K_p} \qquad (4.20)$$

Where K_p is proportional gain and K_i is integral gain.

The transfer function of a buck converter is given by equation 4.21:

$$T.F. = \frac{V_0}{V_i} = \frac{\frac{R}{sRC+1} \times I(s)}{\frac{s^2RLC+sL+R}{sRC+1} \times I(s)} = \frac{R}{s^2RLC+sL+R} \qquad (4.21)$$

Where V_0 = output voltage of buck converter, V_i = input bus voltage. For each converter, the transfer equation remains the same, except when its R, L and C values are substituted into the equations. Figure 30 shows the red outlined PI controller in the Simulink model:

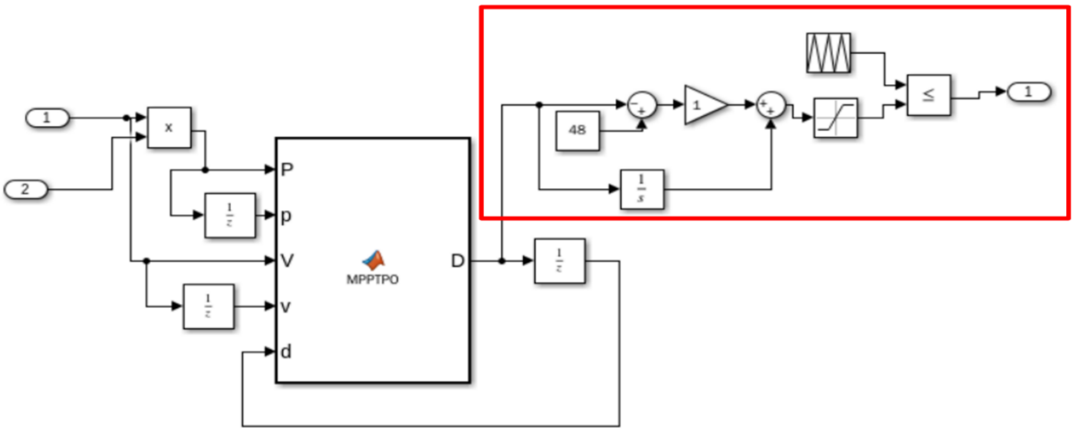

Figure 31: Simulink model of the PI controller used in the DC MG model

Similarly, a PID controller attempts to correct the error between a reference or set value and a measured value by calculating a corrective output action which would adjust the system, accordingly. The transfer function of a PID controller is given by equation 4.22 below:

$$T.F._{PID\ controller} = K_p + \frac{K_i}{s} + K_d s = \frac{K_d s^2 + K_p s + K_i}{s} \qquad (4.22)$$

Where K_p is Proportional gain, K_i is Integral gain and K_d is Derivative gain.

Three control strategies are employed by the PID controller to fulfil its function: Proportional (P), integral (I) and Derivative (D) controls. A PID controller can offer error minimisation to an acceptable level with acceptable levels of stability and damping. The built-in Simulink PID controller models were used in the simulation. Figure 31 below shows the PID model in Simulink.

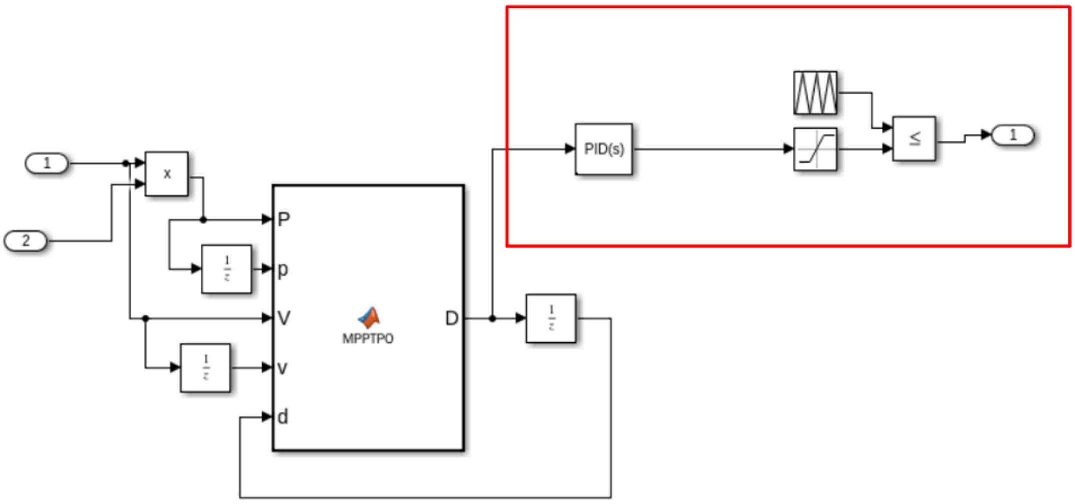

Figure 32: Simulink model of the PID controller of the DCMG model

In applications, where speed of response is not a major requirement, A PI controller is preferred over the PID controller. However, a PI controller would not be able to predict how the error would behave in near future. This shortcoming is mitigated by introducing the Derivative into the PI controller. Derivative control would increase stability by minimising the chances of overshoot.

A stability analysis of the PI and PID controllers for each converter was performed to verify that the PID controllers were more suitable for application in this model.

The MATLAB codes given in Appendix A, were used to determine the stability of the PI versus the PID controllers used in the power converter models.

The Bode plot response was generated to determine the stability of both the controllers using the MATLAB codes in Appendix B.

As explained previously, these codes were customised for each power converter of the DC MG model.

The simulation outputs of these stability analyses are discussed in detail in Chapter 5.

Therefore, after a careful analysis and consideration, the above PID control algorithm was used in controlling the power converters of the DC MG model, due to the ability of the PID controllers to work efficiently with the fast-switching converters used in this design.

Table 9 below shows the PI/PID control parameters for each converter used in the DC MG model.

Table 9: Circuit Parameters of the Converters with PI/PID Control Parameters

Circuit Parameters	Buck Converter 1	Buck Converter 2	Buck Converter 3	Buck - Boost Converter
Input Voltage	326	48	24	48
Inductor(mH)	12.56	9.1139	13.333	#
Capacitor(μF)	289	137.153	93.7499	#
Resistor(Ω	7.6	5.76	2.667	#
Setpoint	48	24	12	12
Proportional gain K_P	48	24	12	12
Integral gain K_I	1	1	0.5	1
Differential gain K_D	1	1	0.5	1

 # values are specified in Table 8

Subsequently, the tuning of the PID parameters was performed according to the DC MG system they would be working in. This would be discussed in detail, in section 4.5.

4.7 DC Household load models

The DC loads connected to all the 3 DC buses are shown in table 10, below. The information on the power ratings of the common New Zealand household appliances were sourced from the Consumer New Zealand website [57].

Table 10: DC Microgrid Load specifications

DC bus Load Voltage	Power use (Watts)	Resistance(Ω)	Typical household appliance based on wattage
48V	300	7.6	cake mixer food processor fan sewing machine
24V	100	5.76	radio stereo
12V	50	2.88	xtraction fan
	4	36	dimmable LED light

4.8 EMI filter designs

EMI generation is a serious cause of concern in the DC MG system. EMI can cause equipment malfunction and eventually lead to serious operational failure, if left unmonitored and unsuppressed.

Slowing down the dv/dt during the converter transitions in the DC MG models, combined with employing an effective EMI filter can help reduce the EMI levels. These filters are made up of coupled inductors. Filter topologies differ from system to system, depending upon load impedances etc. Generally, the differential mode (DM) and Common modem (CM) filters are used to eliminate the EMI emissions. To design an optimised and highly efficient EMI filter, high frequency modelling of the magnetic part of the filter has been utilised. Coupled inductors and capacitors have been modelled and tested for their reliability. Thus, the conducted EMI filter designs were created. For each mode of the conducted EMI, the spectrum analysis graph without the EMI filters was used to calculate the the attenuation level required; this was 41dBV for the differential mode and 7dBV for the common mode EMI. This attenuation level was the difference between the measured disturbance levels and the noise level [58] specified by the EMI standard (refer to Table 1). In order to calculate the above required level of filter attenuations, equation 4.23 [59] below was used:

$$|Att|_{dB} = 20log\left(\frac{\frac{I}{\pi^2 f_s C_{in}} sin(\pi D)}{1\mu V}\right) - V_{max} \qquad (4.23)$$

Where D = duty cycle, I = inductor current, f_s = switching frequency and C_{in} = input capacitor of the converter.

The Nyquist frequency measurement range was 150kHz- 500kHz. Simulations beyond 500kHz produced the Nyquist error message, warning that the start and stop frequency should not exceed the Nyquist frequency limit of [0 – 500]kHz.

A design problem was encounted while determining the filter cut-off frequency. This was because the filter design method stated in [58] could not be directly applied to this design.

Therefore, multiple iterations of different cut-off frequencies were used to design, simulate and test the Spectrum Analyser results against the EMI standards before, an optimised cut-off frequency for both the filters (CM and DM) was achieved. Using this cut-off frequency, the filter components were calculated (refer to Figures 33 and 34 and Table 11).

Figure 32 shows an overview of the circuit diagram of the EMI filters, used in the design.

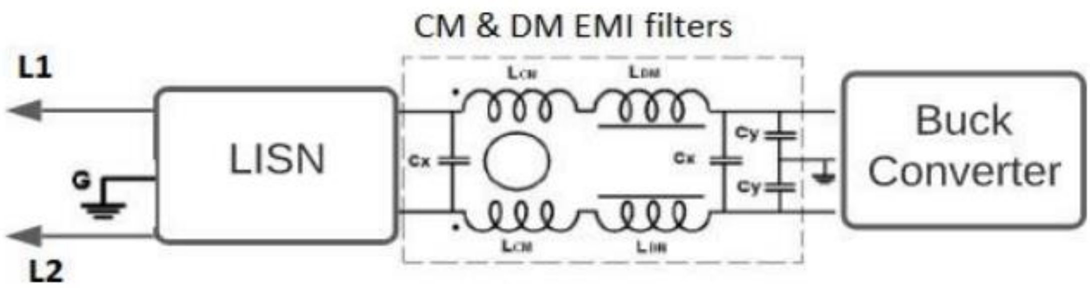

Figure 33: Circuit diagram of the Common-mode and Differential-mode EMI filters

4.8.1 Common mode (CM) EMI filter design

The EMI filters had to be designed according to the mode of conducted EMI it filtered. The Line Impedance Stabilising Network (LISN) circuit does not separate the CM and DM noise signals so separate mode filters had to be designed for this purpose [58]. The CM filter used two capacitors, C_Y, and coupled inductors, L_{CM}, as can be seen in Figure 33. Equation 4.24 is used to calculate the common mode inductor with the chosen value of the capacitor C_Y [58]:

$$L_{CM} = \left(\frac{1}{2\pi f_{CM}}\right)^2 \times \frac{1}{2C_Y} \tag{4.24}$$

Where f_{CM} is the cut off frequency of the CM filter.

Two such CM filters (Figure 33) were used in the design.

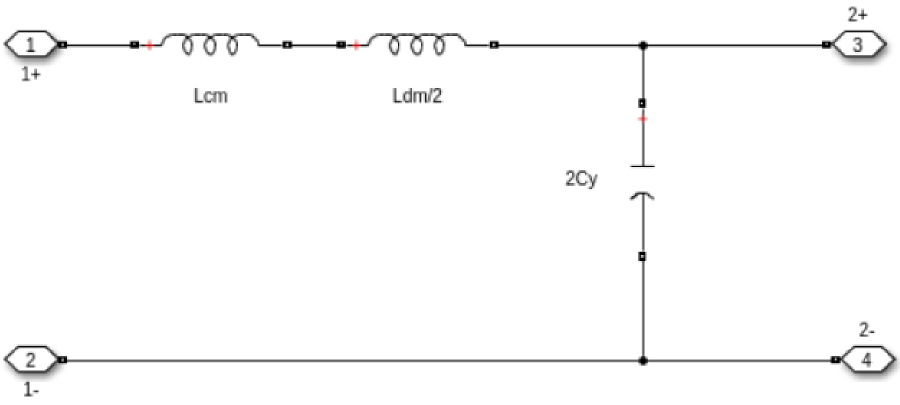

Figure 34: CM filter topology

As stated earlier, the required attenuation for the CM EMI filter, in order to comply with the CISPR allowable limits (refer to fig. 7), was 7dBV.

4.8.2 Differential mode (DM) EMI filter design

The differential mode comprises of two capacitors, C_X, and two separate inductors, L_{DM}. Equation 4.25 is used to calculate the differential mode inductor with the chosen value of the capacitor C_X [58]:

$$L_{DM} = \left(\frac{1}{2\pi f_{DM}}\right)^2 \times \frac{1}{2C_X} \tag{4.25}$$

Figure 34 shows the Simulink model of the DM filter design.

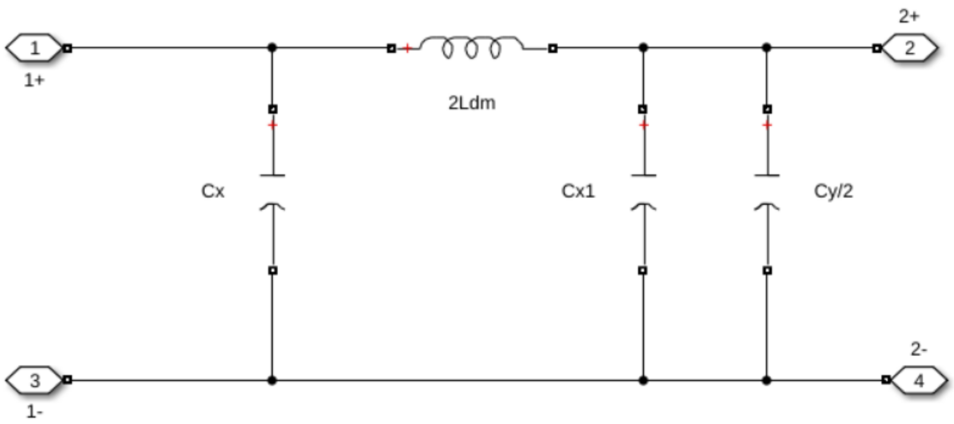

Figure 35: DM filter topology used in the DCMG models

Table 11: CM and DM EMI filter specifications

EMI filter	**Inductor**	**Capacitor**	**Cut-off Frequency**
Common mode	1.68mH	9.4µF	28.32kHz
Differential mode	125µH	1.175nF	592.108Hz

4.9 LISN circuit for measuring the Conducted EMI noise

The Special Line Impedance Stability Network (LISN) was used to measure the conducted noise for the DC – DC converters in the DC MG model. Figure 35 illustrates the schematic diagram of the LISN circuit used in the model and Table 12 displays the circuit parameters.

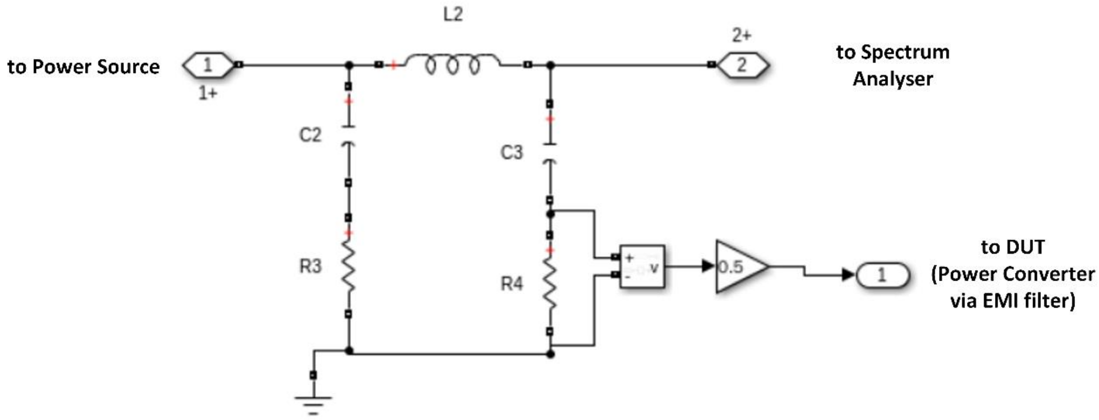

Figure 36: LISN circuit

Table 12: LISN circuit specifications

Parameters	Values
Inductor L_2	5µH
Capacitor C_2	1µF
Capacitor C_2	100nF
Resistor R_3	1Ω
Resistor R_4	50Ω

Figure 36 shows the equivalent Simulink model of the connection between the SPV(power supply), the LISN, EMI filters and the buck converter configuration.

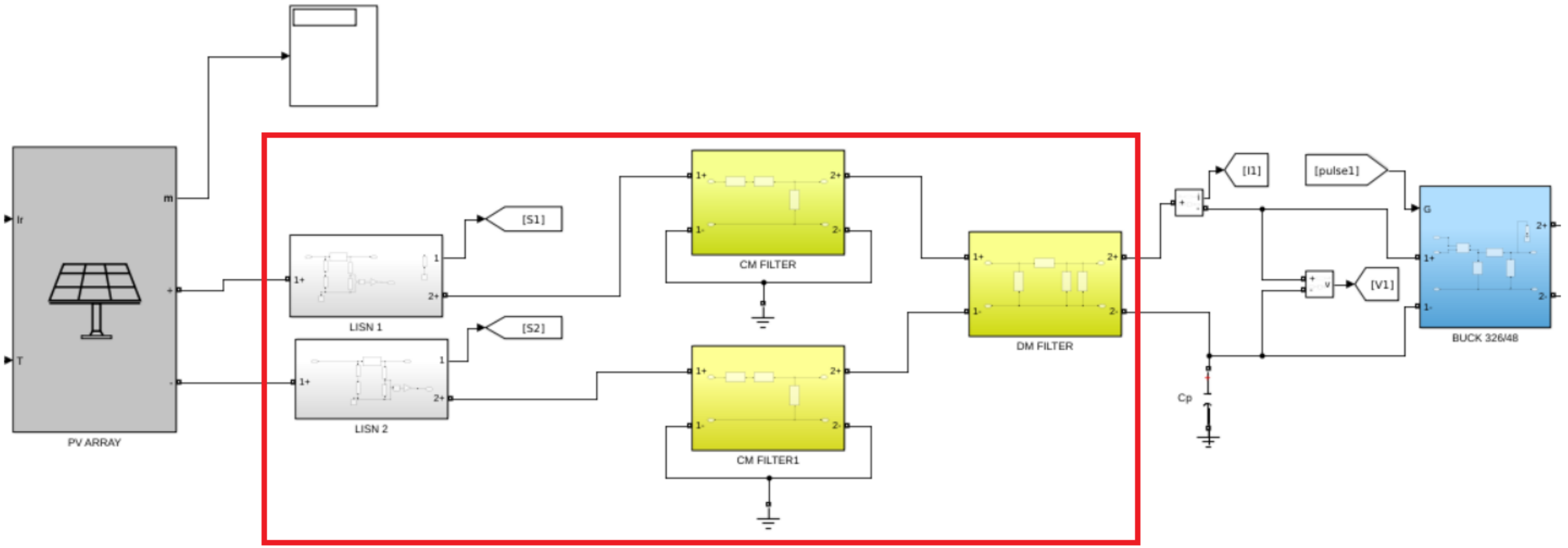

Figure 37: LISN and EMI filter connection shown inside the red block

4.10 Spectrum Analyser

The Simulink block model of a Spectrum Analyser was used to display the EMI emissions in the DC MG model due to the frequent switching properties of the power converters present in the model. The Spectrum Analyser block displayed the frequency spectra of the common mode and differential mode voltage signals. A Simulink model of the Spectrum Analyser is configured to measure the following parameters:

- Signal values through the horizontal and vertical cursors
- Finding the harmonic distortion
- Finding peak value by finding the signal's maximum value and its corresponding x-value. For example, the equation 4.26 [9] below could be used to find the peak voltage signal:

$$V_{peak} = max(V_i) \tag{4.26}$$

Where, for N evenly sampled data in one period, the envelope of the maximum value of the sampled data is V_{peak}.

Figure 37b below, shows how the CM and DM signals have been connected to the spectrum analyser to display the EMI emission in its frequency content. The inherited sampling rate of the block model was 1MHz. Details of the Spectrum Analyser settings are shown in Figure 37a.

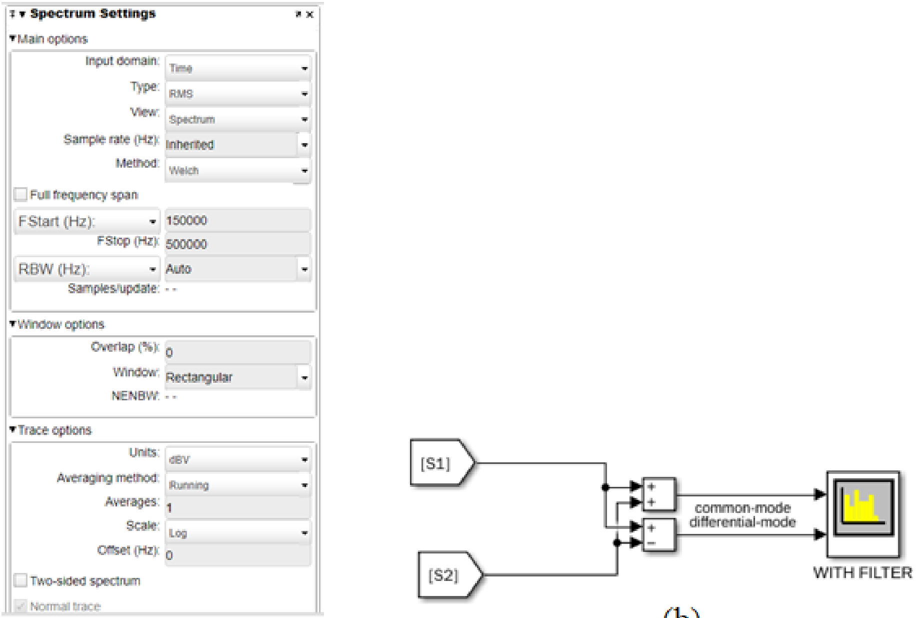

(a)　　　　　　　　　　(b)

Figure 38: (a) Spectral Analysis setting (b) block diagram in Simulink

4.10.1 Welch's algorithm

The Spectrum Analyser block displays the frequency domain of the voltage outputs, the common mode and differential mode, from LISN 1 and LISN 2, simultaneously which will be discussed in detail, in the next chapter. The input signals were transformed into the frequency domain using the Fast Fourier Transform (FFT) internally. The measurement of a range of frequencies is performed sequentially. Figure 37a displays the Spectrum setting used for this analysis.

As can be noted from figure 37a, the Spectrum analyser used the Welch's method for analysis.

This method was selected in MATLAB/Simulink based on it being a widely used nonparametric spectral estimation algorithm [60].

Welch's method is based on non-parametric methods which divide the time domain data into segments by applying the Fourier Transform on each segment, calculating the squared magnitude of the FFT segment, summing, and averaging the transform [61].

4.11 Finalised designs of the DC Microgrid models

The previous sections discussed the DC Microgrid architecture at its component level. In the next section, fully developed architectures would be presented to model real-world and efficient DC MG models which would provide reliable and accurate results to study the aggregated conducted EMI emissions. The add-on features incorporated into the preliminary DC MG model are:

- varying switching frequency of the converters,
- introducing the MPPT technology into the model
- having closed loop feedback systems – PI and PID controllers for converters
- EMI filters connected at different points of interest in the DC MG model.

Chapter 5 **EMI Analysis**

This chapter presents key findings from the simulation outputs of various topologies of the DC Microgrid models to investigate the generation of the electromagnetic interference due to their power converters. Each model was developed from the conceptual designs to fully functional and accurate DC Microgrid models. This process involved extensive research, modelling, trialling, troubleshooting and rectifying design flaws. Performing several iterations of the design parameter tunings, formed a crucial part of the design process in order to develop well-tuned DC Microgrid models for the study.

5.1 Topology 1: DC Microgrid model with Basic power converters

Topology 1(Figure 38) was first modelled using the basic power converters without any control feedback loops.

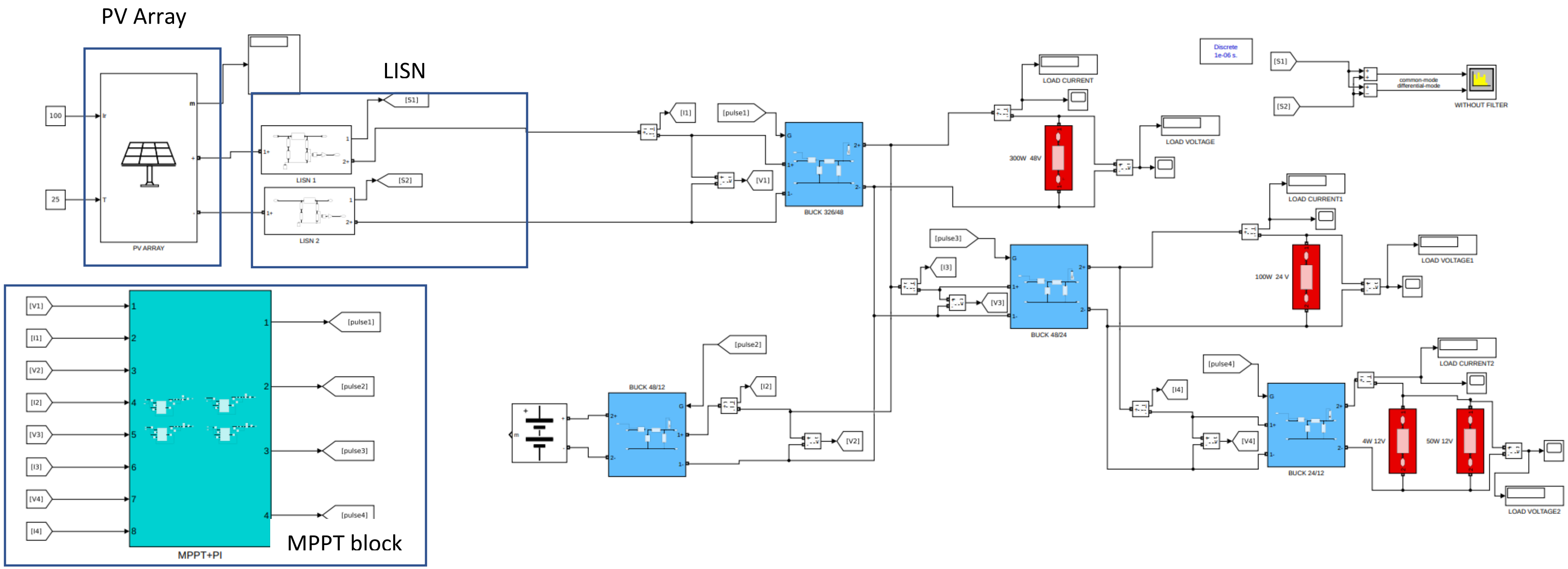

Figure 39: Preliminary model – MATLAB/Simulink model of DC Microgrid without EMI filters

<u>Legend – Colour coding</u>

Cyan = Maximum Power Point Tracking (MPPT) and Proportional Integrator (PI) block

Blue = Buck Converters; Blue block connected to battery is Buck-Boost Convertor

Yellow = Spectrum Analyser; Red = DC Loads

5.1.1 EMI simulation at various frequency ranges

This model did not have any EMI filters and all the power converters operated at same switching frequencies. The purpose was to verify the literature claim that conducted EMI is more prevalent in the frequency range of 150kHz – 30MHz [16]. Therefore, a frequency range of 2kHz – 149kHz [62][63] and 150kHz – 0.5MHz was selected for the EMI simulation for this purpose.

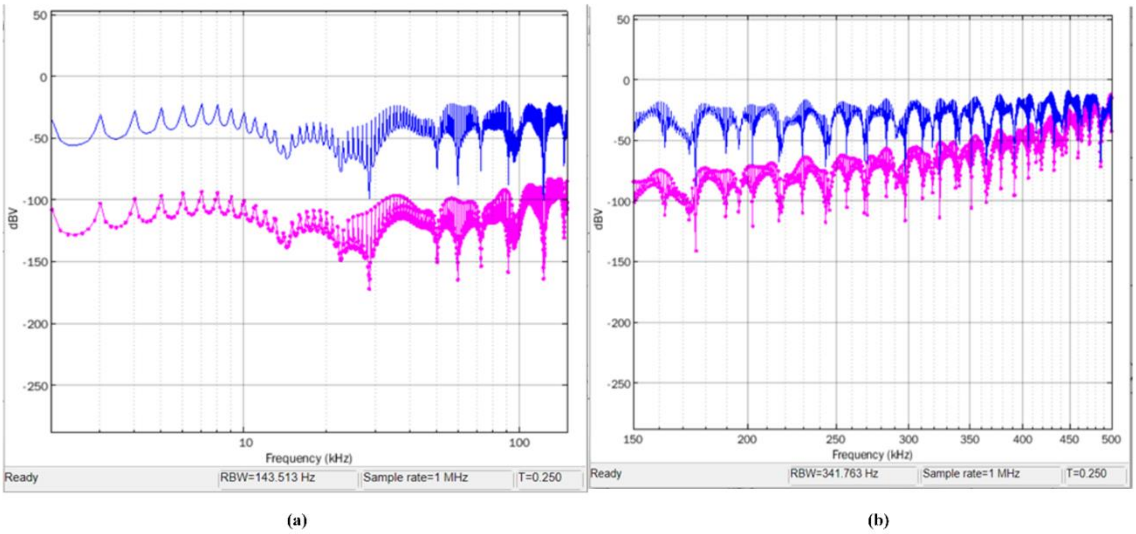

Figure 40: EMI simulation from (a) 2kHz-149kHz, (b) 150kHz-500kHz

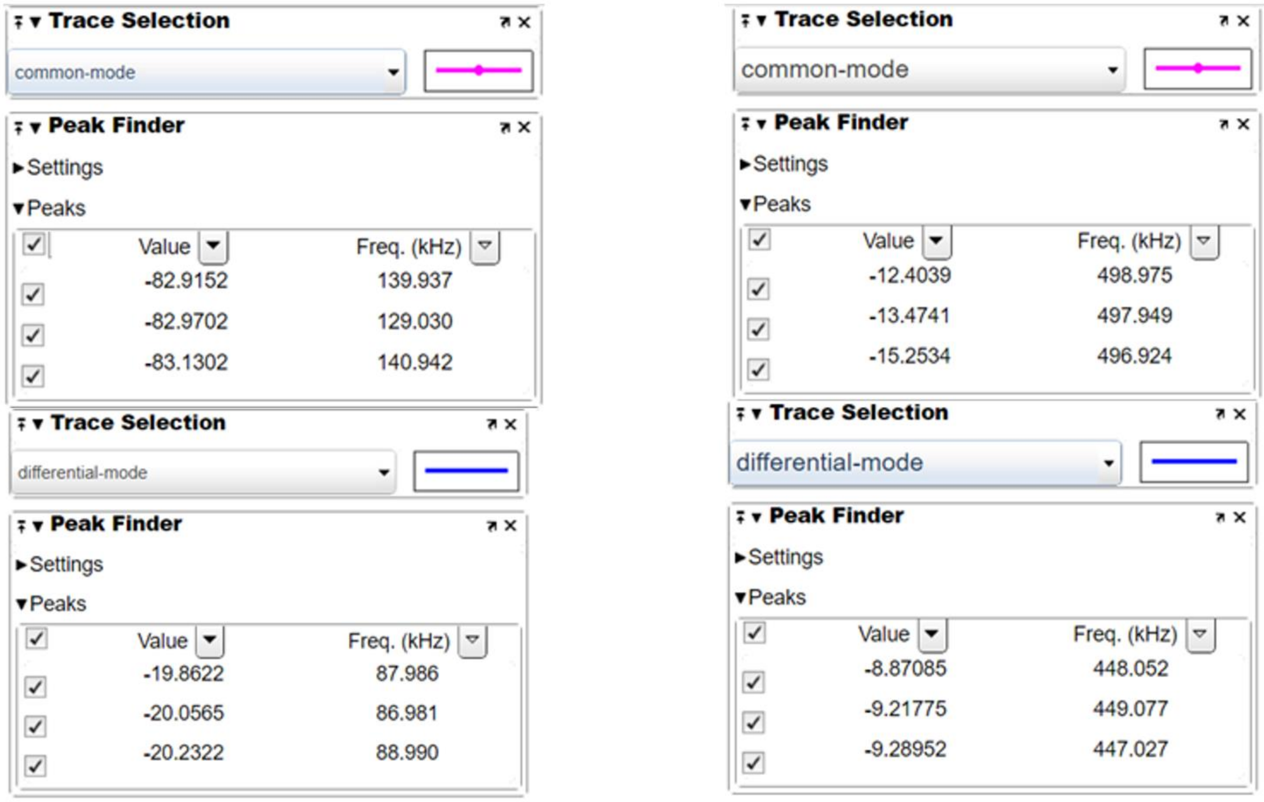

(a) **(b)**

Figure 41: Peak noises of the DC MG model with basic converters at (a) 2kHz - 149kHz (b) 150kHz - 500kHz

5.1.1.1 Measuring the EMI levels

Bascially, the EMI compliance tests are discussed in terms of the three detectors, namely, the quasi peak, peak and the average limits [63][64][65][66][67].

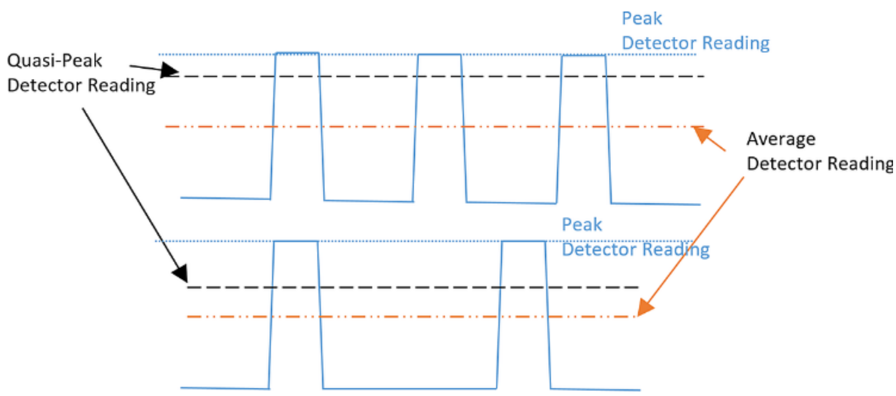

Figure 42: Difference between Quasi-Peak, Peak and Average measurements of EMI [68]

However, in the MATLAB Simulink model of the Spectrum Analyser, as discussed in section 3.1, these measurements can be performed using Peak detections etc. Based on Figure 41, $V_{peak} > V_{quasi-peak} > V_{average}$ [9], it can be confirmed that if a design simulation shows measurements in peak limits, satisfying an EMI compliance standard in the quasi-peak limits such as those outlined in Figure 7 (Section 3.5), with plenty of margin to spare, then the quasi-peak simulation/comparison may not be required. To convert the simulation measurements from dBV to the unit in which the CISPR measurements are presented (in dBμV) in Figure 7, equation 5.1[69] below was used:

$$dB\mu V = dBV + 120 \tag{5.1}$$

Hence, from Figure 39, it can be seen that the EMI peaks for the common-mode noise are mostly around approximately 140kHz and 498kHz. For the differential mode noise, the EMI peaks have been found around approximately 88kHz and 449kHz for both the models described above. Therefore, it was evident from the above figures 39a and 39b that the EMI emissions are more prevalent at frequencies close to 150kHz and beyond.

5.2 Topology 2: Power converters with different switching frequencies: 1 filter model versus 4 filters model

Having ascertained through the simulation results of the topology 1 above, that the EMI emission is more prevalent between the frequency range of 150kHz – 500MHz, the same model was further developed to include the EMI filters and the DC-DC converters were re-designed to operate at different switching frequencies. The purpose of this design modification was to determine if having different switching frequency converters, introducing EMI filters and increasing the number of EMI filters in the DC MG model, had any impact on reducing the EMI emission. Therefore two DC MG models (refer to Figures 42 and 43 below) were designed using the basic power converters having different switching frequencies and without any control feedback loops, similar to topology 1.

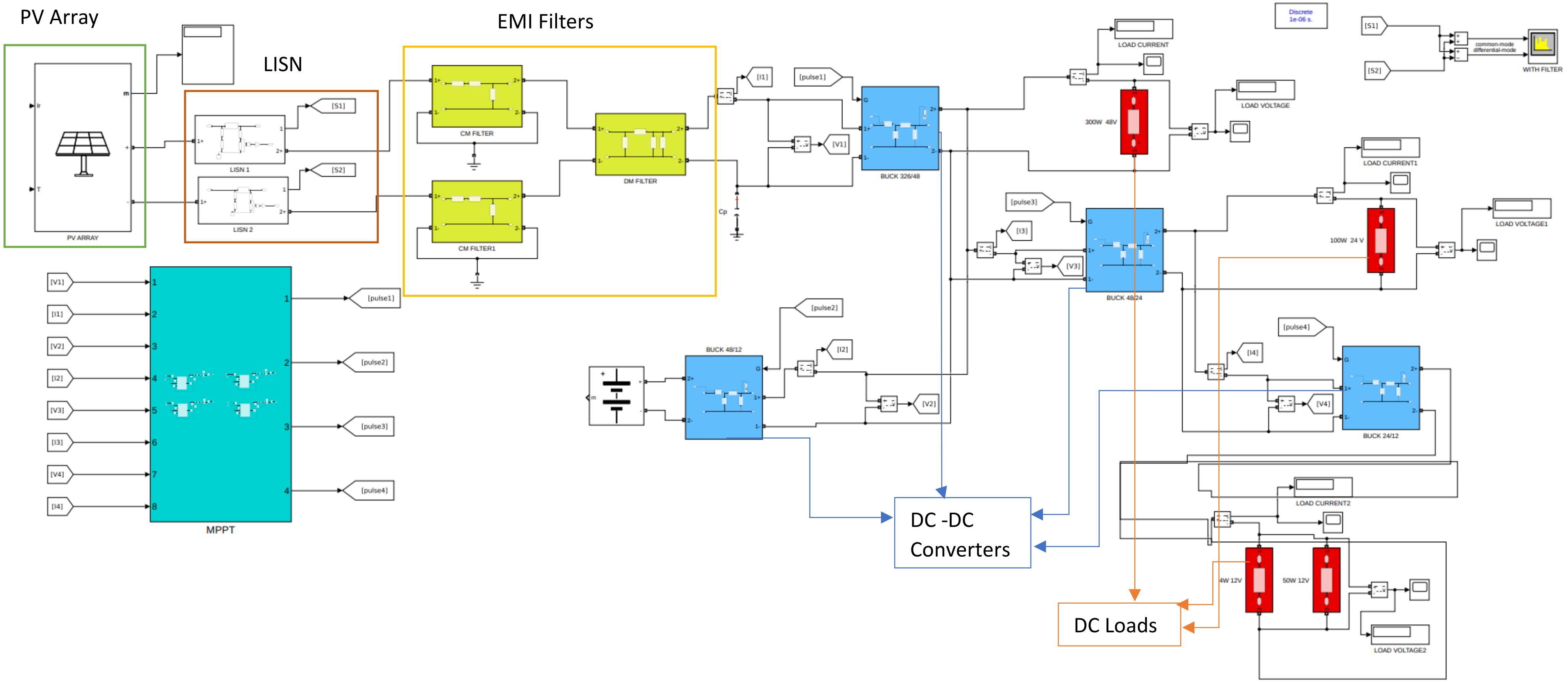

Figure 43: DC Microgrid model with 1 CM & DM EMI filters

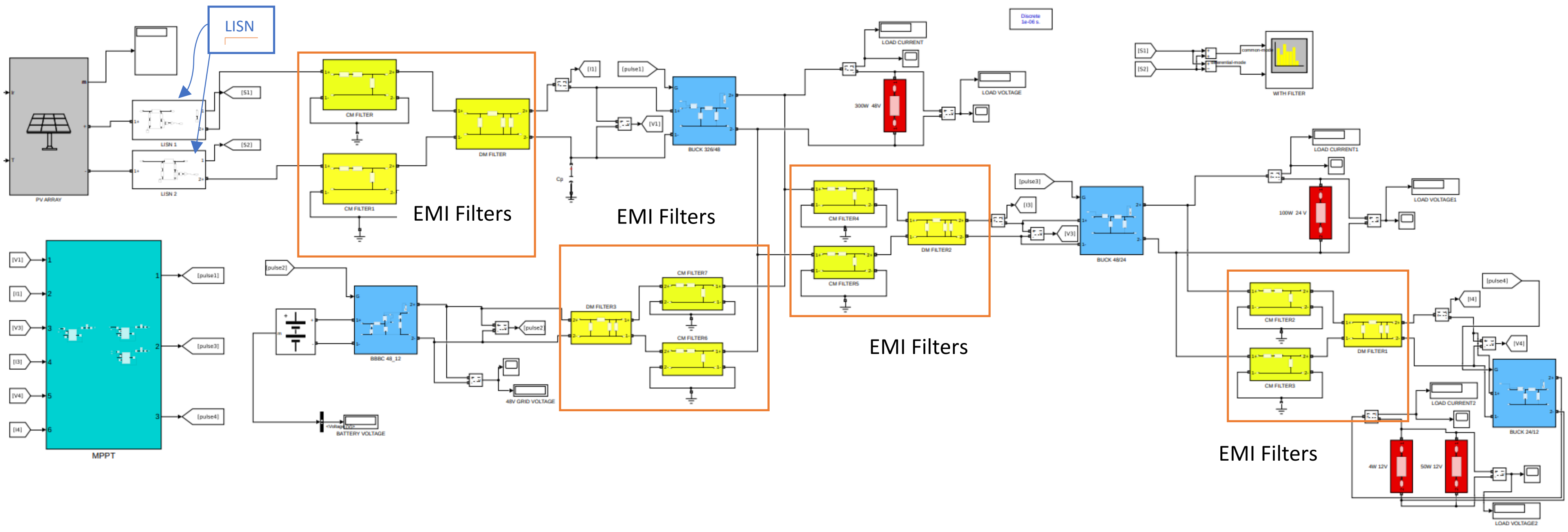

Figure 44: DC MG model with 4 CM & DM filters

Both the models had EMI filters. One model (Figure 42) comprised of one EMI filter set for the common-mode and the differential-mode noises. The other model (Figure 43) had four EMI filters, i.e., each set of CM and DM filters per each power converter present in the DC MG model.

The purpose of modelling and simulating these different topologies was to determine which topology produced the higher EMI reduction.

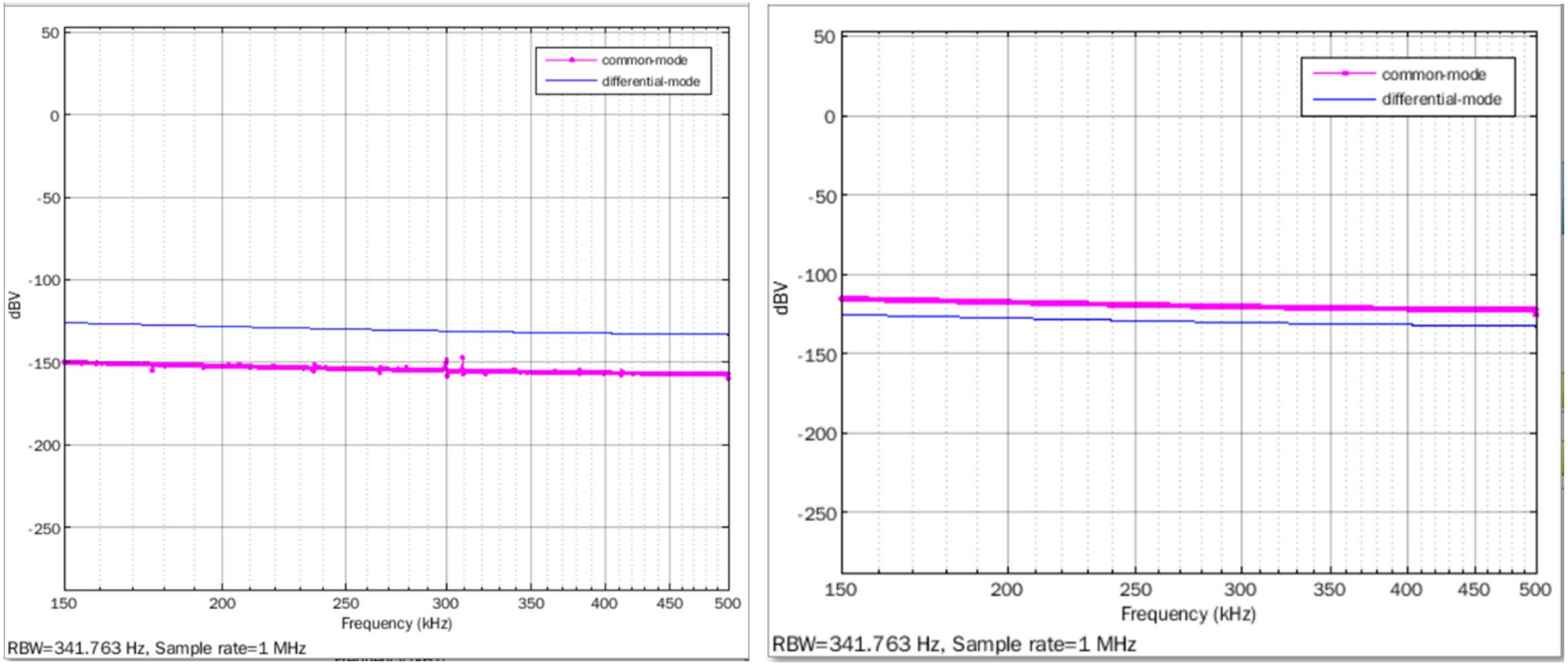

(a) **(b)**

Figure 45: EMI simulation of the DC MG model (a) DC MG model with 1 EMI filter (b) DC MG model with 4 EMI filters

It is evident from Figure 44a and 44b that a single CM and DM filter DC MG model is more effective in reducing the EMI effects contrary to the expectation that a four filter model would be more effective in minimizing the EMI generation. Both DC MG models used same designs for their DC-DC converters and the rest of their microgrid components. The only variation in the designs was the number of CM and DM EMI filters used. Whilst the differential-mode reduction has not been significantly affected by the number of EMI filters used, the common-mode reduction has been significant for the one filter model relative to the four filter model. Therefore, if basic power converters (without control feedback loops) are used in a DC MG model, using a one filter model is more efficient than a four filter model to minimise the common-mode noise generated by the power converters.

5.3 Topology 3: DC Microgrid model with Feedback controlled power converters

5.3.1 PI versus PID controlled power converters

Closed loop stability analysis of converters plays a significant role in the controller selection based on their performances with regards to the EMI reduction. Since the output voltage of converters change with the change in load and supply, it is essential to regulate this voltage using PI/PID controllers. A Proportional (P), Integral (I) and Differential (D) controllers improves the steady state parameters.

Proportional controller determines the reaction of the current error value, while the Integral controller determines the reaction depending on the sum of errors. Derivative controller is calculated using the slope of error over time. The cumulative effect of these controller actions will regulate the DC – DC converter output voltage thus improving the overall stability of the individual converter as well as the microgrid, thereby reducing the overall EMI emissions.

5.3.1.1 One filter model

Topology 3A of the DC MG model, was designed using the PI and the PID controlled power converters.

Topology 3A comprised of the following two different DC MG models:

- One DC MG model had 1 set of EMI filters and PI controlled DC-DC converters
- One DC MG model had 1 set of EMI filters and PID controlled DC-DC converters.

The purpose of designing these models was to determine if having controllers for the power converters assisted in minimising the EMI generation in the DC MG models.

The objective of modelling and simulating these different models was to determine which feedback controller enabled higher EMI reduction.

Figure 45, below demonstrates that no significant difference was noted between the common-mode and differential-mode noises for either of the controllers, for the case of single EMI filter incorporated DC MG models.

5.2.1.2 Four filter model

Topology 3B, comprised of the following two different DC MG models:

- One DC MG model consisted of 4 set of EMI filters and PI controlled DC-DC converters
- One DC MG model consisted of 4 set of EMI filters and PID controlled DC-DC converters.

In figure 45, below, the model having 1 set of EMI filters with PID controlled converters, demonstrated a reduction of the differential-mode EMI by 12.513dBV, whereas no reduction of common-mode EMI was noted.

In Figure 46, below, the model with PID controllers, having 4 EMI filters, showed a common-mode EMI reduction of 1.961dBV and the differential-mode reduction of 1.792dBV.

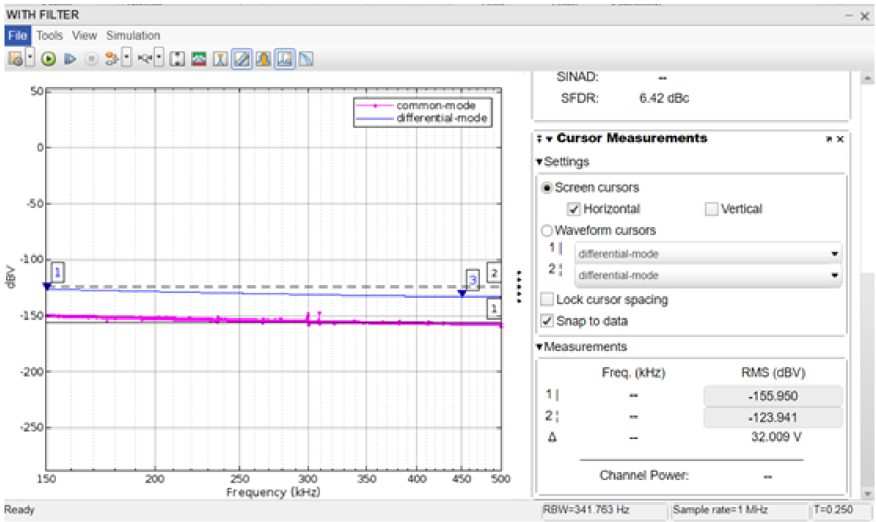

(a)

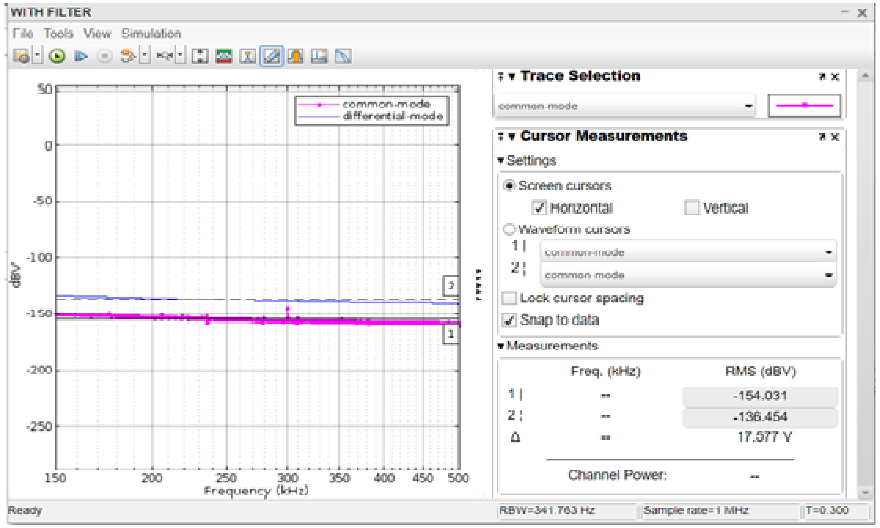

(b)

Figure 46: One filter model with (a) PI controlled power converters (b) PID controlled power converters

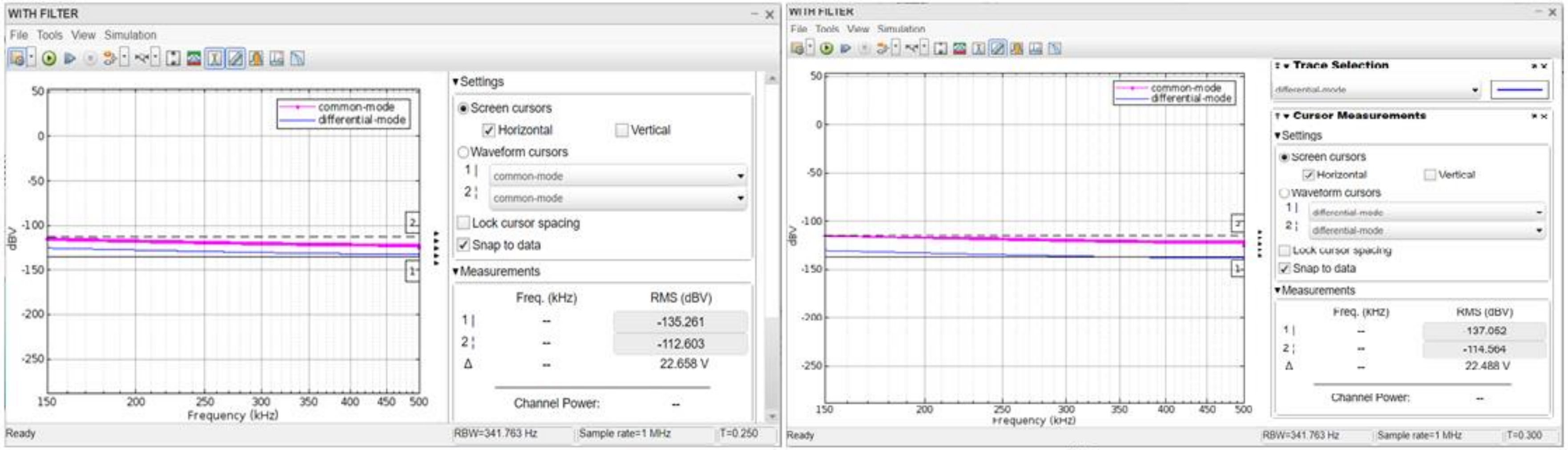

(a) (b)

Figure 47: Four filter model with (a) PI controlled power converters (b) PID controlled power converters

5.4 Summary of performance of the PI/PID controlled converters using single and four EMI filters

PI and PID controlled power converters with single and four EMI filters were considered. The purpose was to determine which controller offered higher EMI reduction and which topology was best suited for this function.

From the simulation outputs(refer figs. 45 and 46), it is evident that the DC MG model having PID controlled converters (topology 3A), performed better that the PI controlled ones.

It was also observed that the one filter PID controlled model had greater CM EMI reduction than the four filter PID controlled model. Overall, the common-mode and differential reduction in the one filter, PID controlled model was greater than the other configurations, thus making it the preffered model for the EMI reduction.

Therefore, it can be concluded that designing a DC MG model with a single set of EMI filters, with the PID controlled converters, is more effective and economical in reducing the EMI generated by each converter in the model, especially in terms of common-mode reduction.

5.1 Stability Analysis of the PI versus PID controlled converters

To explore the possibility of further decreasing the EMI generation in the DC MG model, stable controllers for the power converters were designed and investigated. The objective of this design decision was to ascertain if a stable controller would aid in reducing the overall EMI generation in the DC MG models. The general understanding was that employing the most stable controllers in the DC-DC converters, would help minimise EMI generation. Therefore, bode plots, being an important tool in stability analysis studies, were used to determine the stability of the PI/PID controllers. Hence, this section shows the results of the Bode plot and step response of the PI versus the PID controlled power converters of the DC MG model.

5.1.1 Buck Converter 1

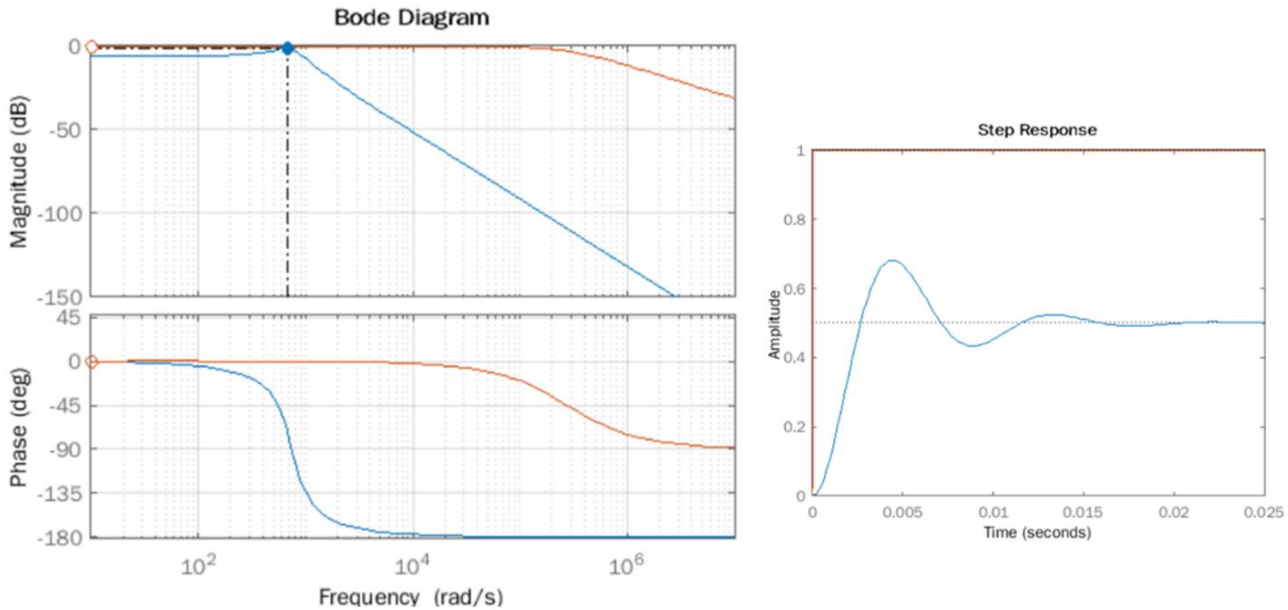

(a) **(b)**

Figure 48: Bode Plot and step response of Buck converter 1

Legend:

Blue trace – Buck converter with PI controller; Orange trace - Buck converter with PID controller

Table 13: Bode plot response characteristic of Buck converter 1

Buck Converter 1	PI controller	PID controller
Rise time (sec)	0.0025	0.824×10^{-5}
Settling time (sec)	0.015	1.48×10^{-5}
Transient time (sec)	0.015	1.48×10^{-5}
Steady state (sec)	0.025	3.5×10^{-5}

where the Rise time is the time required for the reponse to achieve 50% of the final value, settling time is the time required for the response to reach and remain within a specified value of its final value, and the time response is the sum of the transient and steady state time.

5.1.2 Buck Converter 2

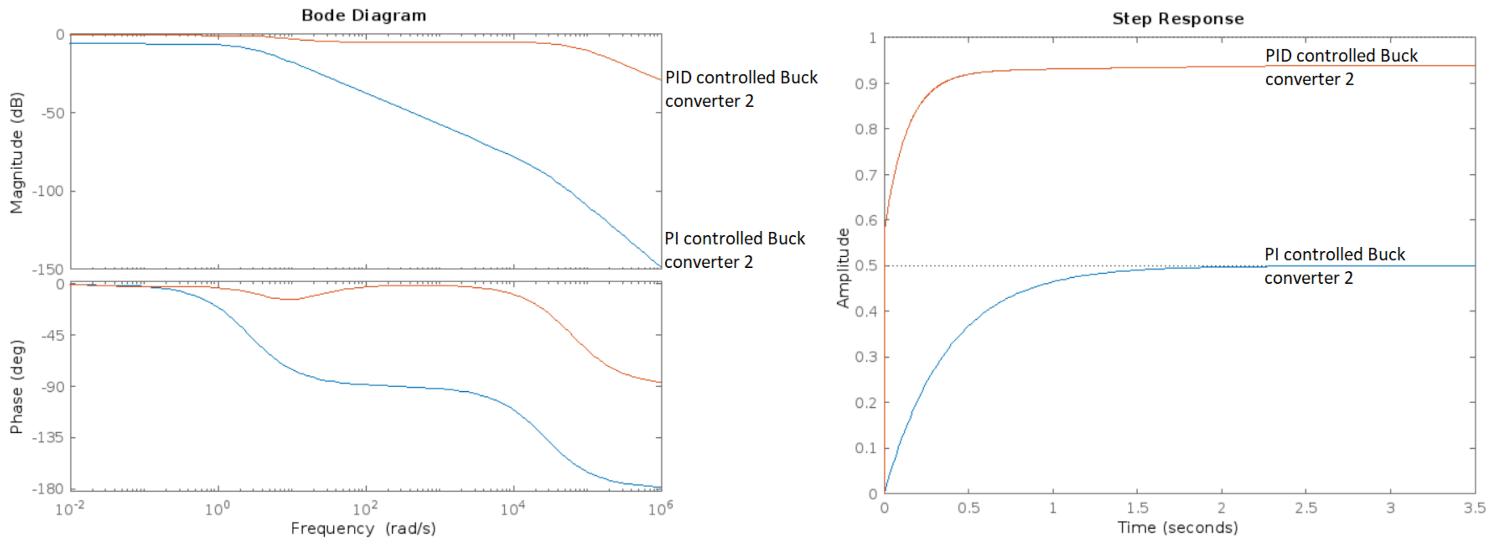

(a) (b)

Figure 49: Bode Plot and step response of Buck converter 2

Table 14: Bode plot response characteristic of Buck converter 2

Buck Converter 2	PI controller	PID controller
Rise time (sec)	0.921	0.381
Settling time (sec)	1.498	-
Transient time (sec)	1.498	-
Steady state (sec)	3.5	1.4

5.1.3 Buck Converter 3

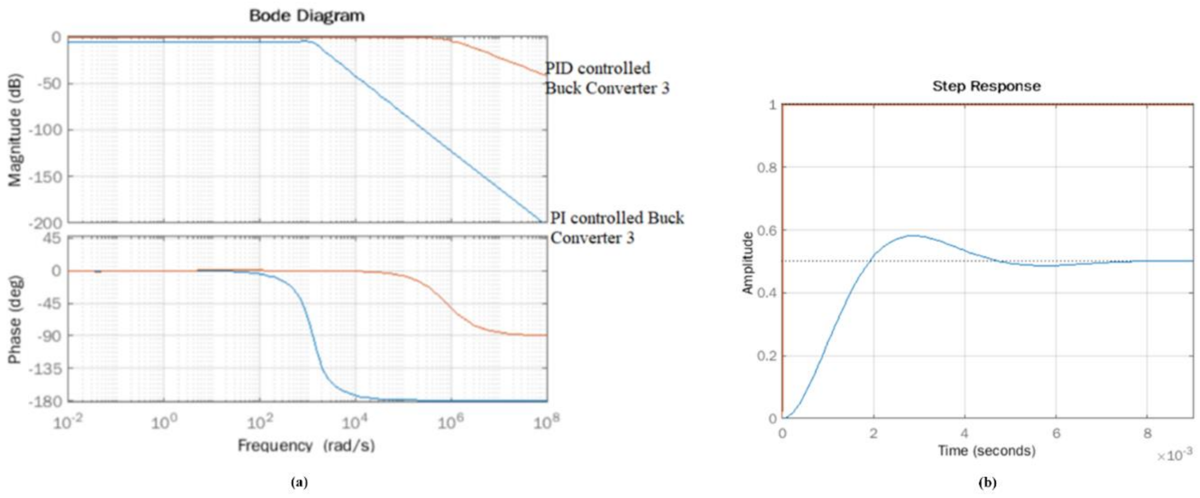

Figure 50: Bode Plot response and step response of Buck converter 3

Table 15: Bode plot response characteristic of Buck converter 3

Buck Converter 3	PI controller	PID controller
Rise time (sec)	1.812×10^{-3}	0.284×10^{-5}
Settling time (sec)	6.311×10^{-3}	0.512×10^{-5}
Transient time (sec)	6.313×10^{-3}	0.512×10^{-5}
Steady state (sec)	7.001×10^{-3}	1.2×10^{-5}

5.1.4 Buck - Boost Converter

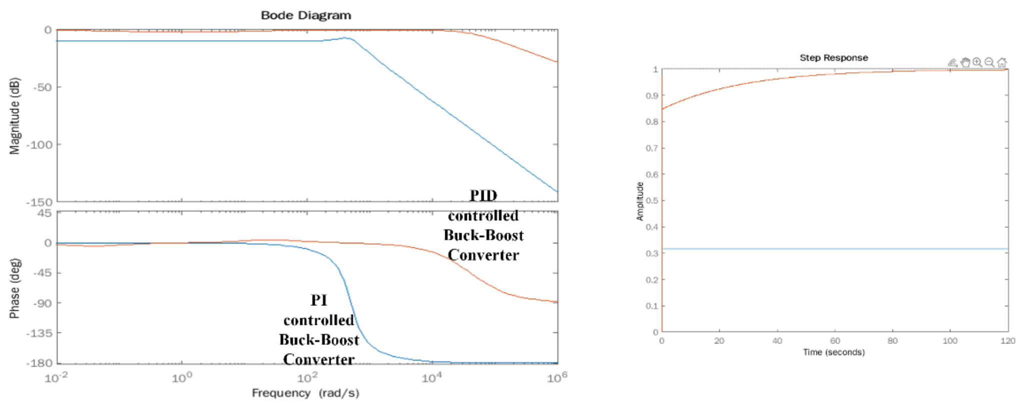

Figure 51: Bode Plot response and step response of Buck-Boost converter

Table 16: Bode plot response characteristic of Buck-Boost converter

Buck-Boost Converter	PI controller	PID controller
Rise time (sec)	0	0.00291
Settling time (sec)	57.5	0.0167
Transient time (sec)	57.5	0.0167
Steady state (sec)	120	0.03

5.1.5 Summary of Stability analysis of the PI and PID controlled converters

The main objective of this study was to determine which type of controller to use in the power converters of the final DC Microgrid models, with the aim of reducing the EMI emissions. Therefore, as part of this research, a stability analysis of the PI versus PID controllers was performed to determine if this had any impact on the overall EMI emission.

The stability analysis study in section 5.5 has proven that the PID controlled power converters have performed better than the PI controlled converters. PID controllers have faster rise times, settling times, transient times and reach steady states quicker than the PI controlled converters.

Therefore, the design decision to continue using one set of the CM and DM EMI filters in the PID controlled DC MG model appeared more feasible, economical, and beneficial in this case. As for the controllers, the PID controller was selected to be incorporated into the DC MG's power converters, due to its superior performance in the stability analysis study, in comparison to the PI controllers.

A design issue was encountered when simulating the Buck-Boost converter model. It was discovered that using the MPPT function for the Buck-Boost converter introduced too many fluctuations in the output voltages at the transient state. Therefore the decision was made to remove the MPPT connections and keep the PID controller connected to the Buck-Boost converter which significantly reduced the output voltage fluctuations. For the remaining Buck converters, this issue did not pose any issue during the simulations.

5.2 Fine-Tuning of the PID parameters: Ziegler and Nichols First Method

Due to the non-linear and time-varying characteristics of the switching operations of the power converters, PID controllers need to be fine tuned for optimal performance in order to obtain the minimum time transient recovery in the DC-DC converters [64]. A fine-tuned controller would help reduce the EMI emissions in the DC Microgrid model occuring due to its power converters. Therefore, as part of the research investigations, PID controllers were optimised by fine-tuning them for each DC-DC converter in the DC MG model, with the aim of lowering the EMI effects in the overall design.

Ziegler and Nichol's (ZN) First Method, based on the step response of the power converters [65], was used for tuning the PID controllers for all the power converters. The main objective of this fine tuning was to stabilise the output voltages for all the power converters used in the DC Microgrid model. The secondary objective was to minimise the control error by only outputting the voltages which were exactly equal to the set voltages of the control feedback loop of the power converters.

The ZN method involves determining the values of the proportional gain K_p, the integral time T_i and the derivative time T_d, based on the transient response characteristics of the power converters. The ZN method suggests setting the values of the K_p, T_i and T_d would produce a stable operation of the converter system. Table 17 below shows the formula for setting the values of the K_p, T_i and T_d.

Table 17: Ziegler and Nichols PID Tuning Rule (First Method)

Type of Controller	K_p	T_i	T_d
PID	$1.2\frac{T}{L}$	2L	0.5L

5.2.1 Fine tuning of the Buck converter 1

The Ziegler and Nichols First Method was implemented using the MATLAB codes found in Appendix C.

A tangent was drawn to the graph (Figure 51) to determine the steady state value K, the lag L, and time constant T. The MATLAB code in Appendix D, was used for designing the K_p, K_i and K_d.

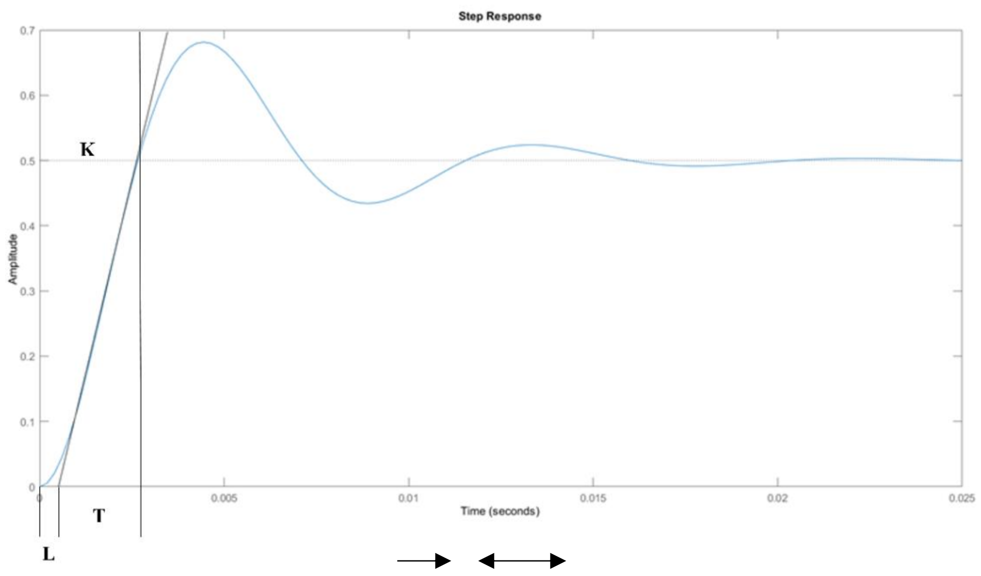

Figure 52: Ziegler-Nichols Rules for tuning PID controllers

Hence, K_p = 13.1, K_i = 1.09 x 10^{-4} and K_d = 0.00394 was obtained from the above simulation results. Figure 52 demonstrates the step response of the Buck converter 1, with and without the tuned PID controller. The orange trace displays the converter step response with the tuned PID controller and the blue trace shows the one without the PID controller. It can be observed from this graph that a tuned PID controller performs better than the system without one.

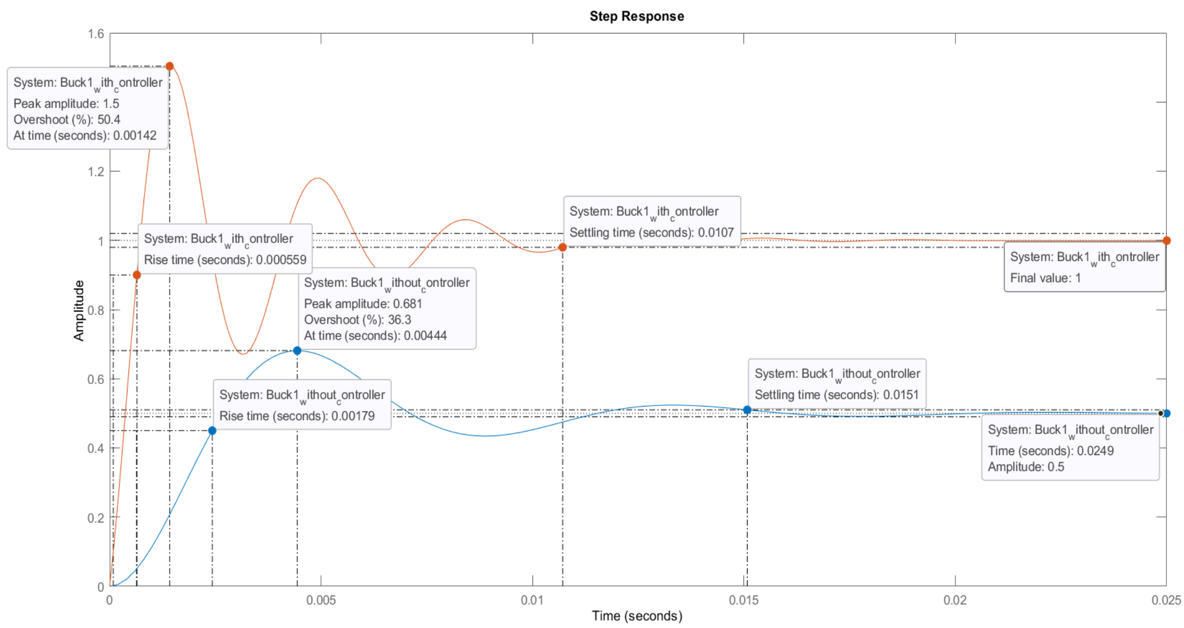

Figure 53: Step response of the PID controlled Buck Converter 1

Table 18: Time Response Specifications of Buck converter 1

Time response specifications	No PID controller	Tuned PID controller
Peak Amplitude	0.681	1.5
Rise time (sec)	0.00179	0.000559
Settling time (sec)	0.0151	0.0107
Steady state value	0.5	1

It can be seen from Table 18 that the rise and settling time for tuned PID controller is less than the converter having no controller. Tuning the PID parameters improved the steady state value from 0.5 to 1.

5.2.2 Fine tuning of the remaining converters

Using the same procedure outlined in section 5.6.1 above, K_p, K_i and K_d were obtained for Buck converters 2, 3 and Buck-Boost converter used in the DC Microgrid models. Table 19 outlines the time responses of all the power converters, with and without the tuned PID controllers.

Table 19: Time Response Specifications of Converters used in the DC Microgrid models

DC-DC Converters	Time Response Specifications			
	Peak Amplitude	Rise Time(sec)	Settling Time(sec)	Steady State Value
Buck converter 2 $K_p = 69.6$, $K_i = 3.48 \times 10^3$ and $K_d = 0.348$ **No PID Controller**	None (Overdamped)	0.824	1.47	0.5
Tuned PID Controller	1.17	0.0167	0.0817	1
Buck converter 3 $K_p = 48$, $K_i = 1$ and $K_d = 1$ **No PID Controller**	0.581	0.0013	0.00638	0.5
Tuned PID Controller	1	2.76×10^{-6}	4.98×10^{-6}	1
Buck – Boost Converter $K_p = 9.14$, $K_i = 3.81 \times 10^3$ and $K_d = 0.00548$ **No PID Controller**	0.582	0.0041	0.0202	0.5
Tuned PID Controller	1.43	0.00137	0.0203	1

Table 19 shows that the peak overshoot improved when the tuned PID controller was incorporated into the Buck converter 2. The overall performance in terms of the decreased rise time and settling time, and the increased steady state value was noted for the tuned PID controller.

For Buck converter 3, table 19 shows that the peak overshoot improved with the tuned PID controller and the overall performance improvement was noted.

As expected, the data in Table 19 proves that the peak amplitude of the buck-boost converter with the tuned PID controller is better than the one without any PID controller. Overall the converter with the tuned PID controller out-performed the one without the controller.

5.3 Summary: Tuning of the PID controllers

The purpose of tuning the PID parameters was to ensure that the output voltages from the power electronic converters, were more stable and accurate. Whilst, tuning the PID controllers provides satisfactory control, sometimes tuning may not provide optimal control [65].

However, overall, the tuned PID parameters enabled the DC MG model to perform faster than un-tuned ones. This was due to the faster rise time, settling time and increased steady state values. Peak overshoot was also better controlled using the tuned PID controllers.

Therefore, based on these key performance factors, tuned PID controllers were used for every power convertor in the DC Microgrid model to further investigate the EMI issues.

Chapter 6 Aggregated Conducted Electromagnetic Interference

This chapter will provide an insight into the research findings presented in the previous chapter, to evaluate the occurrence and reduction of the electromagnetic interference caused by the power converters in the DC Microgrid models. The aim is to also provide further theoretical analyses to confirm the findings of the simulated results which indicated that the aggregated conducted electromagnetic interference generated by multiple power converters, increase as the switching frequencies of the power converters are varied.

6.1 Tuned PID controlled Power Converters of various switching frequencies

In order to investigate how different switching frequency power converters affect the conducted EMI generation in the DC Microgrid model, the following sections would model various design topologies and report on their simulation outcomes.

6.1.1 Topology 4: Three converters of same switching frequency and one converter with different switching frequency

After running several iterations of simulations of the DC Microgrids having power converters of various switching frequencies, as well as considering the switching frequencies used in the commercial power converter products, the frequency range shown in Tables 20 – 22 were selected.

Table 20: Topology 4 - Power Converter Specifications

Power Converters	Buck Converter 1	Buck Converter 2	Buck Converter 3	Buck-Boost Converter
Switching frequencies	10kHz	103kHz	103kHz	103kHz

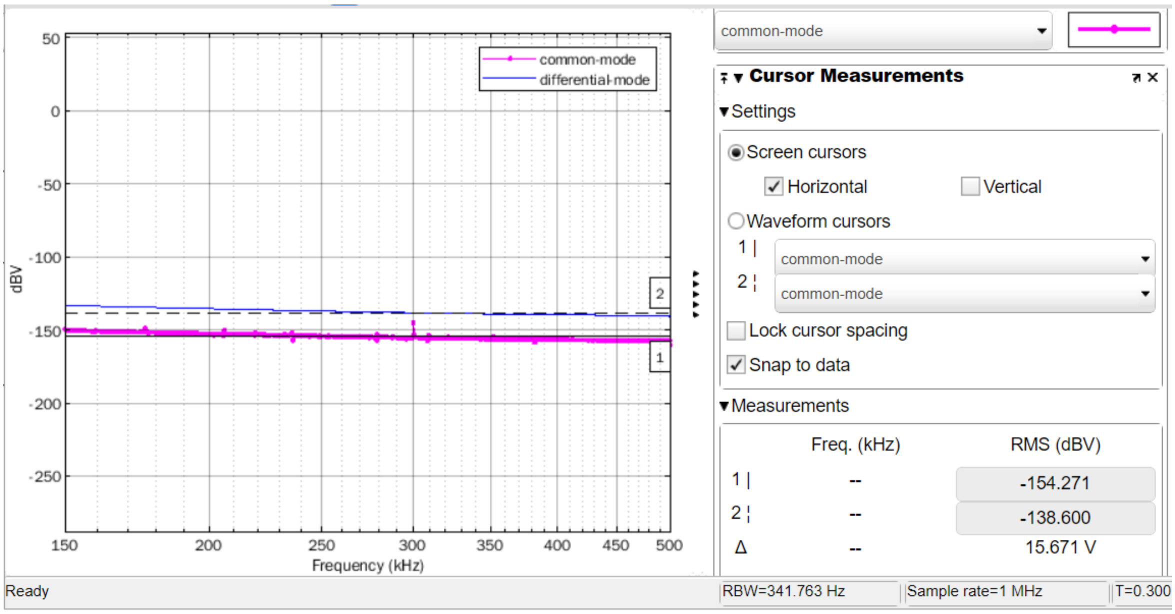

Figure 54: Conducted EMI simulation of Topology 4

6.1.2 Two Converters of same switching frequency and two converter of different switching frequency

Table 21: Topology 5 - Power Converter Specifications

Power Converters	Buck Converter 1	Buck Converter 2	Buck Converter 3	Buck-Boost Converter
Switching frequencies	10kHz	103kHz	103kHz	100kHz

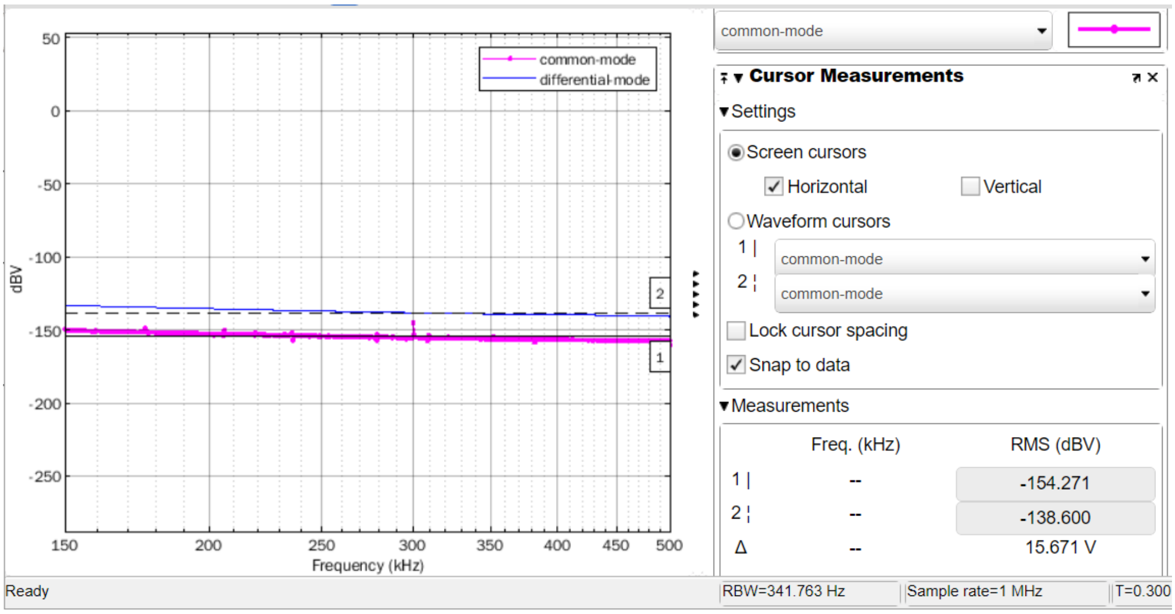

Figure 55: Conducted EMI simulation of Topology 5

6.1.3 Topology 6: All Converters of different switching frequencies

Table 22: Topology 6 - Power Converter Specifications

Power Converters	Buck Converter 1	Buck Converter 2	Buck Converter 3	Buck-Boost Converter
Switching frequencies	10kHz	103kHz	105kHz	100kHz

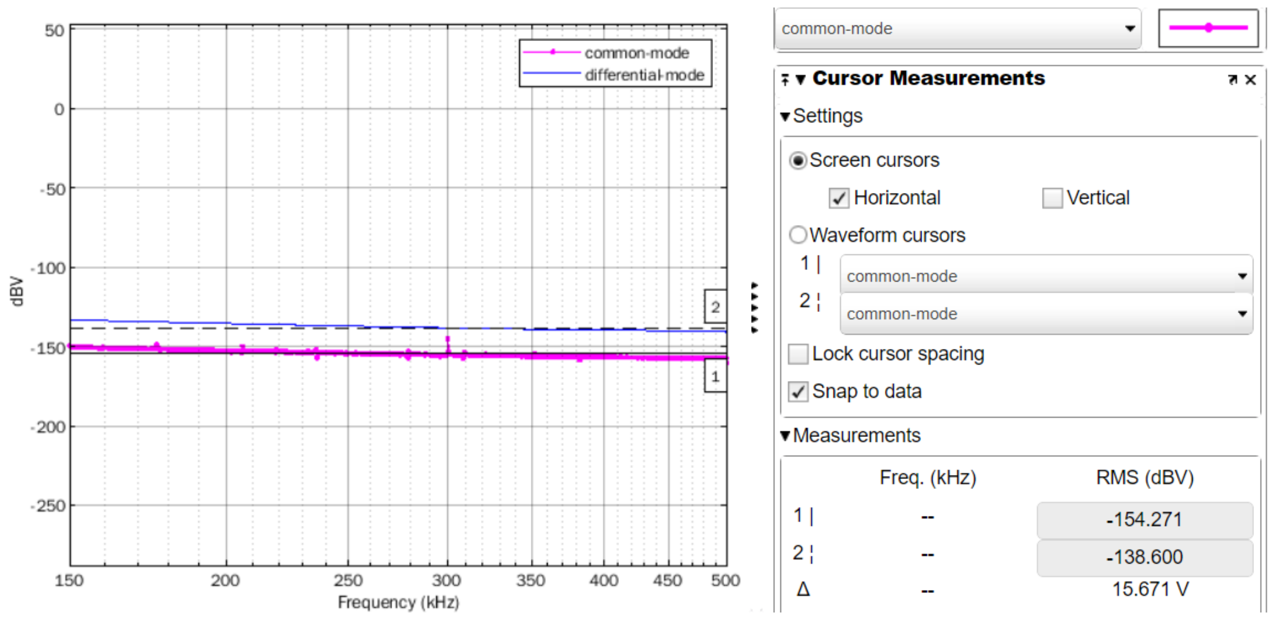

Figure 56: Conducted EMI simulation of Topology 6

6.1.4 Performance Analysis

The topologies 4–6 were designed to test how changing the switching frequencies of the power converters in the DC MG model affected the common-mode and differential-mode conducted EMI. In topology 4, three power converters had same switching frequency and only one had a different switching frequency. The simulation output displayed an overshoot around 200kHz and two minor ones at 300kHz and 400kHz. In topology 5, the switching frequency of two power converters were changed and the other two switching frequencies remained the same. Its simulation result showed the common-mode signals displaying very small signal spikes. Finally, in topology 6, the switching frequencies of all power converters were changed to be different from one another. This model's simulation illustrated much noiser common mode signals between 175kHz–310kHz. These model-based changes of the switching frequencies of multiple power converters, were designed and simulated to study how the common-mode and differential-mode conducted EMI behaved as the switching frequencies were varied.

It was observed from the above simulation outcomes that, as the switching frequencies of all the power converters were varied, the common-mode EMI signal became noiser. Increasing the difference between the switching frequencies of the converters,further,would have produced more visible signal spikes. However, as the switching frequencies of all the converters were optimised, further switching frequency variations were not possible for this model. As for the differential-mode EMI, signals did not exhibit any notable/significant changes as the switching frequencies of the power converters were varied.

In summary, the above results suggest that the aggregated or cumulative interference produced by multiple power converters of same switching frequencies may have helped in smoothing the common mode EMI, due to the phenomenon known as frequency beat [70], which would be discussed in detail in section 6.2. This phenomenon implies that having multiple power converters of different switching frequencies in a system, may contribute to an increased generation of the common mode interference. Changing the power converter's switching frequencies, have not exhibited any significant reduction in the differential mode EMI in the above topologies.

6.2 Aggregated conducted interference generated by the multi-converters in the DC Microgrid model

This chapter addresses the problem of aggregated interference generated by the four different power converters in the DC Microgrid model, which have been mitigated using common-mode and differential-mode conducted EMI filters. The function of the EMI filters in the DC Microgrid system is to spread out the EMI spectra at the given frequency range, in order to reduce the signal spikes/noises and smoothen the signals.

The cumulative effect of the conducted electromagnetic emissions caused by a group of power converters in a system is known as aggregated conducted interference. The individual switching frequencies of the DC-DC converters are treated as the sinusoidal components of a Fourier series [66]. Equation 6.1 describes the summation of the aggregation of the sinusoidal components of multiple power converters of different switching frequencies, mathematically, which can be used to measure the conducted EMI aggregation in multi converter systems such as the DC MG model [66]:

$$S_n(t;\{f_1,..,f_n\}) = \sum_{i=1}^{bn} sin(2\pi f_i t) = \frac{2}{n-1} \sum_{2\le i\le n, 1\le j\le i} cos\left(2\pi \frac{f_i - f_j}{2} t\right) sin\left(2\pi \frac{f_i + f_j}{2} t\right) \qquad (6.1)$$

where the frequency beat effect is prevalent when

$$max|f_i - f_j| \le min|f_i + f_j|. \qquad (6.2)$$

Appendix E contains the MATLAB codes of the above mathematical equation, used to generate the sum of the harmonic vibrations of four sinusoidal components of the switching frequencies f_1, f_2, f_3 and f_4. These switching frequencies had been used to design the power converters in the DC Microgrid models used for simulation in Chapter 5:

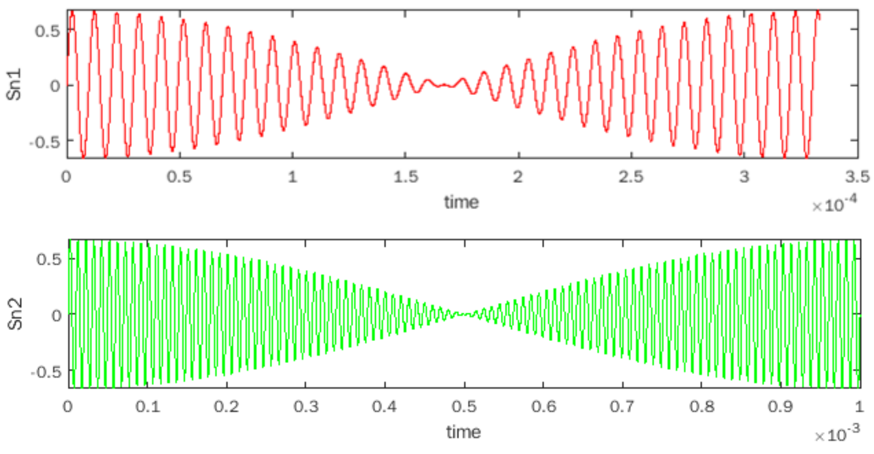

Figure 57: Summation of aggregated EMI signals generated by multiple power converters of different switching frequencies

The period of the summation of the aggregated sinusoidal EMI signals was calculated using the reciprocal of the largest common divisor [63] of all the pairs given by:

$$f_i - f_j \; for \;\; 2 \le i \le n, \;\; 1 \le j < i \qquad (6.3)$$

Figure 56 further proves the point that the increased EMI generation are due to the power converters operating at different switching frequencies, which were noted in the simulation outcomes in the earlier sections. Figure 56 illustrates that, as the switching frequencies of the power converters were varied, i.e., the greater the difference between their switching frequencies were, the higher the occurrence of the switching frequency harmonics were observed in the aggregation of the sinusoidal components of the EMI signals generated by multiple DC-DC converters.

In the first subplot (in red), all three power converters had same switching frequencies so the difference between their switching frequencies was approximately zero. In the second subplot (in green), the switching frequency difference between all three converters, increased from 0kHz to 3kHz. It can be observed that the superimposed signals produced by individual converters increased significantly as the switching frequency difference this time, was further increased. These plots confirm that as the differences between the switching frequencies of power converters are increased, this leads to greater the occurrence of the aggregated conducted EMI signals, due to an increased generation of the superimposed aggregated sinusoidal components of the EMI signals. To further confirm this, the signal envelopes were generated using the equation 6.4 below. The purpose of studying these envelopes [66] was to observe how the signals extreme values varied, as the switching frequencies changed.

$$Env_n(t; \{f_1, \ldots, f_n\}) = \frac{2}{n-1} \sum_{2 \le i \le n, 1 \le j \le i} cos\left(2\pi \frac{f_i - f_j}{2} t\right) \qquad (6.4)$$

Appendix F contains the MATLAB codes used to generate the envelopes of the aggregated signals, using the equation 6.4 above, resulting from the aggregation of four sinusoidal components of frequencies f_1, f_2, f_3 and f_4.

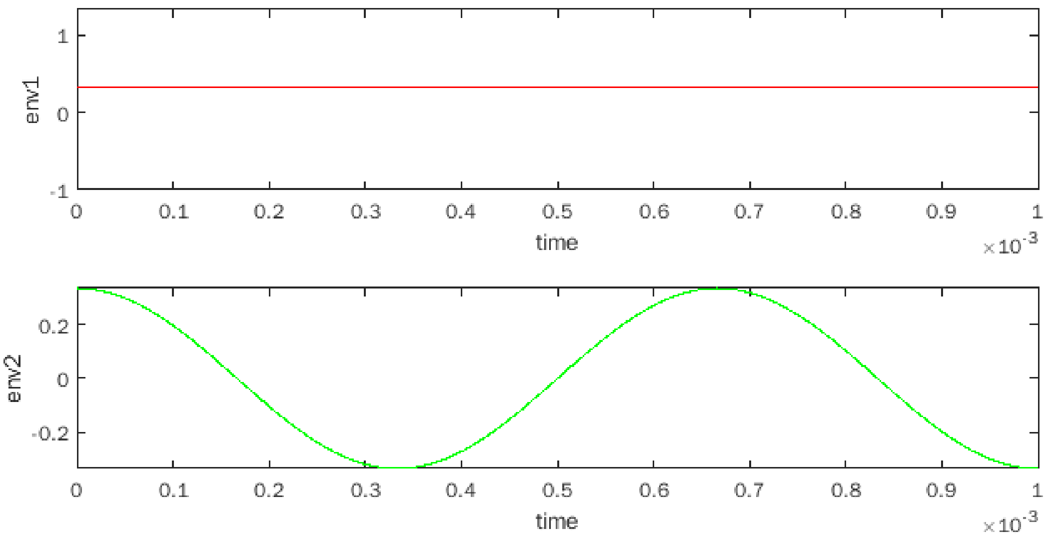

Figure 58: Envelope of signals resulting from aggregation of four sinusoidal components

It has been noted from the literature study [66], that the smaller, the switching frequency differences in the power converters were, the slower the aggregated signal envelope changes were. The frequency beat effect arises when the aggregating sinusoidal components of similar frequencies cause the modulation of their amplitudes with small frequency envelopes. In Figure 57, the switching frequency difference in first subplot(in red), was zero for 2nd, 3rd and 4th converters, hence its aggregated signal "envelope" showed no change at all, displaying a straight line with constant EMI envelope values for the period of the waveform.

On the contrary, for the 2nd subplot (in green) as the switching frequency difference between 2nd, 3rd and 4th converters changed, the envelope of the aggregated EMI becomes more prevalent and obvious. Due to increased difference between the switching frequencies of these multi-converter systems, higher number of harmonic vibrations presented the envelope of aggregation of the sinusoidal components of the signals as is evident in the second subplot in Figure 57.

Figure 57 illustrates the first subplot (in red) of the DC MG system with DC-DC converters of the similar switching frequencies. The second subplot (in green) shows how the aggregated EMI signals start to form envelope of the aggregated sinusoidal components as the switching frequency difference increases by 3kHz, between converters 3(f_3) and converter 4(f_4). The second subplot (in green) displays a well-formed envelope of high frequency signals generated by the aggregation of the sinusoidal components as the switching frequency difference increased, between converters 3(f_3) and converter 4(f_4). Therefore, Figure 57 demonstrates how the aggregated sinusoidal signals occur due to the different switching frequencies of the individual converters. The main point to note here is the lower the difference between the switching frequencies of the individual converters is, the slower the changing envelopes of the aggregated EMI signals [66], which were observed in Figure 57, subplots 1 and 2. To summarise this fact, the rate of change of the envelope is dependent on the differences of the converters' harmonic frequency [66]. This indicates that the aggregated sinusoidal components increase, as the switching frequency differences between individual converters increase, thereby confirming the findings from the simulation results that, as the switching frequency differences between the converters increase, so does the aggregated conducted EMI generation.

On the other hand, when the aggregated EMI envelopes of the converters of same switching frequencies are generated, as can be seen in the first sub-plot of Figure 57, no superimpositions of aggregated EMI signals were observed.

For the DC Microgrid topology having all identical multi-converters, the EMI envelope ceases to exist. A constant envelope value further demonstrates and confirms the research findings from the simulations presented in the previous chapter, that as we increase the difference between the switching frequencies of the multi converters in the DC MG models, the aggregated conducted EMI becomes more prevalent.

For the DC MG models where all power converters had same or similar switching frequencies, the aggregated conducted EMI generation was lower relative to the models with different switching frequencies. Thus, the Figures 56 and 57 have mathematically proven and confirmed the findings from the simulations presented and discussed in the previous chapter.

Therefore, using the analysis above, it can be further ascertained that systems having multiple power converters with different switching frequencies, are the primary cause of the aggregated EMI generation. This EMI issue could be mitigated by using power converters of same or similar switching frequencies as well as incorporating custom designed EMI suppressing filters. Such power converters are available commercially and, if they are not, then custom-designed ones are the best solutions to solve this EMI pollution which can lead to power quality issues in the DC MGs.

6.3 Limitation of the study

The research outcomes using the MATLAB/Simulink simulations have been verified by mathematically by the analysis presented above. However, no experimental designs and measurements have been undertaken to verify the research outcomes. This, however, does not affect the integrity of the research produced due to the research findings being consistent with the literature findings.

Chapter 7 Conclusions and Recommendations for Future Works

7.1 General Conclusions

The novelty of this thesis lies in the research and development work conducted on a standalone, low voltage, photovoltaic based DC Microgrid, to study and mitigate the aggregated conducted electromagnetic interference generated due to the interactions between its multiple fast switching power converters. The power converters operated at switching frequencies ranging in hundreds of kilohertz, which generates electromagnetic interference. The DC Microgrid model was designed and simulated in the MATLAB/Simulink environment to study the conducted electromagnetic interference. The focus of this work was on investigating the electromagnetic interference and delivering an efficient EMI filter topology which could suppress the common-mode and differential mode noise effectively.

This thesis provided an introduction of the theoretical background of the DC Microgrid models. It also outlined the design methodology used, to conduct this research.

The literature review of the EMI emissions due to the power converters and the permissible levels of the EMI, mandated by regulatory bodies such as the IEC was also discussed in detail. The literature study showed that according to CISPR 11, the permissible levels of the EMI for class A quasi-peak level ranges from 79dBµV – 130dBµV and for the average level, 66dBµV – 120dBµV at the frequency range of 0.15MHz – 0.5MHz. It also discussed various DC Microgrid components and presented techniques to mitigate the EMI emissions. Studying these techniques and the information available on the DC Microgrids, led to the conclusions that the EMI generation is a challenging subject and sufficient research has not been performed on this research topic, to date. These research gaps provided the motivation to perform a thorough investigation into this topic to gain useful insights into the EMI emissions due to multiple power converter operations.

Discussions pertaining to the conducted and radiated electromagnetic interference, were covered in all its significant aspects.

The designs of various DC microgrid models, which were utilised to conduct this investigation, were presented. Detailed descriptions on the development of the architecture of various topologies of the DC Microgrids were presented. Design issues encountered at various phases of the design process were also highlighted. EMI filter topology to suppress the conducted EMI was also discussed in detail.

The simulation outputs of all the DC microgrid topologies and the EMI analysis based on the simulation results were analysed extensively. The frequency range of interest for these simulations was 0.15MHz – 0.5MHz, as the conducted EMI emissions were more prevalent in this range. It was found out that all DC microgrid models with EMI filters, complied with the permissible levels of the conducted EMI as mandated by CISPR11. All the DC microgrid models incorporated with EMI filters generated the common-mode interference of -30dBμV to 0 dBμV and the differential-mode interference of -18 dBμV to -5dBμV, both of which are significantly lesser than the mandated levels (refer to Figure The PI versus PID controllers' concepts were thoroughly investigated. PID controllers were found to be more efficient in reducing the EMI generation which led to designing more optimised and tuned PID controllers for each power converter used in the DC Microgrid design, with the overall purpose of minimising the EMI emissions as much as practically achievable.

Finally, the theoretical analysis of the aggregated conducted EMI generated by using various DC Microgrid topologies were discussed using mathematical modelling which demonstrated how the theoretical results supported the simulation results.

To summarise the research outcome, this thesis contributed to a comprehensive understanding of the EMI emissions in a low voltage DC Microgrid, due to its fast-switching multiple power converters, by designing and analysing several DC Microgrid topologies. Mitigation techniques to supress the EMI generation was also presented and discussed. These led to designing a robust and effective DC Microgrid architecture. This design would help minimise the EMI generation which, if left uncontrolled, would have significantly affected the power quality of the microgrid and could have potentially interfered with other neighbouring electronic systems.

7.2 Thesis Contributions

As a whole, this thesis contributed to a comprehensive understanding of the electromagnetic interference emissions in the off-grid DC Microgrid models, due to their power converters, by analysing several DC MG topologies presented in Chapters 4 and 5. Mitigation techniques to suppress the conducted electromagnetic interference were also presented.

Therefore, this thesis recommends an optimum architecture of the DC Microgrid models giving good power quality due to lower EMI emissions, which would add significant value to future microgrid applications in geographically remote locations utilising the low voltage distribution with DC household loads at multiple DC bus voltages. This recommended architecture has the following characteristics:

- Have one set of common-mode and differential-mode EMI filters in the DC Microgrid model

- Design tuned PID controlled power converters for the microgrid
- Design all power converters to have same or similar switching frequencies.

7.3 Recommendations for Future Work

For future works, Droop control method could be researched for this DC Microgrid model. Due to time constraints, it was not possible to investigate this. A droop control of this standalone DC MG model would ensure that efficient load sharing between the power converters is achieved and prevent circulating currents due to any potential output voltage differences between the converters. Zammit, D. et al. 2019 discussed three Droop Control methods which could be used to implement the load sharing between all the PI controlled paralleled Buck converters, in a DC MG model. Implementing the droop control technology into the recommended DC Microgrid model, above, could produce a much lower EMI generating DC MG model.

Another aspect of future research could be to design the physical models of the DC Microgrid and measure how the proximity of the power converters affects the aggregated EMI generation. Measuring the radiated EMI of the physically designed prototypes of the DC Microgrids mentioned in the previous chapters, would complement the findings of this research on the aggregated conducted EMI. This holistic approach would help produce comprehensive research on how the aggregated EMI of both radiated and conducted modes are affected by multi converter systems. For this, prototypes of key topologies presented in this research could be manufactured and the physical distance between the converters could be varied to study how their spacing or proximity in the DC Microgrid system would affect the EMI emission.

Finally, it is recommended to physically design and build the key DC Microgrid topologies presented in this thesis and verify the research outcomes presented through the mathematical and simulation studies which were discussed in this thesis in earlier sections.

References

[1] J. Sun and M. Chen, "Analysis and mitigation of interactions between PFC converters and the AC source", *The IEEE 4th International Power Electronics and Motion Control Conference, 2004. IPEMC 2004.*, vol. 1, pp. 99-104, 2004.

[2] H. Zhang, L. Yang, S. Wang, and J. Puukko, "Common-mode EMI noise modelling and reduction with balance technique for three-level neutral point clamped topology," IEEE Trans. Ind. Electron., vol. 64, no. 9, pp. 7563–7573, Sep. 2017.

[3] A. Hesener, "Electromagnetic Interference (EMI) in Power Supplies", *Emcfastpass.com*, 2010. [Online]. Available: https://www.emcfastpass.com/wp-content/uploads/2017/04/Electromagnetic-Interference-EMI-in-Power-Supplies.pdf.

[4] X. Qian, Y. Yang, C. Li, and S.-C. Tan, "Operating Cost Reduction of DC Microgrids Under Real-Time Pricing Using Adaptive Differential Evolution Algorithm," *IEEE Access*, vol. 8, pp. 169247–169258, 2020.

[5] C. Hua, K. Gunawardane and T. Lie, "Investigation of Progressing Low and Medium Voltage DC Standards to Acquire the Implementation Scenarios for Domestic/Commercial and Industrial Converters and Enabling Technologies", *2021 6th IEEE Asia Conference on Power and Electrical Engineering (ACPEE)*, 2021.

[6] F. Pareschi, R. Rovatti and G. Setti, "EMI Reduction via Spread Spectrum in DC/DC Converters: State of the Art, Optimization, and Tradeoffs," in IEEE Access, vol. 3, pp. 2857-2874, 2015, doi: 10.1109/ACCESS.2015.2512383

[7]"Electromagnetic Interference and Renewable Energy Microgrids," resources.pcb.cadence.com. https://resources.pcb.cadence.com/blog/2022-electromagnetic-interference-and-renewable-energy-microgrids (accessed Aug. 24, 2022).

[8] L. Zhai, G. Hu, M. Lv, T. Zhang and R. Hou, "Comparison of Two Design Methods of EMI Filter for High Voltage Power Supply in D

[9] "Future Architecture of the Network (FAN)," *Future Architecture of the Network (FAN)*. https://www.fan.ac.nz/

[10] L. Yang, S. Wang, H. Zhao and Y. Zhi, "Prediction and Analysis of EMI Spectrum Based on the Operating Principle of EMC Spectrum Analyzers", *IEEE Transactions on Power Electronics*, vol. 35, no. 1, pp. 263-275, 2020.

[11] Y. Zhao, Y. Liu, S. Li, W. Yan, J. Yan, X. Chen and X. Qiu, "The radiated EMI noise modeling and features analysis on the basis of Smart Grid Equipment", *2014 IEEE International Symposium on Electromagnetic Compatibility*, 2014.

[12] N. Mohan, *First course on power electronics*. Hoboken, N.J.: Wiley, 2011, pp. 38-74.

[13] M. Sudheer, "Estimating Far-Field EMI from CM current of Buck Converter", *2019 IEEE 5th Global Electromagnetic Compatibility Conference (GEMCCON)*, 2019.

[14] M. Beck, "EMI filter components and their nonidealities for automotive DC/DC regulators", *Texas Instrument*, 2021. [Online]. Available: https://www.ti.com/lit/an/slyt782/slyt782.pdf?ts=1642822672349&ref_url=https%253A%252F%252Fwww.bing.com%252F.

[15] H. Loschi, R. Smolenski, P. Lezynski, D. Nascimento and G. Demidova, "Aggregated Conducted Electromagnetic Interference Generated by DC/DC Converters with Deterministic and Random Modulation", *Res.mdpi.com*, 2020. [Online]. Available: https://res.mdpi.com/d_attachment/energies/energies-13-03698/article_deploy/energies-13-03698.pdf

[16] R. Amjadifard, M. Tavakoli Bina, H. Khaloozadeh and F. Bagheroskouei, "Proposing an Improved DC LISN for Measuring Conducted EMI Noise", *IEEE Transactions on Electromagnetic Compatibility*, vol. 63, no. 3, pp. 752-761, 2021.

[17] S. Wang and F. C. Lee, "Investigation of the Transformation Between Differential-Mode and Common-Mode Noises in an EMI Filter Due to Unbalance," in IEEE Transactions on Electromagnetic Compatibility, vol. 52, no. 3, pp. 578-587, Aug. 2010, doi: 10.1109/TEMC.2009.2038899

[18] Hesener, A., 2010. *Electromagnetic Interference (EMI) in Power Supplies*. [online] Emcfastpass.com. Available at: https://www.emcfastpass.com/wp-content/uploads/2017/04/Electromagnetic-Interference-EMI-in-Power-Supplies.pdf

[19] J. Yao, Y. Li, Z. Ma, and S. Wang, "Advances of Modelling and Reduction of Conducted and Radiated EMI in Flyback Converters," *2020 IEEE Energy Conversion Congress and Exposition (ECCE)*, 2020.

[20] "CISPR 14-1:2020 | IEC Webstore | electromagnetic compatibility, EMC, smart city," webstore.iec.ch. https://webstore.iec.ch/publication/60734 (accessed Aug. 24, 2022).

[21] saiglobal.com, "EN 55014-1 : 2017 | Electromagnetic Compatibility - Requirements For Household Appliances, Electric Tools And Similar Apparatus - Part 1: Emission (CISPR 14-1:2016 + COR1 | SAI Global," Saiglobal.com, 2017. https://infostore.saiglobal.com/en-us/Standards/EN-55014-1-2017-353609_Saig_Cenelec_Cenelec_806531/

[22] saiglobal.com, "EN 55014-1 : 2017 | Electromagnetic Compatibility - Requirements For Household Appliances, Electric Tools And Similar Apparatus - Part 1: Emission (CISPR 14-1:2016 + COR1 | SAI Global," Saiglobal.com, 2017. https://infostore.saiglobal.com/en-us/Standards/EN-55014-1-2017-353609_Saig_Cenelec_Cenelec_806531/

[23] T. Hegarty, "An overview of conducted EMI specifications for power supplies," *Texas Instrument*, pp. 2–4, Feb. 2018.

[24] P. Nuutinen, A. Pinomaa, J.-P. Ström, T. Kaipia, and P. Silventoinen, "On Common-Mode and RF EMI in a Low-Voltage DC Distribution Network," *IEEE Transactions on Smart Grid*, vol. 5, no. 5, pp. 2583–2592, Sep. 2014, doi: 10.1109/tsg.2014.2305997.

[25] A. Martin, "AN-2162 Simple Success With Conducted EMI From DCDC Converters", *E2e.ti.com*, 2022. [Online]. Available: https://e2e.ti.com/cfs-file/__key/communityserver-discussions-components-files/196/1256.snva489b_5F00_conducted-EMI.pdf.

[26] G. Ciarpi and S. Saponara, "Inductorless DC/DC Converter for Aerospace Applications With Insulation Features," *IEEE Transactions on Circuits and Systems II: Express Briefs*, vol. 67, no. 9, pp. 1659–1663, Sep. 2020, doi: 10.1109/tcsii.2020.3010297.

[27] Z. Zhang and K.-T. Chau, “Pulse-Width-Modulation-Based Electromagnetic Interference Mitigation of Bidirectional Grid-Connected Converters for Electric Vehicles,” *IEEE Transactions on Smart Grid*, vol. 8, no. 6, pp. 2803–2812, Nov. 2017, doi: 10.1109/tsg.2016.2541163.

[28] M. Laour, R. Tahmi, and C. Vollaire, “Modeling and Analysis of Conducted and Radiated Emissions Due to Common Mode Current of a Buck Converter,” *IEEE Transactions on Electromagnetic Compatibility*, vol. 59, no. 4, pp. 1260–1267, Aug. 2017, doi: 10.1109/temc.2017.2651984.

[29] S. Karimi, E. Farjah, T. Ghanbari, F. Naseri, and J.-L. Schanen, “Estimation of Parasitic Capacitance of Common Mode Noise in Vehicular Applications: An Unscented Kalman Filter-Based Approach,” *IEEE Transactions on Industrial Electronics*, vol. 68, no. 8, pp. 7526–7534, Aug. 2021, doi: 10.1109/tie.2020.3007088.

[30] R. Shirai, K. Wada, and T. Shimizu, “Failure Protection Method for CAN Communication Against EMI Noise Generated by Switched-Mode Power Supplies,” *IEEE Journal of Emerging and Selected Topics in Power Electronics*, vol. 9, no. 5, pp. 6152–6160, Oct. 2021, doi: 10.1109/jestpe.2021.3053025.

[31] D. Muller, M. Beltle, and S. Tenbohlen, “EMI Suppression of a DC–DC Converter Using Predictive Pulsed Compensation,” *IEEE Transactions on Electromagnetic Compatibility*, vol. 63, no. 6, pp. 2134–2142, Dec. 2021, doi: 10.1109/temc.2021.3084896.

[32] “DC Microgrids,” *Microgrid Projects*. http://microgridprojects.com/dc-microgrids/

[33] “System Modelling and Simulation - MATLAB & Simulink Solutions,” *au.mathworks.com*. https://au.mathworks.com/solutions/system-design-simulation.html

[34] H. Darajit, C. Shuyu and R. Naayagi, "Design of EMI Filter for Switched Mode Power supply", 2020 3rd International IEEE Conference on Energy, Power and Environment: Towards Clean Energy Technologies, 2021.

[35] V. K. Bussa, A. Aman, and R. K. Singh, “A Minimum-Phase Dual Output Hybrid Converter for Standalone Hybrid AC/DC Supply Systems,” *IEEE Transactions on Industry Applications*, vol. 57, no. 1, pp. 1044–1056, Jan. 2021, doi: 10.1109/tia.2020.3035730.

[36] J. Kumar, A. Agarwal, and N. Singh, “PV fed Hybrid Energy Storage System Supported DC Microgrid,” *2019 IEEE 1st International Conference on Energy, Systems and Information Processing (ICESIP)*, 2019.

[37] V. Saxena, N. Kumar, B. Singh, and B. K. Panigrahi, “A Rapid Circle Centre-Line Concept-Based MPPT Algorithm for Solar Photovoltaic Energy Conversion Systems,” *IEEE Transactions on Circuits and Systems I: Regular Papers*, vol. 68, no. 2, pp. 940–949, Feb. 2021, doi: 10.1109/tcsi.2020.3038114.

[38] S. Salman, X. Ai, and Z. Wu, *Design of a P-&-O algorithm based MPPT charge controller for a stand-alone 200W PV system*. Springer Open, 2018, pp. 1–8.

[39] H. Wen and W. Zhu, “Control and Protection of DC Microgrid with Battery Energy Storage System,” *2016 IEEE International Conference on Power Electronics, Drives and Energy Systems (PEDES)*, 2016.

[40] Y. Shan, J. Hu, K. W. Chan, Q. Fu, and J. M. Guerrero, “Model Predictive Control of Bidirectional DC–DC Converters and AC/DC Interlinking Converters—A New Control Method for PV-Wind-

Battery Microgrids," *IEEE Transactions on Sustainable Energy*, vol. 10, no. 4, pp. 1823–1833, Oct. 2019, doi: 10.1109/tste.2018.2873390.

[41] M. Wei, M. Ye, J. B. Li, Q. Wang, and X. Xu, "State of Charge Estimation of Lithium-Ion Batteries Using LSTM and NARX Neural Networks," *IEEE Access*, vol. 8, pp. 189236–189245, 2020, doi: 10.1109/access.2020.3031340.

[42] M. A. Hannan, Md. M. Hoque, A. Hussain, Y. Yusof, and P. J. Ker, "State-of-the-Art and Energy Management System of Lithium-Ion Batteries in Electric Vehicle Applications: Issues and Recommendations," *IEEE Access*, vol. 6, pp. 19362–19378, 2018, doi: 10.1109/access.2018.2817655.

[43] "Generic battery model - Simulink - MathWorks Australia," *au.mathworks.com*. https://au.mathworks.com/help/physmod/sps/powersys/ref/battery.html

[44] D. W. Gao, *Energy Storage for Sustainable Microgrid*. U.S.A.: Elsevier Ltd, 2015, pp. 35–77.

[45] "DC/DC Buck Converter | DC/DC Converter | Overview | Step-Down Buck | TI.com", *Ti.com*, 2022. [Online]. Available: https://www.ti.com/power-management/non-isolated-dc-dc-switching-regulators/step-down-buck/buck-converter-integrated-switch/overview.html

[46] X. Li, X. Zhang, and F. Lin, "Multi-Objective Design of Output LC Filter for Buck Converter via the Coevolving-AMOSA Algorithm," *IEEE Access*, vol. 9, pp. 11884–11894, 2021, doi: 10.1109/access.2020.3034361.

[47] J. Hua, "Output Noise Filtering for DC/DC Power Modules Application Report Output Noise Filtering for DC/DC Power Modules," 2019. Accessed: Jan. 22, 2022. [Online]. Available: https://www.ti.com/lit/an/snva871/snva871.pdf?ts=1599420606544.

[48] T. Halder, "Hard and Soft Switching Geometries For Operations of the MOSFET Used For the SMPS," *2021 IEEE Devices for Integrated Circuit (DevIC)*, Aug. 2021.

[49] "Buck converters (integrated switch) | Products | TI.com," *Ti.com*, 2020. https://www.ti.com/power-management/non-isolated-dc-dc-switching-regulators/step-down-buck/buck-converter-integrated-switch/products.html

[50] D. Suski and D. A. Górski, "Modeling and Simulation of the Averaged Dynamics of PWM Converters Operating in CCM and DCM," *2018 23rd IEEE International Conference on Methods & Models in Automation & Robotics (MMAR)*, pp. 849–854, Oct. 2018, doi: 10.1109/MMAR.2018.8485926.

[51] B. Hauke, "Basic Calculation of a Buck Converter's Power Stage," *Texas Instrument*, Dec. 2011. https://www.ti.com/lit/an/slva477b/slva477b.pdf?ts=1641436783503&ref_url=https%253A%252F%252Fwww.google.com%252

[52] J. Ning, J. Zeng and X. Du, "A Four-port Bidirectional DC-DC Converter for Renewable Energy-Battery-DC Microgrid System," *2019 IEEE Energy Conversion Congress and Exposition (ECCE)*, 2019, pp. 6722-6727, doi: 10.1109/ECCE.2019.8912185.

[53] F. Li, C. Cañizares and Z. Lin, "Energy Management System for DC Microgrids Considering Battery Degradation," *2020 IEEE Power & Energy Society General Meeting (PESGM)*, 2020, pp. 1-5, doi: 10.1109/PESGM41954.2020.9281580.

[54] S. Saha, A. Bhattacharjee, D. Elangovan and G. Arunkumar, "DC microgrid system for rural electrification," *2017 International Conference on Energy, Communication, Data Analytics and Soft Computing (ICECDS)*, 2017, pp. 307-313, doi: 10.1109/ICECDS.2017.8390006.

[55] I. Weiss, “Basic Calculation of an Inverting Buck-Boost Power Stage,” *Texas Instrument*, Feb. 2017.
https://www.ti.com/lit/an/slva721a/slva721a.pdf?ts=1641596097097&ref_url=https%253A%252F%252Fwww.bing.com%252F

[56] M. S. Omar, A. El-Deib, A. L. El Shafei, M. A. El.rhman and M. E. Abdallah, "Comparative study between PI and fuzzy-logic controllers for three-phase grid-connected photovoltaic systems," *2016 Eighteenth International Middle East Power Systems Conference (MEPCON)*, 2016, pp. 380-386, doi: 10.1109/MEPCON.2016.7836919.

[57]“Appliance running costs,” *Consumer NZ*. https://www.consumer.org.nz/articles/appliance-running-costs

[58] J. L. Kotny, T. Duquesne and N. Idir, "Design of EMI filters for DC-DC converter," *2010 IEEE Vehicle Power and Propulsion Conference*, 2010, pp. 1-6, doi: 10.1109/VPPC.2010.5729047.

[59] “Application Report AN-2162 Simple Success With Conducted EMI From DC- DC Converters,” 2011. Accessed: Jan. 22, 2022. [Online]. Available: https://www.ti.com/lit/an/snva489c/snva489c.pdf?ts=1641817628047&ref_url=https%253A%252F%252Fwww.google.com.hk%252F.

[60] F. K. Tuffner, J. W. Pierre and R. F. Kubichek, "Computationally efficient updating of a weighted Welch periodogram for nonstationary signals," *2008 51st IEEE Midwest Symposium on Circuits and Systems*, 2008, pp. 799-802, doi: 10.1109/MWSCAS.2008.4616920.

[61] “Spectral Analysis - MATLAB & Simulink - MathWorks Australia,” *au.mathworks.com*. https://au.mathworks.com/help/dsp/ug/spectral-analysis.html

[62] A. McEachern, "Special Issues Related to the Frequency Range 2kHz-150kHz," *2018 IEEE Symposium on Electromagnetic Compatibility, Signal Integrity and Power Integrity (EMC, SI & PI)*, 2018, pp. 1-23, doi: 10.1109/EMCSI.2018.8495308.

[63] K. Murakawa, N. Hirasawa, H. Ito and Y. Ogura, "Electromagnetic interference examples of telecommunications system in the frequency range from 2kHz to 150kHz," *2014 International Symposium on Electromagnetic Compatibility, Tokyo*, 2014, pp. 581-584.

[64] S. Kapat and P. T. Krein, "PID controller tuning in a DC-DC converter: A geometric approach for minimum transient recovery time," *2010 IEEE 12th Workshop on Control and Modeling for Power Electronics (COMPEL)*, 2010, pp. 1-6, doi: 10.1109/COMPEL.2010.5562367.

[65] K. Ogata and Pearson, *Modern control engineering*. Delhi: Pearson, 2016.

[66] R. Smolenski, P. Lezynski, J. Bojarski, W. Drozdz, and L. C. Long, “Electromagnetic compatibility assessment in multi-converter power systems – Conducted interference issues,” *Measurement*, vol. 165, p. 108119, Dec. 2020, doi: 10.1016/j.measurement.2020.108119.

[67] F. Krug and P. Russer, "Quasi-peak detector model for a time-domain measurement system," in *IEEE Transactions on Electromagnetic Compatibility*, vol. 47, no. 2, pp. 320-326, May 2005, doi: 10.1109/TEMC.2005.847410.

[68] “EMI emissions testing: peak, quasi-peak, and average measurements,” *EDN Asia*, Jul. 13, 2018. https://www.ednasia.com/EMI-emissions-testing-peak-quasi-peak-and-average-measurements/

[69] “Convert from dBuV | Cantwell Engineering,” *www.cantwellengineering.com*. http://www.cantwellengineering.com/calculator/convert/dbuv (accessed Jan. 23, 2022).

[70] M. Enohnyaket, "Generation of very low frequency beat waves from power converters," *2009 IEEE Vehicle Power and Propulsion Conference*, 2009, pp. 1025-1031, doi: 10.1109/VPPC.2009.5289734.

Appendices

Appendix A: MATLAB codes for Stability of the PI vs PID controllers

MATLAB codes to determine the stability of the PI versus the PID controllers used in the power converter models

```
clc;                                %clear the screen
num=[0.0222222]                     %numerator coefficients
den=[6.24*10^(-7) 0.0166667 0.0222222]  %denominator coefficients
G2= tf(num,den)                     %transfer function
H=[1]                               %feedback initialization

B2= feedback(G2,H)                  %feedback integration

kp=12;                              %Proportional control
ki=1;                               %Integral control
kd=1;                               %Derivative control
Gc2=pid(kp,ki,kd);                  %PID controller
Bc2=feedback(Gc2*G2,H)              %Buck2 with PID

step(B2)                            %step response of Buck2
hold on                             %Hold the first obtained response
step (Bc2)                          %step response of Buck2 with PID
```

Appendix B: MATLAB codes for Bode plot responses

The bode plot response was generated to determine the stability of both the controllers using the MATLAB codes below:

```
clc;                                          %clear the screen
num=[0.0222222]                               %numerator coefficients
den=[6.24*10^(-7) 0.0166667 0.0222222]  %denominator coefficients
G2= tf(num,den)                               %transfer function
H=[1]                                  %feedback initialization

B2= feedback(G2,H)                            %feedback integration

kp=12;                                        %Proportional control
ki=1;                                         %Integral control
kd=1;                                         %Derivative control
Gc2=pid(kp,ki,kd);                            %PID controller
Bc2=feedback(Gc2*G2,H)                        %Buck2 with PID

[Gm,Pm,Wcg,Wcp] = margin(B2)   %Calculate Gain Margin, phase margin of B2
bode(B2)                                      % Obtain bode plot of B2
hold on                                %Hold the first obtained response
[Gm,Pm,Wcg,Wcp] = margin(Bc2) %Calculate Gain Margin, phase margin of Bc2
bode(Bc2)                                     % Obtain bode plot of Bc2
```

Appendix C: MATLAB codes for Ziegler Nichols First Method

The Ziegler Nichols First Method was implemented using the MATLAB codes below:

```
clc;                                        %clear the screen
num=[7.6]                                   %numerator coefficients
den=[2.75*10^(-5) 0.01256 7.6]              %denominator coefficients
G1= tf(num,den)                             %transfer function
H=[1]                                       %feedback initialization
Buck1_without_controller=feedback(G1,H)     %feedback integration
step(Buck1_without_controller)  %step response of Buck1 without controller
```

Appendix D: MATLAB codes for calculating the K parameters

MATLAB code below, was used to design the K_p, K_i and K_d.

```
clc;                                    %clear the screen
num=[7.6]                               %numerator coefficients
den=[2.75*10^(-5) 0.01256 7.6]          %denominator coefficients
G1= tf(num,den)                         %transfer function
H=[1]                                   %feedback initialization
Buck1_without_controller=feedback(G1,H)     %feedback integration
step(Buck1_without_controller)  %step response of Buck1 without controller

hold on                     %Hold the first obtained response

K=0.67;                 %steady state value of obtained graph
L=0.0006;               %lag
T=0.005-L;              %time constant

a=K*L/T;
Ti=2*L;                 %calculate the value of Ti
Td=L/2;                 %calculate the value of Td

Kp=1.2/a                %calculate the value of Kp
Ki=Kp/Ti                %calculate the value of Ki
Kd=Kp*Td                %calculate the value of Kd
cont=pid(Kp,Ki,Kd)      %PID controller

Buck1_with_controller=feedback(cont*G1,H)       %Buck1 with PID
step (Buck1_with_controller)        %step response of Buck1 with PID
```

Appendix E: MATLAB Codes for the Mathematical equation 6.1

MATLAB codes to generate the sum of the harmonic vibrations of four sinusoidal components of frequencies f_1, f_2, f_3 and f_4:

```
N=4;
t=linspace(0,1/0.93*10*1^(-5),1000);%93kHz

 for fi1=[103000 103000 100000]        %f2,f3,f4
   for fj1=[10000 103000 103000]       %f1,f2,f3
      Sn1=                                   (2/(N-1))*((cos(2*pi*((fi1-
fj1)/2)*t)).*(sin(2*pi*((fi1+fj1)/2)*t)));
   end
 end
plot(t,Sn1,'linewidth',1,'color','r')
xlabel('time')
ylabel('Sn1')
```

Appendix F: MATLAB Codes for the Mathematical equation 6.4

MATLAB codes to generate the Envelope of the signals resulting from the aggregation of four sinusoidal components of frequencies f_1, f_2, f_3 and f_4:

```
%        f1      f2      f3      f4
%Case1   10K     103K    103K    100K
%Case2   10K     103K    103K    103K
%Case3   10K     103K    105K    100K

% 2 ≤ i ≤ 4   and  1 ≤ j ≤ i
N=4;
t=linspace(0,1/0.93*10*1^(-5),1000);%93kHz
 %t=linspace(0,1/0.093*10*1^(-7),1000);%930kHz

 for fi1=[103000 103000 100000]        %f2,f3,f4
   for fj1=[10000 103000 103000]       %f1,f2,f3
      env1=(1/(N-1))*(cos(2*pi*((fi1-fj1)/2)*t));
   end
 end

subplot(3, 1, 1)
plot(t,env1,'linewidth',1,'color','r')
xlabel('time')
ylabel('env1')

 for fi2=[103000 103000 103000]        %f2,f3,f4
   for fj2=[10000 103000 103000]       %f1,f2,f3
      env2=(1/(N-1))*(cos(2*pi*((fi2-fj2)/2)*t));
   end
 end

subplot(3, 1, 2)
plot(t,env2,'linewidth',1,'color','g')
xlabel('time')
ylabel('env2')

for fi3=[103000 105000 100000]         %f2,f3,f4
   for fj3=[10000 103000 103000]       %f1,f2,f3
      env3=(1/(N-1))*(cos(2*pi*((fi3-fj3)/2)*t));
   end
end
subplot(3, 1, 3)
plot(t,env3,'linewidth',1,'color','b')
xlabel('time')
ylabel('env3')
```